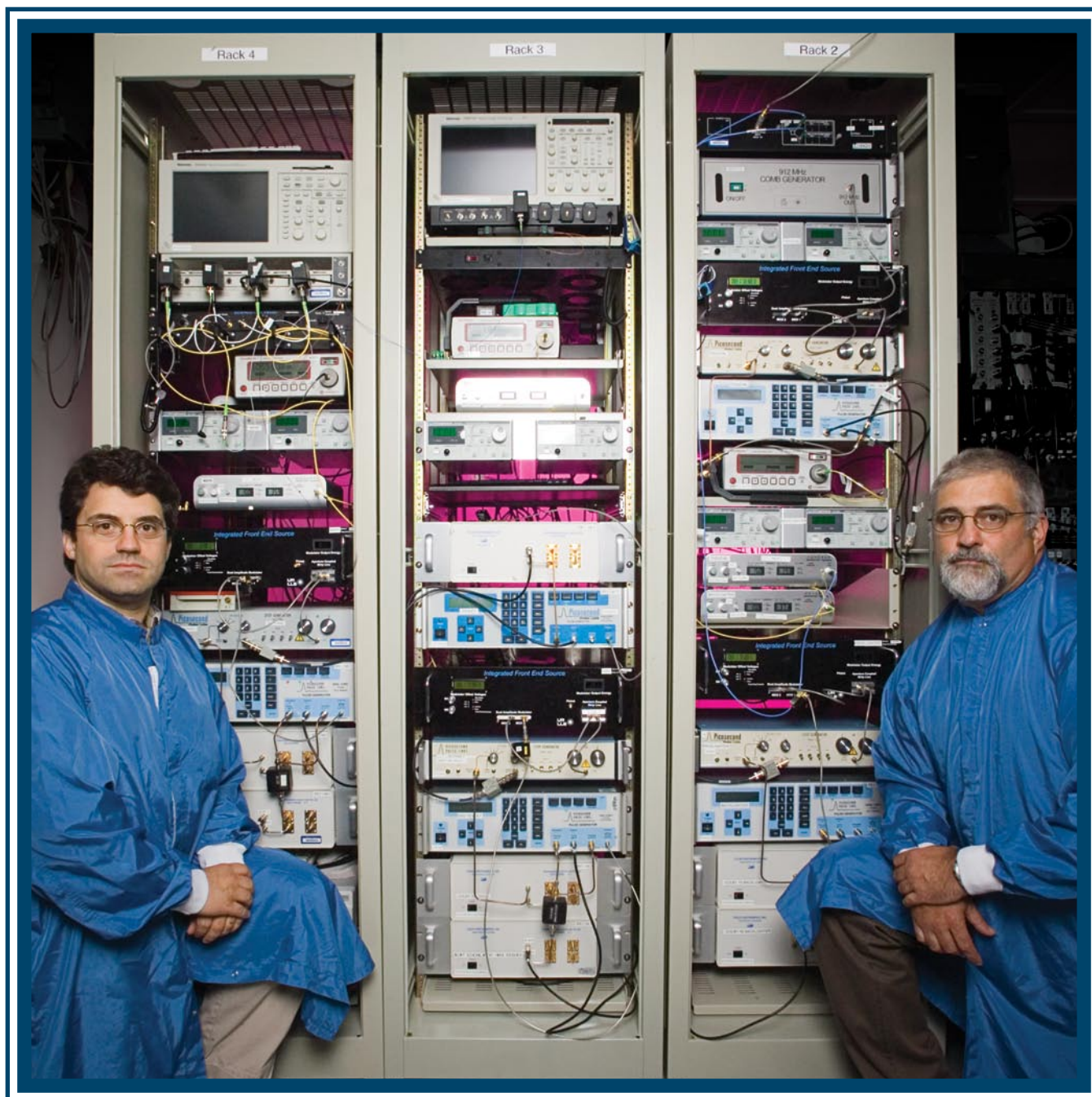


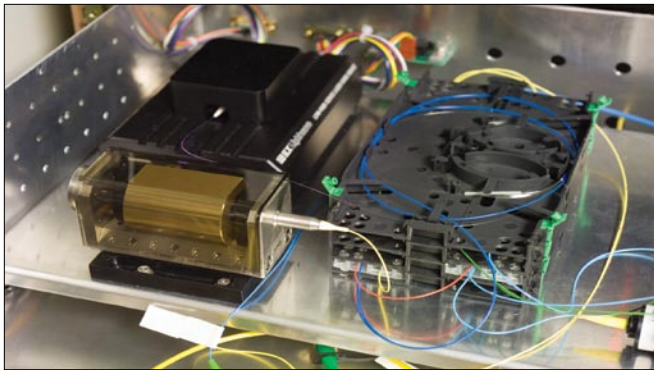
LLE Review



Quarterly Report



About the Cover:



The front cover shows LLE scientist John Marciante and LLE engineer Rick Roides with the integrated front-end sources (IFES) for each of the four driverlines on the OMEGA Laser System. IFES is a rack-mounted, front-end seed source that was developed at LLE for the OMEGA and OMEGA EP Laser Systems. This laser source generates an optical pulse in the 100-pJ range using a compact, stable, single-frequency fiber DFB laser, dual lithium niobate amplitude modulators, and a high-gain polarization-maintaining fiber amplifier. A single rack-mounted box contains the amplitude modulators, the LLE-built fiber amplifier, and custom LLE control electronics, as shown in the photo at the top left, and is driven by software written at LLE (ACSL v2). The key to the success of this system is the high-gain fiber amplifier, as shown in the bottom left photo. This amplifier was developed at LLE and is detailed in the article beginning on p. 63. Without any adjustable alignment, the IFES system has demonstrated high stability, turn-key operation, and low maintenance. IFES has contributed significantly to the stability of the OMEGA front end, and thus has helped provide higher reliability in the generation and reproducibility of shaped pulses on OMEGA.

This report was prepared as an account of work conducted by the Laboratory for Laser Energetics and sponsored by New York State Energy Research and Development Authority, the University of Rochester, the U.S. Department of Energy, and other agencies. Neither the above named sponsors, nor any of their employees, makes any warranty, expressed or implied, or assumes any legal liability or responsibility for the accuracy, completeness, or usefulness of any information, apparatus, product, or process disclosed, or represents that its use would not infringe privately owned rights. Reference herein to any specific commercial product, process, or service by trade name, mark, manufacturer, or otherwise, does not necessarily constitute or imply its endorsement, recommendation, or favoring

by the United States Government or any agency thereof or any other sponsor. Results reported in the LLE Review should not be taken as necessarily final results as they represent active research. The views and opinions of authors expressed herein do not necessarily state or reflect those of any of the above sponsoring entities.

The work described in this volume includes current research at the Laboratory for Laser Energetics, which is supported by New York State Energy Research and Development Authority, the University of Rochester, the U.S. Department of Energy Office of Inertial Confinement Fusion under Cooperative Agreement No. DE-FC52-92SF19460, and other agencies.

Printed in the United States of America
Available from
National Technical Information Services
U.S. Department of Commerce
5285 Port Royal Road
Springfield, VA 22161
Price codes: Printed Copy A04
Microfiche A01

For questions or comments, contact Semyon Papernov, Editor, Laboratory for Laser Energetics, 250 East River Road, Rochester, NY 14623-1299, (585) 275-4259.

Worldwide-Web Home Page: <http://www.lle.rochester.edu/>

LLE Review

Quarterly Report



Contents

In Brief	iii
High-Gain, Polarization-Preserving, Yb-Doped Fiber Amplifier for Low-Duty-Cycle Pulse Amplification	63
The Development of Methods and Techniques for the Decontamination of Metals and Alloys	70
Basic Principles of Direct-Drive Ignition Target Design	83
Tests of the Hydrodynamic Equivalence of Direct-Drive Implosions with Different D ₂ and ³ He Mixtures	90
Deterministically Polarized Fluorescence from Uniaxially Aligned Single-Dye Molecules	102
Fiber-Coupled Single-Photon Detectors Based on NbN Superconducting Nanostructures for Practical Quantum Cryptography and Photon-Correlation Studies	108
Transition Metal Dithiolene Near-IR Dyes and Their Applications in Liquid Crystal Devices	112
Publications and Conference Presentations	

In Brief

This volume of the LLE Review, covering January–March 2006, features “High-Gain, Polarization-Preserving, Yb-Doped Fiber Amplifier for Low-Duty-Cycle Pulse Amplification” by J. R. Marciante and J. D. Zuegel. In this article (p. 63) the authors report on a high-gain, low-noise, double-pass ytterbium-doped amplifier for which amplified spontaneous emission (ASE) suppression techniques were utilized to fabricate a double-pass amplifier with the noise properties of a single-pass amplifier. A double-pass configuration allows for significantly higher gains to be obtained in a fiber amplifier than can be achieved in a single-pass configuration. Simulations based on a rate-equation model were used to analyze the ASE and the impact of the suppression techniques. These techniques were implemented in an alignment-free, double-pass fiber amplifier with 26-dB gain at a wavelength 23 nm off the gain peak and a –48-dB noise floor, while amplifying linearly polarized optical pulses with a low duty cycle.

Additional highlights of recent research presented in this issue include the following:

- W. T. Shmayda, M. Quinlan, Z. Chambers, and U. Schroeder discuss the development of methods and techniques for the decontamination of metals and alloys from tritium (p. 70). The efficacy of tritium removal from stainless steel using four different approaches has been studied: thermal desorption in a dry inert gas purge, thermal desorption in a wet inert gas purge, thermal desorption in an inert gas purge containing hydrogen peroxide, and radio-frequency–driven argon plasma irradiation. This study indicates that reducing the activity in metals below $0.5 \mu\text{Ci/g}$ is feasible without generating secondary active waste byproducts other than water.
- V. N. Goncharov presents a review of the basic concept of laser-driven ICF ignition with emphasis on the direct-drive ignition target design, requirements for the temporal shape of the laser pulse, and consideration of the stability issues (p. 83).
- J. R. Rygg, J. A. Frenje, C. K. Li, F. H. Séguin, and R. D. Petrasso (Plasma Science and Fusion Center, MIT), and J. A. Delettrez, V. Yu. Glebov, V. N. Goncharov, and D. D. Meyerhofer (LLE) report the results on direct-drive implosions of targets filled with different mixtures of D_2 and ^3He gas on the OMEGA Laser System (p. 90). At temperatures above a few electron volts, D_2 and ^3He gases are fully ionized, and hydrodynamically equivalent fuels with different ratios of D_2 and ^3He can be chosen to have the same mass density, total particle density, and equation of state. Implosions with a 50/50 mixture of $\text{D}:\text{}^3\text{He}$ by atom consistently result in measured nuclear yields, half of that anticipated by scaling from measured yields of implosions with pure D_2 and nearly pure ^3He . This observation is seen over a wide range of experimental configurations, including targets with a variety of shell thicknesses and fill pressures, simultaneously for two different nuclear yields (D-D and D- ^3He), as well as for shock and compression yields. A number of possible mechanisms to cause the scaling are considered, but no dominant mechanism has been identified.
- S. G. Lukishova, A. W. Schmid, R. Knox, P. Freivald, L. Bissell, R. Boyd, C. R. Stroud, Jr., and K. L. Marshall demonstrate, for the first time, deterministically polarized fluorescence from single emitters (dye molecules) (p. 102). In this experiment a planar-aligned, nematic liquid crystal host provides uniaxial alignment of single-dye molecules in a preferred direction. As a result, fluorescence of these single emitters is deterministically polarized (single photon source), which allows one to consider such systems for applications in photonic quantum information.

- W. Słysz, M. Węgrzecki, J. Bar, P. Grabiec, and M. Górńska (Institute of Electron Technology, Warsaw); V. Zwiller, C. Latta, and P. Bohi (Swiss Federal Institute of Technology, Zurich); I. Milostnaya, O. Minaeva, A. Antipov, O. Okunev, A. Korneev, K. Smirnov, B. Voronov, N. Kaurova, and G. Gol'tsman (Moscow State Pedagogical University, Moscow); and A. Pearlman, A. Cross, I. Komissarov, A. Verevkin, and R. Sobolewski (ECE and LLE) present results on fiber-coupled single-photon detectors based on NbN superconducting nanostructures for practical quantum cryptography and photon-correlation studies (p. 108). Several two-channel, single-photon detector systems based on two fiber-coupled superconducting single-photon detectors were built and characterized. The best device reached the system quantum efficiency of 0.3% in the 1550-nm telecommunication wavelength with a fiber-to-detector coupling factor of about 30%.
- K. L. Marshall, G. Painter, K. Lotito, A. G. Noto, and P. Chang present results on design and synthesis of transition metal dithiolene near-IR dyes (p. 112). Transition metal complexes based on nickel, palladium, or platinum dithiolene cores show substantial promise for guest–host liquid crystal devices operating in the near- to mid-IR region. The authors show some specific application examples for these materials in LC electro-optical devices and discuss the most recent results in the computational modeling of physical and optical properties of this interesting class of organometallic optical materials.

Semyon Papernov
Editor

High-Gain, Polarization-Preserving, Yb-Doped Fiber Amplifier for Low-Duty-Cycle Pulse Amplification

Introduction

Erbium-doped fiber amplifiers have become commonplace in telecommunications systems.¹ High-bit-rate pulse trains mean that continuous pumping can be utilized. Additionally, the unknown polarization state of the arriving pulses is ideal for common fiber-optic components and erbium-doped fibers, which typically do not preserve the polarization state of the light passing through them. For other applications, however, such conditions do not apply. Low-duty-cycle pulses leave gain available in the fiber for long durations between pulses, which can lead to parasitic lasing or destructive self-pulsations. The amplification of signals with wavelengths far from the gain peak only enhances this problem since the gain can be substantially lower for such signals. Additionally, the amplification of linear polarizations requires not only a polarization-maintaining (PM) active fiber, but also PM wavelength division multiplexers (WDM's) and other fiber components that can be difficult to fabricate.

Utilizing a double-pass configuration allows for significantly higher gains to be obtained in a single-fiber amplifier than can be achieved in a single pass.²⁻⁵ Additionally, using a Faraday rotator just before the end mirror ensures that the pulse returning from the second pass through the cavity has a polarization state that is orthogonal to that of the input pulse. Consequently, when used in conjunction with a polarizing beam splitter, the output pulse can be separated from the input pulse with high fidelity.³ Double-pass configurations are ripe for parasitic lasing or destructive self-pulsations in a highly pumped unsaturated amplifier, however, since half a resonator is created intentionally. Special care must be taken to minimize reflections from components, connectors, and splices. Utilizing a timed gate, e.g., an acousto-optic modulator (AOM), at the end of the first pass can ensure stable operation,³ but this significantly adds to the complexity of the system.

In this work, a double-pass, ytterbium-doped fiber amplifier is presented that overcomes these hurdles to provide high gain for low-duty-cycle pulse repetition rates while preserving the linear polarization state in a single-spatial-mode package that

requires no alignment. In **Amplified Spontaneous Emission Considerations** (p. 63) the amplified spontaneous emission (ASE) is modeled in ytterbium-doped fiber amplifiers. In particular, the effects of ASE filtering are studied for use in a double-pass amplifier configuration. The **Experimental Results** (p. 66) are presented on the measurements of a double-pass fiber amplifier built with the various ASE-suppression schemes described in **Amplified Spontaneous Emission Considerations**. Additional discussions regarding the experimental configuration and modeling are given in **Discussion and Conclusions** (p. 68), along with concluding remarks.

Amplified Spontaneous Emission Considerations

The amplified spontaneous emission of fiber amplifiers can be studied via rate-equation modeling.⁶ Such a model represents the optical power resolved in wavelength along the length of the fiber and the ytterbium atomic states as a homogeneously broadened inversion. The resultant equations are given by

$$\pm \frac{\partial P^\pm}{\partial z} + \frac{1}{v_g} \frac{\partial P^\pm}{\partial t} = \Gamma[\sigma_e N_2 - \sigma_a N_1]P^\pm - \alpha P^\pm + 2\sigma_e N_2 \frac{hc}{\lambda^3} \Delta\lambda + S\alpha_{RS}P^\mp \quad (1)$$

and

$$\frac{\partial N_2}{\partial t} = \frac{1}{hc} \int \frac{\Gamma}{A} [\sigma_e N_2 - \sigma_a N_1] (P^+ + P^-) d\lambda - \frac{N_2}{\tau}, \quad (2)$$

where $P^\pm(z, t, \lambda)$ is the forward (+) or backward (-) propagating power as a function of wavelength, time, and axial position along the fiber. N_2 and N_1 are the upper and lower state population densities, respectively, as a function of time and axial position along the fiber and are related by the total ion concentration as $N_t = N_2 + N_1$, which is constant throughout the fiber. Wavelength-dependent parameters in Eqs. (1) and (2) include the geometrical overlap of the fiber mode with the core Γ , modal area A , absorption/emission cross section of the active ion $\sigma_{a/e}$, group velocity v_g , fiber attenuation α , and Rayleigh scattering coefficient α_{RS} . Additional parameters include the upper-state lifetime τ , the fiber-core capture coefficient S , and the optical sampling bandwidth $\Delta\lambda$.

Equation (1) represents the bidirectional power flow through the fiber, including stimulated emission, spontaneous emission, and absorption from the active ions; loss due to the inherent fiber attenuation; and Rayleigh scattering. Since the parameters all have wavelength dependence, only a single equation is mathematically required to represent the behavior of the pump, signal, and ASE.

Equation (2) represents the excited-state population density, which is governed by the absorption and emission of optical power as well as nonradiative decay. One notable omission in Eq. (2) is the wavelength dependence of the excited state governed by the details of the atomic transition manifold. This leads to, for example, excitation due to the absorption of long-wavelength light that can then be used to amplify shorter wavelength light. While this effect is small in the presence of a highly inverted fiber, the impact on the current work is to overestimate the ASE at the gain peak. Since the current goal is to suppress this feature, the model will yield a worse case than is expected experimentally.

For simplicity, the wavelength dependence of A , v_g , α , and α_{RS} are neglected. Since the current work considers core-pumped (as opposed to cladding-pumped) active fibers, Γ can also be well approximated by a constant. The ytterbium cross sections are obtained from the data in Ref. 7. For convenience, these cross sections are fit to a series of Gaussians of the form

$$\sigma_j = \sum_m A_{j,m} \exp\left\{-\left[\frac{\lambda - \lambda_{j,m}}{w_{j,m}}\right]^2\right\}$$

with the coefficients listed in Table 106.I. Other utilized parameters are listed in Table 106.II.

Table 106.I: Gaussian coefficients for ytterbium emission and absorption cross sections.

j	$A_{j,m}$ (10^{-27} m ²)	$\lambda_{j,m}$ (nm)	$w_{j,m}$ (nm)
a	180	950	70
a	360	895	24
a	510	918	22
a	160	971	12
a,e	2325	975	4
e	160	978	12
e	340	1025	20
e	175	1050	60
e	150	1030	90

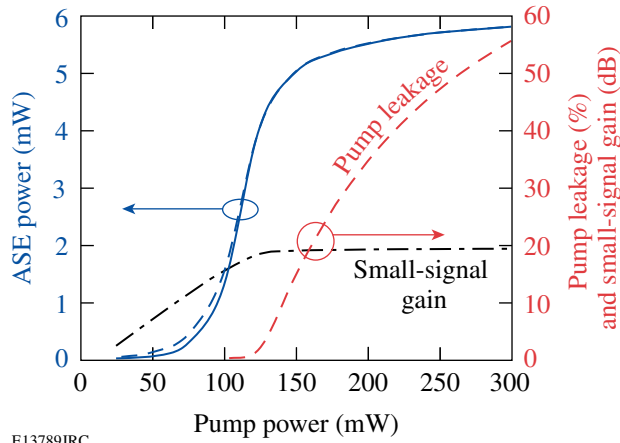
Table 106.II: Parameters used in simulations.

Parameter	Value
N_t	9.4×10^{24} m ⁻³
Γ	0.85
A	$30 \mu\text{m}^2$
v_g	$c/1.5$
α	0.003 m ⁻¹
$S\alpha_{RS}$	1.2×10^{-7} m ⁻¹
τ	0.84 ms
$\Delta\lambda$	1 nm
λ_{pump}	976 nm
λ_{signal}	1053 nm

Data provided with the ytterbium-doped fiber (Nufern), along with our own measurements on the fiber, determined the values of N_t , Γ , and A . The other values were obtained from Ref. 6. The parameters used are compiled in Table 106.II. A simple finite-difference method is utilized to calculate the power and inversion distributions in the fiber. Initial conditions assume no optical power or inversion within the fiber, and the pump power is included as a boundary condition. A double-pass configuration can also be realized by applying the appropriate boundary conditions.

Unsaturated fiber amplifiers cannot be pumped to arbitrarily high levels because of self-pulsations and oscillation, which limit the length of fiber that can be practically used in a single-pass amplifier. In an unsaturated amplifier this translates to limited available gain. Figure 106.1 shows the forward and reverse amplified spontaneous emission for the case of reverse pumping and very weak signal amplification (no gain depletion) for a 3.5-m length of Yb: fiber with the characteristics in Table 106.II. The small-signal gain, defined as the ratio of output energy to input energy, for a 1053-nm signal and the pump leakage are also shown in this figure. After 140 mW of pump power, the fiber is almost completely inverted, and the remaining pump is lost out of the opposite end of the fiber. The small-signal gain 23 nm off the gain peak is therefore limited to approximately 20 dB.

Since the gain is in fact unsaturated, simply sending the signal back through for a second pass increases the amplification without additional pumping. Such a double-pass configuration, however, also allows the ASE to make a second trip through the gain, which can lead to undesirable oscillation

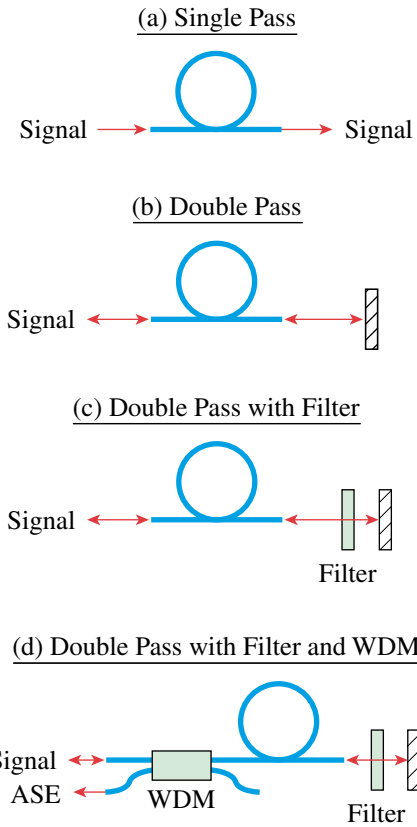


E13789JRC

Figure 106.1 Total (spectrally integrated) forward (solid) and reverse (dashed) ASE, 976-nm pump leakage, and 1053-nm small-signal gain as a function of pump power for a 3.5-m-length Yb: fiber.

and self-pulsations. The ASE must therefore be filtered to use a double-pass configuration. Two simple methods of filtration were investigated, as depicted in Fig. 106.2. The first is a bandpass filter, which is inserted between subsequent trips through the active fiber to deny double-pass ASE except in a small bandwidth around the filter peak. The second is a WDM designed to split the ASE peak from the signal, which removes a significant fraction of the ASE power from the signal, provided the signal is not near the gain peak. Four different amplifier configurations are modeled, as shown in Fig. 106.2. The first two are simple single- and double-pass configurations through the fiber. In the third configuration, a bandpass filter is added between subsequent passes through the fiber. The fourth configuration adds a WDM filter to the output of the third configuration.

For these calculations, the filters are assumed to be lossless at the transmission peaks with zero transmission at the nulls. The mirror adds 1 dB of loss to the double-pass amplifiers. Assuming pump and signal wavelengths of 976 and 1053 nm, respectively, the total (spectrally integrated) ASE power out of the different amplifier configurations is shown in Fig. 106.3 as a function of pump power. Because of undepleted gain and pump leakage, the single-pass ASE has a maximum power below 6 mW. In the double-pass configuration, the amplifier becomes saturated by the ASE, which extracts a significant fraction of the gain in the fiber. This linear trend in the ASE growth with pump power leads to an ASE level that is greater than 25 times the single-pass case and means that there will be very limited reduced gain available for the signal. In contrast, the dotted trace shows that the insertion of the bandpass filter

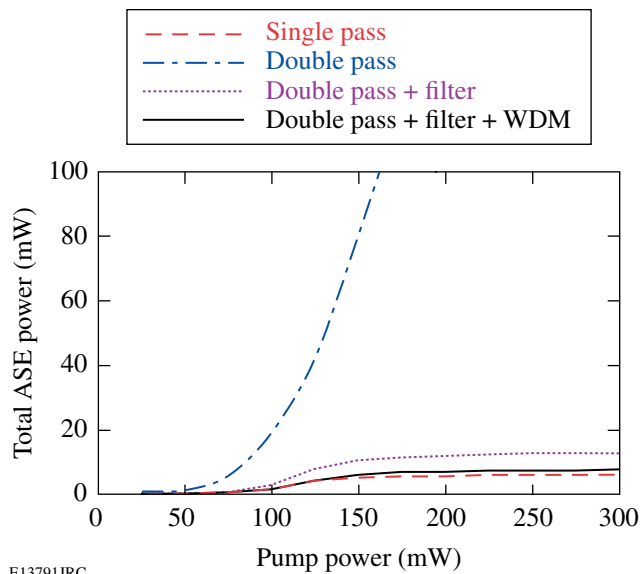


E13813JRC

Figure 106.2 Depiction of modeled configurations for (a) single pass, (b) double pass, (c) double pass with an intracavity bandpass filter, and (d) the same as (c) with a WDM filter at the amplifier output.

prohibits the ASE closest to the gain peak from experiencing double-pass gain. The total ASE is therefore limited to small-signal amplification, even with double-pass amplification far off the gain peak, and accumulates no more than twice the power of the single-pass configuration. The insertion of this filter then allows for exponential signal gain from the double-pass amplifier. The addition of the WDM filter (solid curve) reduces the total ASE output power of the double-pass fiber amplifier to only 30% more than the single-pass ASE.

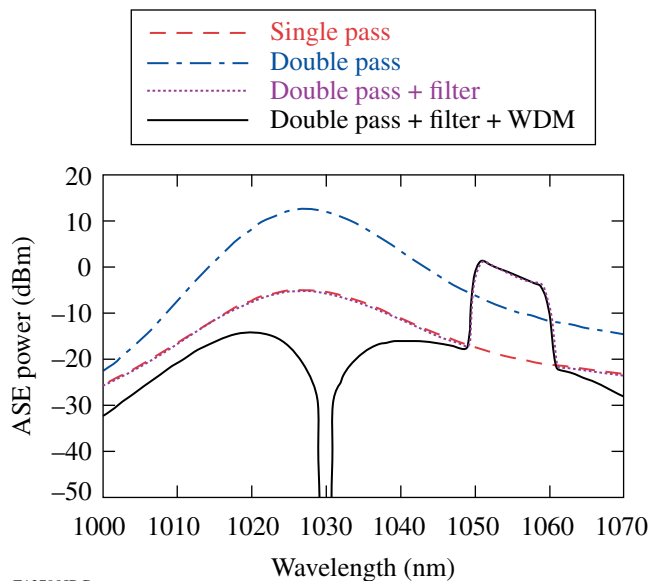
The ASE spectra for the four configurations are shown in Fig. 106.4 at a pump power of 250 mW. The ASE within the bandpass filter is actually stronger than the unfiltered double-pass ASE since the gain is unsaturated. Nonetheless, this lack of gain saturation allows for double-pass gain of the signal in the amplifier. The bandpass filter is therefore critical for operation of this double-pass configuration for the amplification of signals off the gain peak.



E13791JRC

Figure 106.3

Total (spectrally integrated) ASE power at the amplifier output as a function of pump power for the configurations shown in Fig. 106.2 using the fiber from Fig. 106.1.



E13790JRC

Figure 106.4

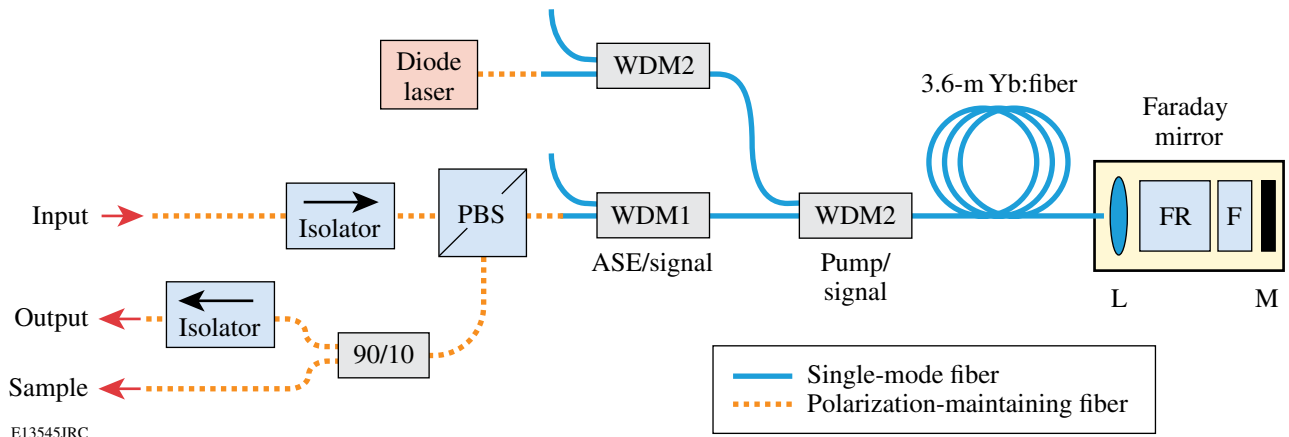
Amplified spontaneous emission spectra at the amplifier output for the configurations shown in Fig. 106.2 using the fiber from Fig. 106.1 with 250 mW of pump power.

Experimental Results

Under the guidance of **Amplified Spontaneous Emission Considerations** (p. 63), a double-pass polarized amplifier was constructed that contained both the bandpass filter and the

WDM and utilized a Faraday mirror with a polarizing beam splitter (PBS) to separate input from output and preserve the linear polarization state. This amplifier configuration is shown in Fig. 106.5 and utilizes both single-mode (SM) and PM fibers. The input signal comes through a PM-pigtailed isolator to prevent any ASE or signal from returning to the seed source. The light then passes through a PM-pigtailed polarizing beam splitter followed by a single-mode, 1030-nm/1053-nm wavelength division multiplexer (WDM) used to reduce ASE. A SM WDM combines the seed light with pump light from a fiber Bragg grating-stabilized pump laser with a second WDM in series for additional isolation of the pump diode from the amplified signal. The combined light is sent into 3.6 m of single-mode, single-clad, ytterbium-doped fiber with an unsaturated absorption coefficient of approximately 70 dB/m at 975 nm. After the first pass of amplification, the signal passes through a Faraday mirror, a factory-aligned, fiber-coupled package containing a Faraday rotator, 10-nm bandpass filter at 1053 nm, and mirror. The reflected light passes back through the Faraday mirror package, the Yb-doped fiber, and the WDM's, one of which acts to filter out the ASE centered at 1030 nm (WDM1). Since the polarization at the PBS is orthogonal to that which entered the PBS because of the Faraday mirror, the light is ejected out a different port and sent through a PM 90/10 splitter to provide polarized signal and sample ports. All fibers were spliced using a Furukawa S183PM fusion splicer, and there are no alignment knobs in the system. The pump was operated continuously and there is no AOM gate so that no temporal alignment is required between the seed pulses and the amplifier.

The seed pulse used in this amplifier was a 2-ns square pulse with 1.56 pJ of energy, resulting in a peak power of 0.78 mW. The seed pulse had an optical wavelength of 1053 nm and a pulse repetition rate of 300 Hz and was linearly polarized with a polarization extinction ratio of 20 dB. Different lengths of Yb-doped fiber were tested in the amplifier to optimize the active fiber length in terms of maximizing gain while maintaining stability as well as operation free from parasitic lasing or self-pulsations. For a given fiber length, a fraction of the fiber remains unpumped and thus lossy to the signal wavelength. If the pumped portion of the fiber has sufficient gain, then the amplifier can *Q*-switch because of the saturable absorption of the unpumped section of fiber and minute reflections in the system. This can be remedied by making the fiber sufficiently short; however, there is an optimum fiber length for which the fiber provides maximum gain without self-pulsations. For several amplifiers that were constructed, the optimum fiber length



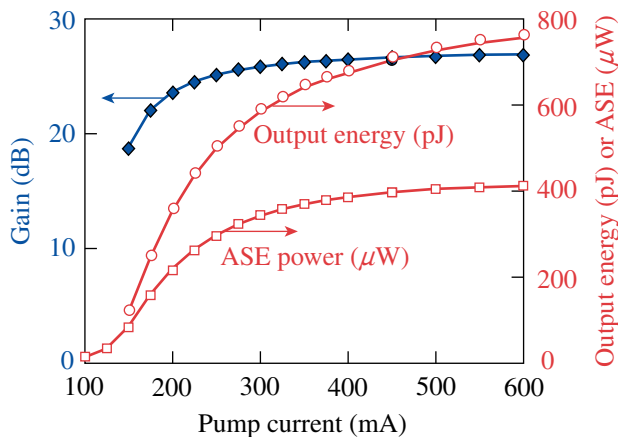
E13545JRC

Figure 106.5

Schematic of a high-gain, double-pass amplifier consisting of input and output isolators, a polarizing beam splitter (PBS), an ASE/signal wavelength division multiplexer (WDM1), two pump/signal wavelength division multiplexers (WDM2), 3.6 m of ytterbium-doped fiber, a Faraday mirror, and a 90/10 splitter. The Faraday mirror was a factory-aligned package containing a lens (L), Faraday rotator (FR), bandpass filter (F), and mirror (M). The polarization-maintaining fiber is notated by dotted lines while the single-mode fiber is notated in solid.

was determined to be near 3.5 m, regardless of the variability between components or splice quality. The pump utilized had a threshold of 16 mA and a slope efficiency of 0.68 mW/mA.

Figure 106.6 shows the signal gain, output energy, and total ASE power as a function of pump current. As the pump current is increased beyond 200 mA, the amplifier gain rolls off since the additional pump light is mostly not absorbed in the active fiber, a feature that is also reflected in the ASE curve. It is important to note that because of the low seed energy and repetition rate, the amplifier is unsaturated. Consequently, the



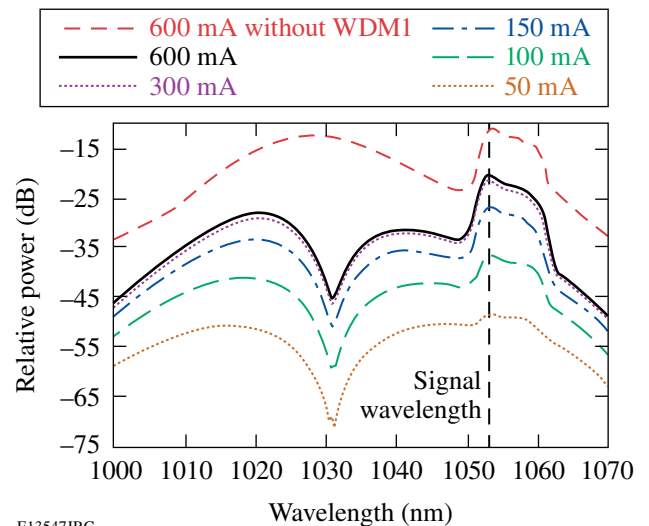
E14258JRC

Figure 106.6

Gain, output energy, and ASE power of the experimental amplifier described in Fig. 106.5 as a function of pump current.

small-signal gain afforded by this amplifier 23 nm off the gain peak is nearly 27 dB.

Self-pulsations were not observed at any pump currents because of the bandpass filter in the Faraday mirror assembly and the 1030-nm/1053-nm WDM that suppresses the stronger gain at shorter wavelengths. Figure 106.7 shows the ASE spectra of the double-pass amplifier for various pump current levels.



E13547JRC

Figure 106.7

Amplified spontaneous emission spectra from a dual-pass fiber amplifier for various pumping levels. Also shown are the seed wavelength at 1053 nm and the ASE trace for the amplifier without the 1030-nm/1053-nm WDM, which has been offset for clarity.

The seed wavelength is depicted by the vertical dashed line. The traces clearly show the double-pass gain of the wavelengths in the filter pass band compared to the single-pass gain of those outside the pass band. The top trace in Fig. 106.7, which is offset for clarity, is the ASE spectra for the double-pass amplifier without the 1030-nm/1053-nm WDM. This WDM, combined with the 10-nm bandpass filter, has a significant impact on both the output of the amplifier and the stability against lasing and self-pulsations, as evident in Fig. 106.7, and shows results very similar to the modeling results shown in Fig. 106.4.

It is difficult to define the noise floor of a system with regards to a low-repetition-rate signal. Simply comparing the strength of the signals on an optical spectrum analyzer requires an optical gate such that the spectrum is only integrated for the duration of the pulse. One alternative method compares the peak power of the amplified signal to the ASE power. A more meaningful metric that more accurately represents an optical signal-to-noise figure of merit compares the peak power of the amplified pulse to the ASE power in a limited spectral bandwidth around the seed-pulse wavelength. While the total noise floor is less than -28 dB across the entire operating range, the bandwidth-limited noise floor is better than -48 dB in a 0.1-nm bandwidth around the signal wavelength. Since the amplifier runs unsaturated, the noise floor is essentially constant as a function of pump current.

As mentioned previously, the combination of a Faraday mirror and polarizing beam splitter allows for high-fidelity separation of the input and output signals at the front end of the amplifier while maintaining the linear polarization state of the seed. The polarization extinction of the amplified signal was measured to be 19.9 dB, which is identical to that of the input signal.

Discussion and Conclusions

The pump is a grating-stabilized diode centered at 975.5 nm. The feedback from the fiber Bragg grating (FBG) maintains stable laser operation even in the presence of optical feedback, which can otherwise destabilize a diode laser.⁸ However, the amplified seed can be a problem in damaging the diode. Starting with a 2-pJ seed signal of 2-ns duration, the amplified signal becomes ~ 1 nJ. By some spurious reflection, a second round-trip through the double-pass amplifier is possible, leading to 0.5 μ J. Even in the presence of a pump/signal WDM, the fraction split off from this energetic pulse (~ 15 dB) leads to a pulse impinging on the face of the pump diode with an energy of 15 nJ and a peak power over 7 W. This can cause catastrophic optical damage on the facet of the laser diode

where the beam size is less than 10^{-7} cm². Two components in our system serve to eliminate this problem. The first is the output isolator, which significantly reduces the risk of a high-energy back-reflection into the amplifier. The second is the second pump/signal WDM, which serves as an ~ 15 -dB isolator of the signal pulse into the diode.

The agreement between measurements and simulations is favorable in the prediction of the noise characteristics of the amplifier, as shown in Table 106.III. In particular, using the ratio of small-signal gain over ASE power leads to an amplifier performance metric of 1161 per milliwatt, which agrees exceedingly well with the measurements. Both the signal gain and the ASE power levels were approximately 6 dB too high in the simulations, even when accounting for realistic component loss. There are several reasonable explanations for the discrepancy. First, there is the uncertainty in the loss due to the components and the splices. Second, the addition of the 10-nm filter in the Faraday mirror assembly may cause additional insertion loss due to slight perturbations in the propagation length and/or angle between the mirror and the fiber within the assembly. Finally, some of the parameters used in the simulations were simply taken from previous work.^{6,7} In particular, the emission and absorption cross sections can play a large role in determining the output performance of the amplifier. By varying the simulated emission cross section at 1053 nm, it is found that the ASE and gain change by 9.5% and 8.1%, respectively, for a 1% change in the emission cross section alone. Given the variability between measurements of ytterbium absorption and emission cross sections,^{7,9} this is likely a strong contributor to the mismatch in absolute values of gain and ASE power.

Table 106.III: Comparison of measured and simulated values for the double-pass fiber amplifier.

Characteristic	Measured Value	Simulation Result
Small-signal gain/ASE	1175/mW	1161/mW
Total noise floor	-28 dB	-30.6 dB
Noise floor in 0.1-nm bandwidth	-48 dB	-43.5 dB
Small-signal gain	26.6 dB	32.3 dB

The unpumped amplifier has a passive loss of approximately 15 dB. The simulations show an unpumped amplifier loss of 13.9 dB. While some of this loss is due to absorption in the

unpumped Yb-doped fiber, almost 9 dB of this loss is insertion loss of the constituent components. Many of these components are free-space optics that are packaged with fiber pigtails at the vendor. All-fiber components would certainly help to increase the gain of the system as well as the noise figure. The noise figure of the amplifier is given by¹⁰

$$NF = \frac{2P_{\text{ASE}}}{h\nu\Delta\nu_{\text{opt}}G}, \quad (3)$$

where P_{ASE} is the ASE power measured on a bandwidth $\Delta\nu_{\text{opt}}$, G is the signal gain, and ν is the optical frequency of the signal. Using measured parameters, the noise figure of the double-pass amplifier in a 0.1-nm bandwidth is 6.6 dB. Considering that the seed is degraded by 2.8 dB because of the insertion loss of the components before the active fiber, this result leads us to conclude that, in spite of operating far from the gain peak in a double-pass configuration, the amplifier is of extremely high quality because of the ASE suppression techniques utilized. Further, our model shows that our double-pass amplifier does not add any penalty to the noise figure, as has been observed in erbium-doped amplifiers used in a simple double-pass configuration.⁴

In conclusion, amplified spontaneous emission suppression techniques were utilized to fabricate a double-pass, ytterbium-doped amplifier with the noise properties of a single-pass amplifier. Simulations based on a rate-equation model were used to analyze the ASE and the impact of the suppression techniques. These techniques were implemented in an align-

ment-free, double-pass, ytterbium-doped fiber amplifier with 26-dB gain at a wavelength 23 nm off the gain peak and a -48-dB noise floor while amplifying linearly polarized optical pulses with a low duty cycle.

ACKNOWLEDGMENT

This work was supported by the U.S. Department of Energy Office of Inertial Confinement Fusion under Cooperative Agreement No. DE-FC52-92SF19460, the University of Rochester, and the New York State Energy Research and Development Authority. The support of DOE does not constitute an endorsement by DOE of the views expressed in this article.

REFERENCES

1. E. Desurvire, *Erbium-Doped Fiber Amplifiers: Principles and Applications* (Wiley, New York, 1994).
2. S. Hwang *et al.*, IEEE Photonics Technol. Lett. **13**, 1289 (2001).
3. A. Galvanauskas *et al.*, Opt. Lett. **26**, 935 (2001).
4. S. W. Harun, P. Poopalan, and H. Ahmad, IEEE Photonics Technol. Lett. **14**, 296 (2002).
5. L. L. Yi *et al.*, IEEE Photonics Technol. Lett. **16**, 1005 (2004).
6. Y. Wang and H. Po, J. Lightwave Technol. **21**, 2262 (2003).
7. R. Paschotta *et al.*, IEEE J. Quantum Electron. **33**, 1049 (1997).
8. R. W. Tkach and A. R. Chraplyvy, J. Lightwave Technol. **LT-4**, 1655 (1986).
9. N. A. Brilliant *et al.*, J. Opt. Soc. Am. B **19**, 981 (2002).
10. P. C. Becker, N. A. Olsson, and J. R. Simpson, *Erbium-Doped Fiber Amplifiers: Fundamentals and Technology* (Academic Press, San Diego, 1999).

The Development of Methods and Techniques for the Decontamination of Metals and Alloys

Background

Metallic components made of stainless steel, inconel, aluminum, and copper are routinely tritiated through the operation of tritium facilities. A significant disposal cost savings can be realized if the activity of the contaminated metals can be reduced below $0.5 \mu\text{Ci/g}$. The scope of this project was to determine the effectiveness of tritium removal, measure the residual tritium concentration, and establish the utility of the decontamination techniques in a tritium handling facility environment. To this end, metallic samples have been charged with tritium and stored in a helium environment for the study.

The proposed decontamination techniques were

- linear thermal desorption in an inert environment,
- linear thermal desorption using humidified inert gas,
- linear thermal desorption using inert gas containing different hydrogen peroxide concentrations, and
- radio-frequency–driven plasma decontamination using inert gas as the working medium.

This report describes the decontamination facilities and summarizes the efficacy of dry and humid thermal desorption, hydrogen peroxide decontamination, and radio-frequency–driven plasma decontamination.

Samples

A total of 57 low-carbon-content 316 stainless steel coupons have been contaminated with tritium gas for this study. The samples were not forged or polished, were cut into $2\text{-cm} \times 5\text{-cm} \times 0.5\text{-cm}$ -thick rectangles, and cleaned of oils and fingerprints using an acetone wash followed by a de-ionized water rinse. No heat treatment was applied to the samples before their exposure to HT gas at 375 Torr and 300 K for 105 h. The samples were charged with tritium in two batches. Following the dosing, the HT was evacuated and replaced with inert gas. The samples were individually wrapped in paper and then an

aluminum wrap and fixed in slots in the container so that the coupons could not touch each other or the container walls. All coupon handling was carried out in an inert gas environment.

Fourteen months later, the container was opened in a helium glovebox operating at a moisture level below the -60°C dew point. Twenty coupons were unwrapped and sealed in a separate container that was backfilled with air for future decontamination tests. The remaining coupons were transferred from the glovebox to the experiment as the need arose in groups of 2 to 4 in a sealed container backfilled with air. None of the coupons was exposed to air for more than 1 week before a desorption run.

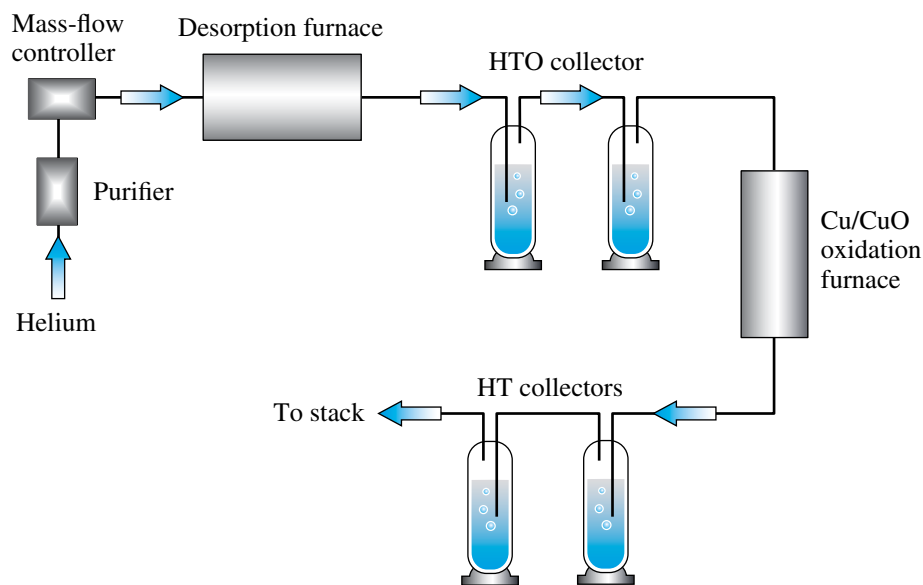
Experimental Facilities

1. Linear Thermal Desorption Facility

Linear thermal desorption (LTD) spectroscopy is an established diagnostic in the surface physics community that is used to study the nature of binding sites on surfaces. The target material is heated at a fixed linear rate from room temperature to some maximum value, usually of the order of 1100 K. The gas release rate from the surface is monitored and quantified as a function of the coupon temperature. The outgassing rate typically increases, peaks at one temperature, and then drops. The temperature at which the maximum desorption occurs depends on the linear heating rate and the binding energy for that species. A plot of the peak temperature against the heating rate can be used to extract the desorption energy. The technique has been used to study the release of tritium-labeled species from contaminated surfaces.^{1,2}

The LTD facility used in this work is illustrated in Fig. 106.8. A glass furnace outfitted with a heater, thermocouples, and associated support equipment accepts the dosed coupons for the thermal desorption study. Helium purges the furnace during the temperature ramp. The helium carrier is purified to parts per billion levels to preclude contamination of the desorbing species with organic compounds present in the carrier gas.

Effluent collection is an established experimental method for collecting volatile tritiated species.³ The technique quantifies



E14411JRC

Figure 106.8
Schematic of the linear thermal desorption facility.

the tritium release, segregates the airborne components into water-soluble and nonwater-soluble species, and permits limited resolution of the organic component released from surfaces.

Tritiated gas released from a dosed coupon is swept from the desorption furnace with the carrier to an array of water bubblers and a Cu/CuO furnace. The first two bubblers collect the water-soluble species and the second set collects the non-soluble species that have been oxidized to water in the Cu/CuO furnace. Bubblers are used in pairs to quantify the trapping efficiency of the upstream bubblers under the given operating conditions. Typically, the primary loss mechanism from each bubbler is the HTO transport in the humidified stream leaving the bubbler. The Cu/CuO furnace operates at 750°C to ensure high oxidation efficiency for volatile organic species, particularly tritiated methane. The entire system is fabricated from glass to minimize tritium retention on walls and catalytic exchange of HT to HTO on hot metal surfaces upstream of the Cu/CuO furnace. Each bubbler is equipped with a septum to permit on-line sampling of the water activity in each bubbler without disrupting the carrier flow. After the first four coupons were decontaminated, the bubbler immediately following the desorption furnace was fitted with an on-line liquid scintillation counter (LSC). The water in the bubbler was replaced with a liquid scintillation cocktail. A cocktail sample was continuously drawn from the bubbler at 1 ml/min, counted in a 0.2-ml detector, and returned to the bubbler. The activity profile was subsequently differentiated to extract the outgassing rate.

In these experiments, each bubbler was filled with 185 ml of liquid and the purge gas residence time in each bubbler was 3.7 min. The Cu/CuO oxidation furnace was periodically re-oxidized by passing air over the copper held at 750°C.

For humidity-stimulated desorption tests and for hydrogen peroxide-induced desorptions, the helium carrier was saturated with either liquid by passing purified helium through a bubbler containing one of the two liquids. The moist stream was blended with a dry helium stream to adjust the liquid content in the carrier entering the desorption furnace. The total helium flow rate was maintained at 50 ml/min for all experiments.

Before and after each LTD spectrum, the resident tritium inventory on the coupon was measured using the surface activity monitor (SAM) illustrated in Fig. 106.9

2. Surface Activity Monitor

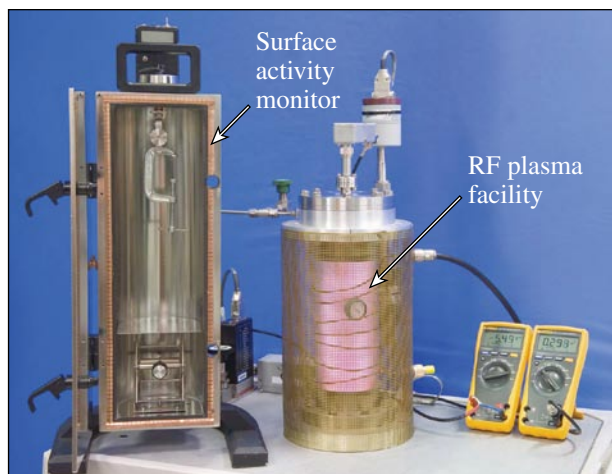
Surface activity monitoring is a nondestructive technique based on measuring a decay-beta-induced current emanating from a contaminated surface.⁴ The correlation between the emission current and surface activity has been established for metals and some nonmetals.⁵⁻⁷ Surface activities greater than 2 nCi/cm² can be measured by placing the detector on a contaminated surface. The detection limit of the device rests in the ability to build stable amplifiers that can measure down to 1 fA. Decay betas emanating from the subsurface regions of the metal and its attendant oxide layer are attenuated during their progression

into the air. Typically, the device is limited to tritium detection to a depth of the order of 0.1 μm in stainless steel.

In the current work, the surface activity monitor has been modified to measure the total activity of the coupon. In this case, the coupon is inserted into a Faraday cage and the total current released by the coupon is measured. While the minimum detection current is still restricted to 1 fA, the sensitivity of the device to measure the tritium concentration in a coupon will increase with increasing coupon surface area. In the current configuration, the SAM can accommodate a sample 30-cm long \times 10-cm wide.

3. Radio-Frequency–Driven Plasma Decontamination Facility

The decontamination facility⁸ is illustrated in Fig. 106.9. Coupons were positioned along the long axis of a cylindrical glass vessel and electrically disconnected from the ground. A low-temperature, Tonks–Langmuir, argon plasma was struck between the coupons and the glass wall. The electric potential that developed on each coupon while it was immersed in the plasma was allowed to float at the plasma potential. The working neutral gas pressure was 50 mT. Desorbed species were removed from the vicinity of the coupon by purging the 1.6-liter cylindrical volume with argon at 0.5 Torr-L/s. After each plasma exposure, the coupon was removed and its residual tritium inventory was measured with the SAM. During the longer exposures, the coupon temperature gradually increased from 300 K to 340 K but never exceeded 340 K. Both the floating voltage and the current to ground were monitored in real time during each plasma exposure.



E14412/JRC
Figure 106.9
Photograph of the surface activity monitor and the radio-frequency–driven plasma decontamination facility.

Results

1. Data Overview

The decontamination protocols used during this study are summarized in Table 106.IV.

Bubbler 1 and 3 data, the lead bubbler in each set, were collected manually for coupons 1 through 4 by taking a 0.5-ml aliquot according to the sampling rate listed in Table 106.V.

All subsequent B1 data was collected continuously with the in-line liquid scintillation counter described earlier. Periodically, 0.5-ml aliquots of the liquid scintillation cocktail were extracted from bubbler 1 to cross-reference against a calibrated

Table 106.IV: Decontamination protocol used for each coupon.

Coupon number	Desorption furnace ramp rate ($^{\circ}\text{C}/\text{min}$)	Purge stream component	Concentration (ppm)
1	10	Dry	
2	10	Dry	
3	5	Dry	
4	5	Dry	
5	5	Dry	
6	2.5	Dry	
7	2.5	Dry	
8	1.5	Dry	
9	1.5	Dry	
10	1.5	Dry	
11	1.5	Dry	
12	1.5	Dry	
13	1.5	H ₂ O	3210
14	1.5	H ₂ O	9630
15	Steps	H ₂ O	16053
16	Steps	H ₂ O ₂	310
17	Steps	H ₂ O ₂	1550
18	Steps	Dry	
19	RF decontamination		
20	RF decontamination		

Table 106.V: Sampling rate dependence on the furnace ramp rate.

Ramp rate ($^{\circ}\text{C}/\text{min}$)	Sample interval (min)
10	5
5	10
2.5	15
1.5	20

liquid scintillation counter. Figure 106.10 summarizes the evolution of “soluble” activity collected from the first 12 coupons that are listed in Table 106.IV. The evolutions were normalized by the total “soluble” activity collected to permit a comparison of the evolution profiles. These profiles, which are shown in Fig. 106.10, exhibit a dependence on the temperature ramp rate because the coupon temperatures are inferred from the furnace temperature. For example, for a ramp rate of 2°C, the difference between the furnace and coupon temperatures peaks at 20°C. For a 10°C ramp rate, that difference increases to 80°C. In Fig. 106.10, the normalized release profiles were all observed to steepen as the ramp rate decreased from 10° to 1.5°C/min. These curves indicate that most of the activity is released between 200°C and 350°C.

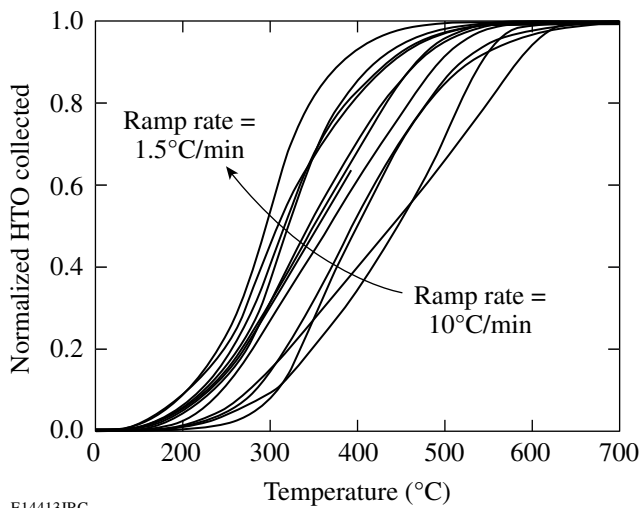


Figure 106.10 Normalized activity of bubbler 1 as a function of furnace temperature.

During these tests, the trapping efficiencies of bubbles 1 and 3 exceed 99.8% except at low bubbler activities where measurement errors are large. If bubbles 2 and 4 have similar collection efficiencies, then less than 4×10^{-6} of the soluble activity entering the first bubbler set will contribute to the activity in the bubbler set following the furnace. Additionally, less than 4×10^{-6} of the activity leaving the furnace escapes the desorption facility. Water soluble and nonsoluble activity released by the coupons is effectively separated by the two bubbler sets at a 50-ml/min helium purge rate. Random sampling of the effluent leaving the fourth bubbler with a portable ionization chamber confirmed that no measurable activity was escaping capture in the desorption facility.

Switching from water to a liquid scintillation cocktail in bubbler 1 to permit on-line monitoring of the activity reduced

the trapping efficiency of this bubbler to 95% at high water loadings in the cocktail. Nevertheless, and in part because the second bubbler continued to use water as the capture medium, the total transfer of water-soluble activity to the bubbler set following the furnace only increased by 25-fold, from 4×10^{-6} to 1×10^{-4} . At this overall trapping efficiency and assuming that the water-soluble component is 100 times larger than the insoluble fraction, the water-soluble contribution to the insoluble fraction will represent a 1% overestimate in the nonsoluble activity.

Water vapor is continuously transferred from upstream bubblers toward downstream bubblers. The concomitant rate of activity loss from the upstream bubbler was observed to match the rate of activity accumulation in the second bubbler for both bubbler sets. This indicates that the trapping efficiency of each bubbler was limited by HTO transport from bubbler to bubbler rather than by an inefficient activity transfer from the helium purge stream into the bubbler fluid.

The activity and split between soluble and insoluble components for all decontaminated coupons are presented in Table 106.VI. The coupons are listed in the order in which

Table 106.VI: Summary of the activities and the fraction of soluble and insoluble components collected from each coupon.

Run	HTO (μCi)	HT (μCi)	Total (μCi)	% HTO/total
1	665	176	841	79
2	690	113	803	86
3	1331	92	1424	94
4	902	137	1039	87
5	1080	70	1149	94
6	1018	103	1120	91
7	945	53	998	95
8	1086	34	1120	97
9	854	35	889	96
10	741	6	747	99
11	665	11	676	98
12	1358	26	1384	98
13	1387	37	1424	96
14	931	26	957	97
15	N/A			
16	2228	98	2326	96
17	551	87	638	86
18	895	60	955	94
Average			1088	94

they were desorbed. Equipment failure during the processing of coupon 15 has led to some questionable results; those values are not presented in the table. Results from detritiating coupon 1 and, to a lesser extent, coupon 2, are skewed toward a higher activity collection in the bubbler set following the furnace because residual activity released from the furnace has contributed to the activity collected in the second bubbler set. Disregarding the coupon-1 data, 94% of the total activity released by the coupons is water-soluble and assumed to be HTO for the present discussion. The mean activity collected from each coupon was 1.1 ± 0.4 mCi.

2. Linear Thermal Desorption in Dry Helium

The evolution of each activity profile from bubbler 1 has been smoothed with a running average that spans six data points, differentiated with respect to time, and normalized by dividing the differentiated curve by the total tritium collected from that coupon. The resulting outgassing curves for four coupons are provided in Fig. 106.11 to compare the sample-to-sample variation in the outgassing rate that can be expected for identical desorption conditions.

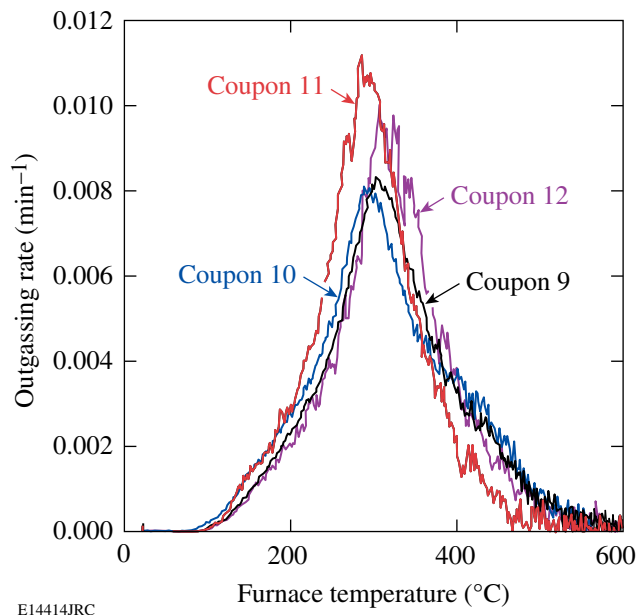


Figure 106.11
Sample-to-sample variation in the outgassing rate for identical desorption conditions at 1.5°C/min.

The on-line monitoring system collects and records the activity of bubbler 1 every minute. Consequently, the running average used to smooth the data spans a 6-min period. The purge gas residence time in bubbler 1, the mean contact time of the bubbles in the liquid, is 3.7 min at 50 ml/min. The rate

of absorption of HTO into the liquid scintillation cocktail is exponential with a time constant determined by the interfacial area of the bubble (area/volume), overall mass transfer coefficient, and time the bubble spends in the fluid. Given the high trapping efficiency, it is reasonable to assume that the majority of the activity is removed in the first half of the bubbler and that the stirring to equilibrate the activity within the bubbler by the action of bubbles floating to the liquid surface will exceed the gas residence times by at least a factor of 2. Averaging over 6 min should accurately reflect the mean bubbler activity at any given moment in time. The fluctuations in liquid activity seen in Fig. 106.11 are attributed to local variations in the fluid activity arising from the random passage of bubbles close to the LSC sampling point. Similar fluctuations are evident in the activity for the two samples desorbed at 2.5°C/min in dry helium, as shown in Fig. 106.12. The run-to-run variation in the outgassing measurement is less than 20% in both examples.

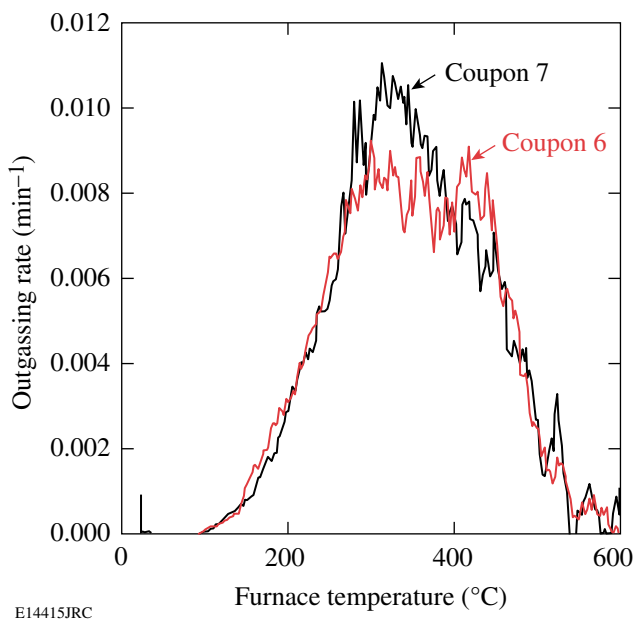


Figure 106.12
Sample-to-sample variation in the outgassing rate for identical desorption conditions at 2.5°C/min.

The normalized outgassing rate dependence on the temperature ramp rate of the desorption furnace is provided in Fig. 106.13. Three features are evident.

The profiles become progressively more skewed as the ramp rate increases. This suggests that the desorbing species did not have time to equilibrate with the surface during desorption at the higher ramp rates. The skewed evolution profiles may be more representative of the release of the actual species bound to

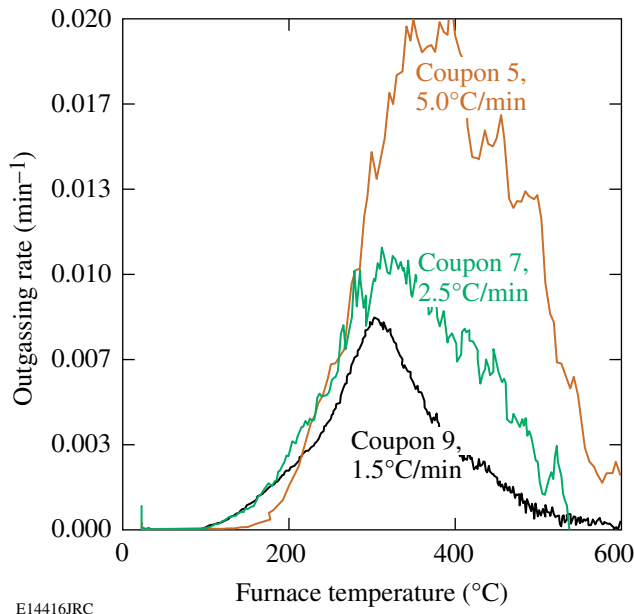


Figure 106.13
The outgassing rate dependence on the temperature ramp rate of the desorption furnace for coupons 5, 7, and 9.

the surface. That is, either different species or the same species with different surface-binding energies are being released at the higher ramp rates without thermally accommodating with the surface before release. In contrast, the symmetric profile evident in the 1.5°C/min ramp rate case suggests that surface-bound species can migrate on the surface to lower energy states before release to the gas phase.

The shift in the desorption peaks as one proceeds to higher ramp rates is an artifact of the experimental setup, as discussed earlier.

Finally, the normalized outgassing rate increase with increasing ramp rate is a consequence of limited activity on the surface. As discussed in **Data Overview** (p. 72), the total activity released from each coupon was of the order of 1.1 mCi. As a result, increasing the ramp rate requires a commensurate increase in the outgassing rate if the total quantity of material released is to remain constant.

3. Thermal Desorption in a Helium Stream Bearing H₂O

The normalized outgassing rate from coupons soaked at fixed temperatures while exposed to a helium purge containing 0- and 16050-ppm water is provided in Figs. 106.14 and 106.15, respectively.

These figures indicate that the preponderance of the activity is released between 100°C and 300°C. Furthermore, a

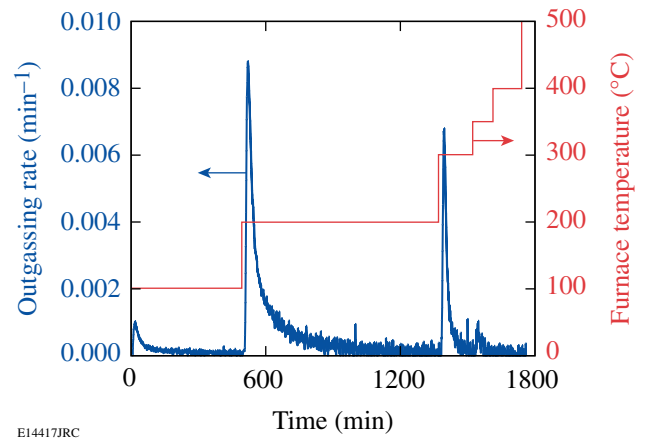


Figure 106.14
The outgassing rate dependence on the temperature of the desorption furnace in a dry helium purge. Coupon 18 contained 0.96 mCi.

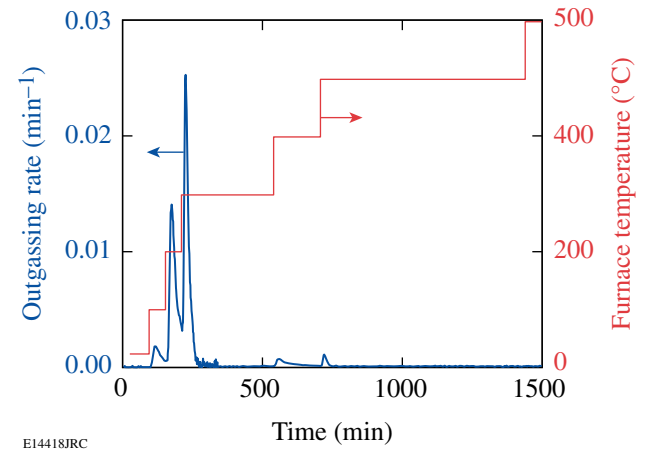


Figure 106.15
The outgassing rate dependence on the temperature of the desorption furnace in a wet helium purge. Coupon 15 contained 0.69 mCi. The helium purge rate was 50 ml/min, with a water content of 16050 ppm.

comparison of the two figures suggests that the presence of water in the helium purge stream stimulates tritium release at all temperatures. That removal rate appears to be limited by diffusion from the subsurface to the surface. At all temperatures, once the near-surface tritium has been depleted, the activity outgassing rate reduces to zero. Increasing the coupon temperature from 200°C to 300°C increases the tritium diffusion rate to the surface, as expected. Increasing the coupon temperature beyond 300°C does not noticeably increase activity release in the dry helium purge case, but it does stimulate the release of more tightly bound residual

activity when water vapor is present in the purge stream. Increasing the coupon temperature to 500°C results in negligible additional activity release in both cases. The residual activity following each bakeout is negligible in both cases based on SAM measurements.

4. Thermal Desorption in a Helium Stream Bearing H₂O₂

The normalized outgassing rate from coupons soaked at fixed temperatures while exposed to a helium purge containing 310- and 1550-ppm hydrogen peroxide is provided in Figs. 106.16 and 106.17, respectively.

In both cases, at coupon temperatures below 150°C, the outgassing rate is rate controlled by tritium diffusion from the subsurface to the solid/gas interface as for the dry and humid

helium purge runs. Above 150°C, however, activity removal decreases with the logarithm of time, suggesting the rate-limiting step is peroxide transport to the reaction zone. Furthermore, the reaction rate increases with increased hydrogen peroxide concentrations. Negligible activity is removed beyond a coupon temperature of 250°C.

To illustrate these observations more clearly, the two outgassing curves have been overlaid on the semilogarithmic curve provided in Fig. 106.18. The diffusion-limited outgassing regime below 150°C is evident for both coupons. In the 1550-ppm case, however, activity is removed approximately threefold more aggressively than in the 310-ppm case. Above 150°C, the reaction rate depends on the logarithm of time, doubling for a fivefold increase in hydrogen peroxide concentration.

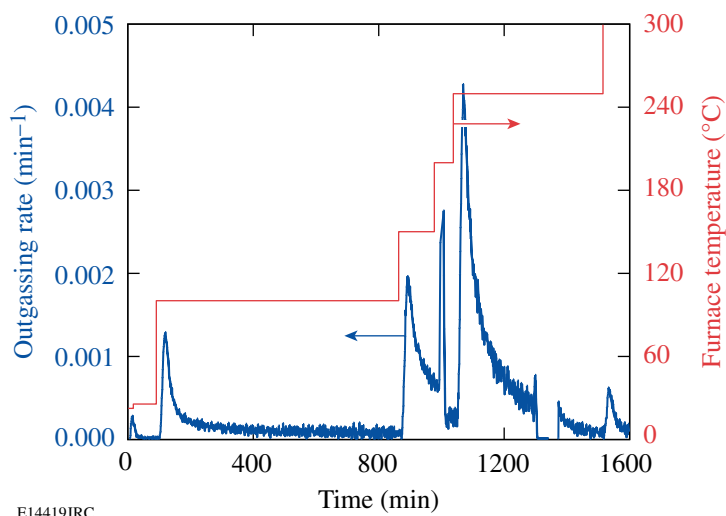


Figure 106.16
The outgassing rate dependence on the temperature of the desorption furnace in a helium purge containing 310-ppm hydrogen peroxide. Coupon 16 contained 2.33 mCi.

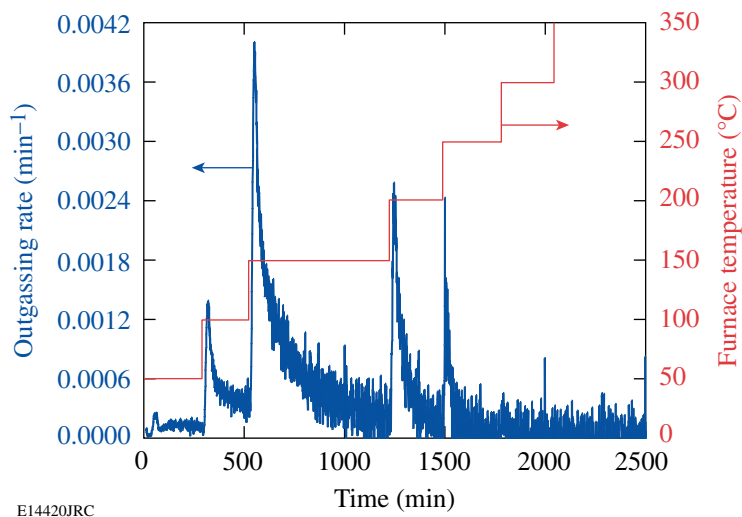


Figure 106.17
The outgassing rate dependence on the temperature of the desorption furnace in a helium purge containing 1550-ppm hydrogen peroxide. Coupon 17 contained 0.64 mCi.

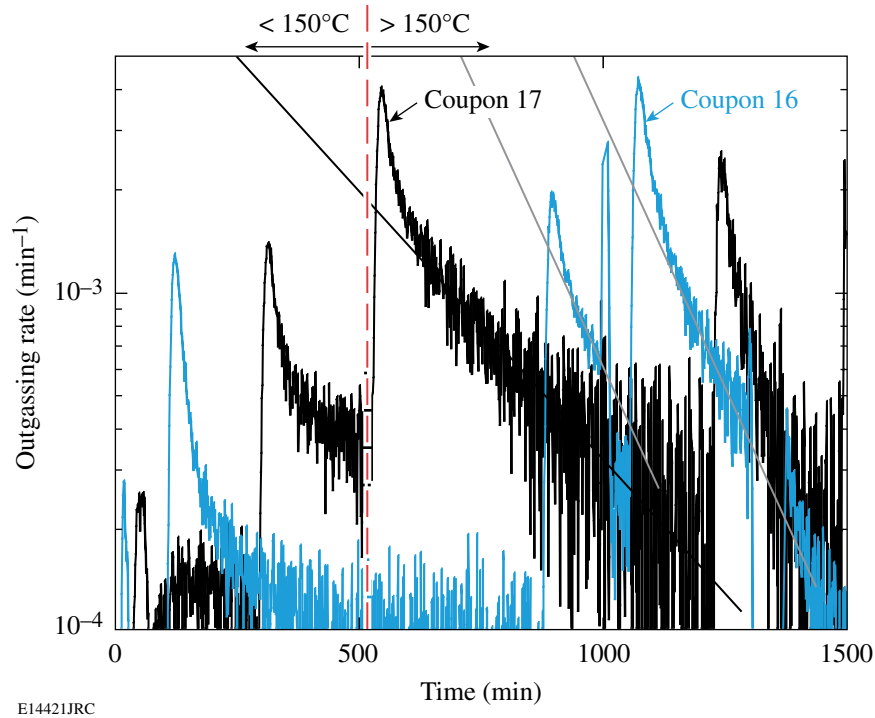


Figure 106.18
The outgassing rate dependence on both coupon temperature and hydrogen peroxide concentration.

5. Correlation Between SAM and LSC Measurements

A continuous beta flux emanates from a tritiated metallic surface. This flux is uniquely related to the near-surface tritium concentration

$$I_{\text{sat}} = \frac{A}{2W} \int_0^{E_T} eE\Phi(E)dE, \tag{1}$$

where A is the emitting area, W is the mean energy invested in forming ion pairs (33.7 eV/ion pair in air at 1 bar), e and E are the electronic charge and the energy of the decay electron, respectively, and $\Phi(E)$ is the energy distribution of the flux emanating from the surface. The factor of 2 accounts for the half of the decay electrons that are emitted in the direction of the metal bulk and cannot contribute to ion-pair formation in the air.

In the limit where the tritium resides on the surface or in the proximity of the surface, i.e., the attenuation of the decay electron energy before the electrons reach the air interface can be neglected, Eq. (1) simplifies to

$$I_{\text{sat}} = \frac{eE_m}{2W} \lambda n_s,$$

where n_s is the number of tritium atoms on the surface decaying at the rate λ to emit an electron stream of mean energy E_m (5.7 keV). Introducing the numeric values,

$$I_{\text{sat}} = \frac{1.602 \times 10^{-19} \times 5700}{2 \times 33.7} \lambda n_s \tag{2}$$

$$= 0.0135 \lambda n_s, \tag{3}$$

where λn_s is the activity on the surface in becquerels and I_{sat} is measured in femtoamperes (fA), or

$$I_{\text{sat}} = 0.5007 \lambda n_s, \tag{4}$$

where λn_s is expressed in nanocuries and I_{sat} is in femtoamperes.

This current is collected on the anode in the SAM, boosted in one of two ranges by an onboard transimpedance amplifier, and displayed as a voltage. The transfer function for the two ranges is

$$V(\text{mV}) = 0.196 \times I(\text{pA}) \tag{5}$$

on scale 1 and

$$V(\text{mV}) = 0.212 \times I(\text{fA}) \quad (6)$$

on scale 2. Both ranges have been calibrated against a NIST-traceable standard for this work.

Substituting for the current in Eqs. (4) and (5) and Eqs. (4) and (6) yields

$$\lambda n_s = 10.2 \times V(\text{mV}) \quad (7)$$

microcuries on scale 1 and

$$\lambda n_s = 9.43 \times V(\text{mV}) \quad (8)$$

nanocuries on scale 2.

The activity of each coupon was measured before and after treatment in the SAM, and the surface activity was estimated using either Eq. (7) or (8). Table 106.VII compares SAM measurements with the total activity collected by the bubblers.

Table 106.VII: Comparison of the SAM measurements with the total activity collected for each coupon.

Run	Total (μCi)	SAM (μCi)	% SAM/total
1	841	632	75
2	803	588	73
3	1424	N/A	
4	1039	698	67
5	1149	764	66
6	1120	813	73
7	998	662	66
8	1120	842	75
9	889	682	77
10	747	511	68
11	676	499	74
12	1384	835	60
13	1424	740	52
14	957	513	54
15	N/A	527	
16	2326	1113	48
17	638	434	68
18	955	654	68

This data is displayed in Fig. 106.19 with its estimated error. The error in the SAM data is taken to be of the order of 2% of

the value. The error in the LSC data is expected to reach up to 10% of the value. The primary source of error in the LSC data is a sampling error. The liquid activity was sampled by extracting 0.5 ± 0.05 -ml aliquots for counting. Systematic errors are assumed to be negligible compared to the sampling error since both measurement techniques rely on differing principles and both measurement schemes have been independently calibrated. If the origin is included in the linear regression analysis, the SAM registers 70% of the LSC value with a correlation of 0.93 and a 10% offset in slope. If the origin is not included, the SAM registers 70% of the LSC value with a 20% offset in slope and a 0.84 correlation coefficient. In either case, approximately 70% of the total activity collected from the coupon is visible to the SAM.

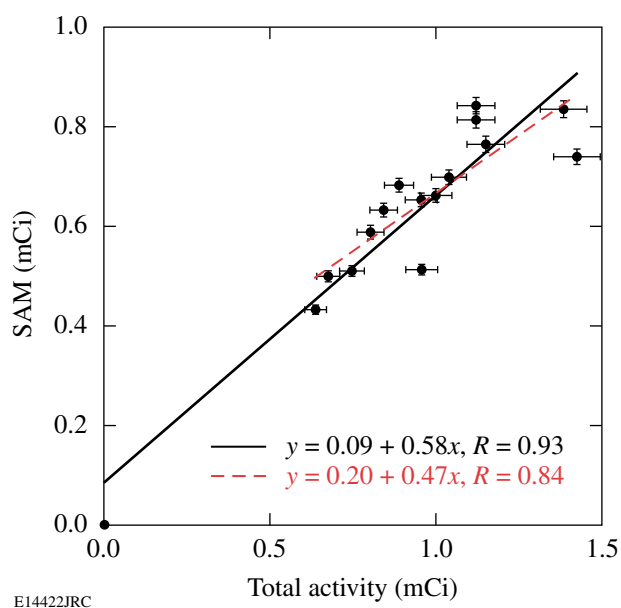


Figure 106.19
Surface activity correlation between SAM measurements and LSC data for each coupon.

The range of 5.7-keV electrons decreases from 400 nm in water to 50 nm in stainless steel. More energetic 18.6-keV electrons will reach 5000 nm in water and 600 nm in stainless steel. If we idealize the stainless surface as a metal covered with 100 monolayers of water and each layer is approximately 0.3 nm thick, then the water layer on the surface will be of the order of 30 nm thick. All decay electrons originating from the water layer will contribute to the surface activity measurement. Additionally, electrons originating from the water-metal interface will reach the air-water interface with some attenuation while electrons originating at a depth of

50 nm with energies below 5.7 keV will not contribute to the SAM measurement. The SAM to LSC ratio in Fig. 106.19 suggests that approximately 70% of the tritium desorbed from the coupon resides in areas shallower than 50 nm in the stainless steel.

For exposures of the order of an hour and at room temperature, most of the tritium will reside in the water layers on the metal or close to the water-metal interface in the stainless steel.⁹ The amount of tritium sorbed on a room-temperature stainless steel coupon is directly proportional to the exposure time¹⁰ until, in effect, each resident water molecule bound to the surface is labeled with a triton; that is, the mean surface activity reaches 48 $\mu\text{Ci}/\text{cm}^2$. Under these exposure conditions, about 10% of the tritium penetrated approximately 100 nm into the metal. More recent experiments indicate that tritium can diffuse up to 400 μm into the metal¹¹ and that the tritium concentration in the metal drops off with the error function of the square root of the diffusivity time product when the exposure temperature is above 370 K, in accordance with the classical equations for hydrogen diffusivity in metals. Below 370 K, classical diffusion based on lattice diffusivity does not appear to apply. Presumably, grain-boundary and triple-point diffusion contribute more significantly to the total hydrogen transport into the metal.

SAM measurements are linearly related to the surface/near-surface activity, as discussed previously. Earlier studies referenced in this article indicate that sample-to-sample variations are small for samples exposed under identical conditions. The variability between the SAM and LSC measurement data observed in the current sample set is attributed to coupon handling following exposure. As discussed, 70% of the tritium resides in the top 50 nm of the surface. Up to 10% of the activity in this layer could be removed with a single coupon handling. The action of wrapping and unwrapping the coupons can easily represent a variation of 20% in the surface-activity measurement. The deviation between the linear regression provided in Fig. 106.19 and each SAM measurement listed in Table 106.VII has been expressed in a percentage of the expected SAM measurement and plotted against the total coupon activity in Fig. 106.20. The measurements fluctuate about the linear regression value for each measurement with the range +16%/-21%, as expected.

6. Radio-Frequency-Driven Plasma Decontamination

The effectiveness of using a plasma discharge to decontaminate tritiated metal is illustrated in Figs. 106.21 and 106.22. In these tests, each coupon was removed from storage under

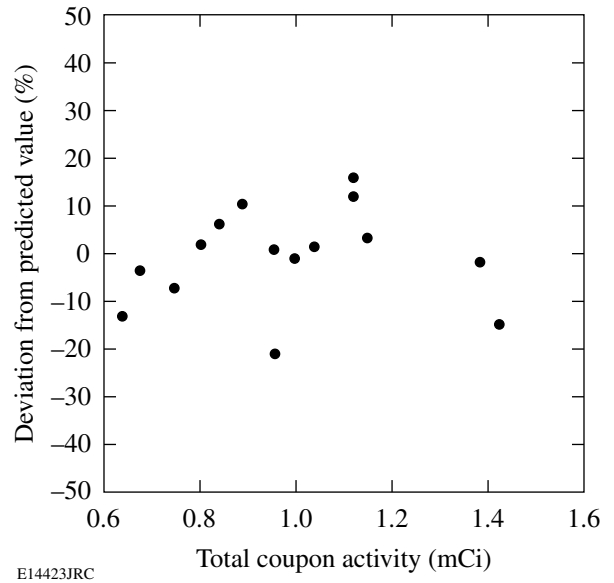


Figure 106.20
Deviation of individual SAM measurements from the expected SAM measurement for a range of coupon activities.

helium gas, its surface activity measured using the SAM, and then transferred to the decontamination chamber shown in Fig. 106.9. During the measurement and transfer, the coupon was exposed to air for approximately 5 min. The decontamination chamber was evacuated, an argon purge through the chamber initiated, and the discharge struck. The time during which the coupon was exposed to a plasma increased from

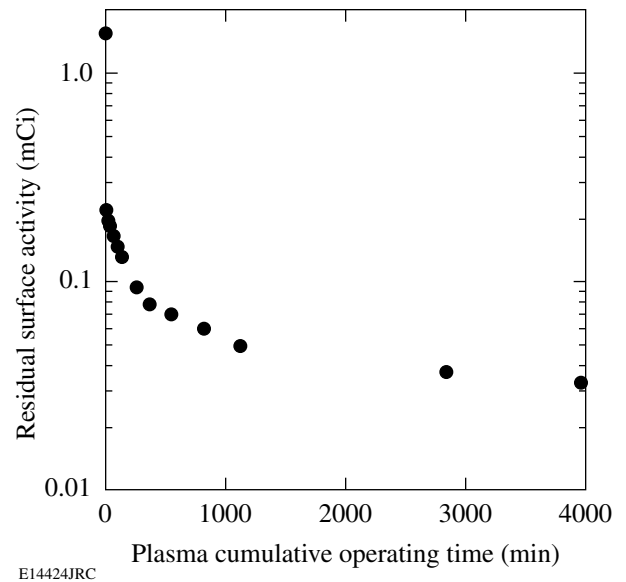


Figure 106.21
Residual surface activity following exposure to RF-driven plasma.

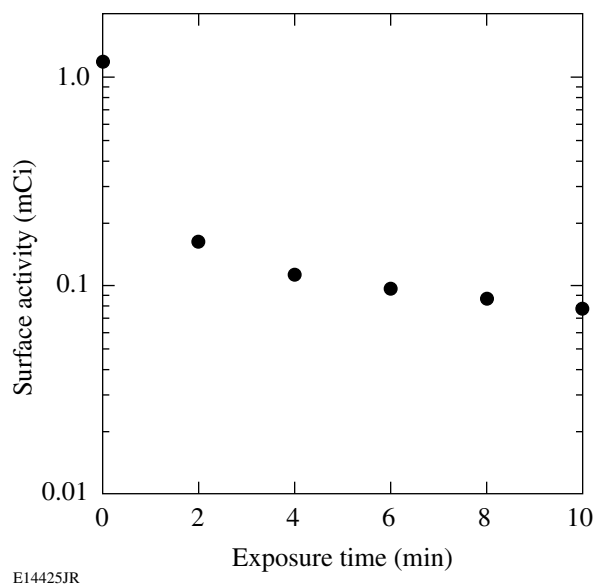


Figure 106.22
Residual surface activity following 2-min exposures to RF-driven plasma.

7 min in the first exposure to 18.7 h in the last. The original surface activity and the activities immediately following each exposure are plotted as a function of cumulative exposure in Fig. 106.21.

This figure illustrates that 86% of the surface activity is removed in the first 7 min of plasma exposures. After almost 4000 min of additional exposure, 2% of the original activity remains in the coupon.

Figure 106.22 illustrates the rate of activity removal for sequential 2-min plasma exposures of a second coupon under the same discharge conditions used for the previous sample. This figure indicates that 86% of the initial surface activity is actually removed within the first 2 min of exposure.

An argon discharge in a 10-cm-diam cylinder with a neutral pressure of 50 mTorr will support an electron temperature approaching 30,000 K and a sheath potential of 1.2 eV. Argon-neutral atoms and ions will bombard a coupon immersed in this plasma with an average energy of 1.2 eV. During the tests illustrated in Figs. 106.21 and 106.22, the ion current drawn by the coupon was of the order of 1 mA. Equivalently, particles struck the coupon surface at the rate $1 \times 10^{-3}/1.6 \times 10^{-19} \approx 6 \times 10^{15}$ particles/s.

The hard sphere radius of water is 0.145 nm. Each monolayer of water on the coupon surface will contain 1.5×10^{15} particles/cm² $\times 27$ cm² (the coupon surface area) $\approx 4 \times 10^{16}$ particles.

If we assume the coupon is covered with approximately 30 monolayers (ML) of water,[†] then the number of water molecules desorbed from the surface during a 2-min discharge per incoming argon atom will be

$$\frac{30 \text{ ML} \times 4 \times 10^{16} \#/\text{ML}}{2 \text{ min} \times 60 \text{ s/min} \times 6 \times 10^{15} \text{ ions/s}}$$

This relationship suggests that 1.7 water molecules are released per argon ion.

Typically, the first layer of water bonds to the metal surface via the lone pair electrons with an energy of the order of 0.4 to 0.7 eV. That is, those electrons not involved in the hydrogen bonding are shared with the metal surface so that the water molecule is oriented with the oxygen facing the surface and the two hydrogen atoms pointed away from the surface. All additional water layers are held to the surface via hydrogen bonds to the first layer molecules with energies of the order of 0.2 to 0.3 eV per bond. The O-H dissociation energy is 5.18 eV. Argon ions from the plasma drop through the sheath, increase their energy from roughly 0.03 eV to 1.2 eV, and deposit that energy on the coupon surface. On average, this energy can break up to four water-to-surface bonds, a fraction of which would be released from the surface. Water desorption is preferred to water dissociation.

The estimated release of 1.7 water molecules per incoming argon ion is consistent with the observations provided in Figs. 106.21 and 106.22. Both figures show that the tritium removal efficiency drops rapidly following the first 2 min. The removal rate is no longer argon ion flux limited but tritium atom supply limited. Tritium must first diffuse to the metal surface before it can be removed from the coupon. This suggests that heating the coupon would accelerate tritium removal during this phase of the decontamination. The discharge is a highly efficient method for removing tritiated water from a metal surface.

Summary and Conclusions

The efficacy of removing tritium from stainless steel surfaces using the following four different approaches has been studied:

- thermal desorption in a dry purge
- thermal desorption in a wet purge

[†]Stainless steel exposed to ambient air with a relative humidity in the vicinity of 40% to 50% will contain up to 100 monolayers of water. The time for the water content on a surface to equilibrate with the water vapor pressure in the air is of the order of a few seconds.

- thermal desorption in a purge containing hydrogen peroxide
- radio-frequency–driven argon plasma irradiation.

Thermal desorption experiments indicate that the averaged activity desorbed from each coupon was 1.09 mCi. A standard deviation of 0.4 mCi in these measurements is attributed to coupon handling during the wrapping and unwrapping of individual coupons.

The activity of each coupon was measured using a surface activity monitor. The SAM measured 70% of the actual tritium desorbed from the coupons. This suggests that 30% of the tritium resides deeper than 600 nm in the metal matrix before decontamination. Such penetration depths are consistent with the 105-h exposure durations used to prepare the coupons. More than 80% of the tritium desorbed from the coupons was released as a water soluble.

It appears that some tritium diffuses from depths below 50 nm, i.e., from the metal bulk during the decontamination process, most likely as atoms, recombines with hydroxyls at the surface or isotopically exchanges with molecular water still resident on the surface, and then desorbs.

Desorption in a dry helium purge is tantamount to boiling molecular water from the coupon surface. A minimum metal temperature of 600°C is required to remove the bulk of the tritium. SAM measurements following the high-temperature desorptions do not indicate the presence of tritium. Based on Eq. (8), the mean-surface/near-surface activity to a depth of 200 nm into the metal must be less than

$$\frac{9.43 \text{ nCi/mV} \times 0.25 \text{ mV}}{27 \text{ cm}^2 \times 200 \text{ nm} \times 9 \text{ g/cc}} = 485 \text{ nCi/g} = 0.5 \text{ } \mu\text{Ci/g},$$

where 0.25 mV is the minimum detectable voltage that can be measured with certainty. This value represents the SAM's detection limit for these coupons.

Desorption in a wet helium purge also approximates boiling molecular water from the coupon surface. Nevertheless, the presence of water promotes some activity release. The higher normalized outgassing rates observed in the presence of water vapor are most likely attributable to isotopic exchange at the metal surface. Negligible tritium release is observed above 500°C. As in the dry helium purge case, the rate-limiting step in activity removal appears to be tritium diffusion from the water layers or the metal bulk.

At 100°C and for low hydrogen peroxide concentrations, activity removal from the coupon surface follows the same rate-limiting mechanism observed under dry and moist purge conditions, i.e., tritium diffusion through the metal oxide layers. Increasing the hydrogen peroxide concentration fivefold to 1550 ppm without changing the coupon temperature shifts the rate-limiting mechanism from diffusion through the metal oxide to hydrogen peroxide arrival at the metal surface. Negligible activity remains in a coupon following a decontamination using a 1550-ppm hydrogen peroxide-doped helium purge over a coupon heated to 250°C.

Radio-frequency–driven plasma decontamination removes the layers of molecular water extremely rapidly. Subsequently, diffusion from the metal bulk limits the rate of activity removal. It appears that the overall time needed to decontaminate metal with this approach can be realized with an initial exposure to the plasma at room temperature followed by additional plasma exposures at elevated metal temperatures.

This study has shown that water or water-soluble components represent the majority of the activity released from metal exposed to tritium gas for 105 h. Earlier studies have shown similar results for short exposure durations. Additionally, most of the tritium that has diffused into the bulk returns to the surface, recombines with hydroxyl radicals, and is released as water. Some of the re-emergent tritium combines with hydrogen and is released as HT.

ACKNOWLEDGMENT

This work has been carried out at the University of Rochester under the United Kingdom Atomic Energy Authority Contract #3000000092, formerly contract #C011840. This work was supported by the U.S. Department of Energy Office of Inertial Confinement Fusion under the Cooperative Agreement No. DE-FC52-92SF19460, the University of Rochester, and the New York State Energy Research and Development Authority. The support of the DOE does not constitute an endorsement of the views expressed in this article.

REFERENCES

1. Y. Belot, H. Camus, S. Raviart, A. B. Antoniazzi, and W. T. Shmayda, *Fusion Technol.* **28**, 1138 (1995).
2. A. B. Antoniazzi and W. T. Shmayda, *Fusion Technol.* **26**, 673 (1994).
3. W. T. Shmayda, A. B. Antoniazzi, and R. A. Surette, Ontario Hydro Research Division, Toronto, Canada, Report No. 92-51-K (1992).
4. W. T. Shmayda, N. P. Kherani, and D. Stodilka, in *Fusion Technology 1996*, edited by C. Varandas and F. Serra (Elsevier, Amsterdam, 1997), pp. 1245–1248.
5. N. P. Kherani and W. T. Shmayda, *Fusion Technol.* **28**, 893 (1995).

6. W. T. Shmayda and N. P. Kherani, U.K. Patent No. 2,301,222 (11 August 1999).
7. C. R. Shmayda, W. T. Shmayda, and N. P. Kherani, *Fusion Sci. Technol.* **41**, 500 (2002).
8. A. B. Antoniazzi and W. T. Shmayda, in *Fusion Technology 1992*, edited by C. Ferro, M. Gasparotto, and H. Knoepfel (Elsevier Science Publishers B.V., Amsterdam, 1993), pp. 1680–1684.
9. N. P. Kherani, D. Stodilka, and W. T. Shmayda, Ontario Hydro Technologies, Toronto, Canada, Report No. A-IT-96-52-CON (1996).
10. N. M. Masaki, T. Hirabayashi, and M. Saeki, *Fusion Technol.* **15**, 1337 (1989).
11. A. N. Perevezentsev *et al.*, *Fusion Sci. Technol.* **48**, 208 (2005).

Basic Principles of Direct-Drive Ignition Target Design

Introduction

Inertial confinement fusion (ICF) is an approach to fusion that relies on the inertia of the fuel mass to provide confinement. The confined fuel must reach a high temperature and density to produce enough $D + T \rightarrow \alpha(3.5 \text{ MeV}) + n(14.1 \text{ MeV})$ reactions so that the total energy released is much larger than the driver energy required to compress the fuel. The capsule in an ICF implosion, which is a spherical cryogenic deuterium–tritium (DT) shell filled with DT vapor, is irradiated directly by laser beams (direct-drive approach) or by x rays emitted by a high-Z enclosure (hohlraum) surrounding the target (indirect drive).¹ Only a small portion of the fuel is heated to ignition conditions in a typical ignition target. This part of the fuel forms a hot spot that initiates a burn wave that ignites the remaining fuel. In the direct-drive approach, the following stages of an implosion can be identified: At the beginning of the laser pulse, the outer portion of the pellet heats up and expands outward, creating a plasma atmosphere around the pellet. Then a critical electron density $n_{cr} = \pi m c^2 / e^2 \lambda_L^2$ is established outside the cold portion of the shell, where m is the electron mass, c is the speed of light, e is the electron charge, and λ_L is the laser wavelength. The laser energy is absorbed in a narrow region near the critical surface via the inverse bremsstrahlung, and the absorbed energy is transported, mainly by electrons, toward the colder portion of the shell. The cold material, heated by the thermal conduction, expands outward. Such an expansion creates an ablation pressure that, similar to the rocket effect, compresses the pellet. At the beginning of implosion, the ablation pressure launches a shock wave that propagates ahead of the thermal ablation front and increases the fuel entropy. Then, as the first shock breaks out at the rear surface of the shell, the transmitted shock is formed. It converges through the vapor to the capsule center. After reflection from the center, the shock moves outward and interacts with the incoming shell. At this point, the velocity of the inner portion of the shell starts to decrease, reversing its sign at stagnation. This is a crucial point of the implosion since no more “pdV” compression work can be done to the hot spot after the stagnation, and the only remaining heating source is the energy deposition of α particles produced by fusion reactions inside the hot spot (α heating).

At the deceleration phase of the implosion, the kinetic energy of the shell is transferred into the internal energy of the hot spot. To ignite the fuel, the energy gain due to the pdV work of the imploding shell and α heating must be larger than the energy losses due to thermal conduction and radiation. This requirement sets a minimum value for the implosion velocity v_{imp} of the shell.

The following sections review the basic concept of ICF ignition, present the simplest direct-drive ignition target design, and discuss stability issues.

Basic Concepts

To burn a substantial fraction of the fuel mass, the fuel density at stagnation must be very large. This can be easily shown if we assume that the main fuel at the peak compression is assembled as a uniform-density sphere with a radius R_f and density ρ_m .^{1,2} The reaction rate is given by $dn/dt = n_D n_T \langle \sigma v \rangle$, where $\langle \sigma v \rangle$ is the average reactivity, n_D and n_T are the density of deuterium and tritium, respectively, and n is the number density of the reacted fuel. Assuming a 50/50 DT mixture, $n_D = n_T = n_0/2 - n$, where n_0 is the initial density. To calculate the total number of reactions, we integrate $N = \int_0^{t_d} V(t)(dn/dt)dt$ over the burn duration time t_d , where $V(t)$ is the volume of the burning fuel. The burn time is determined by the fuel disassembly rate. Since there is no external force to keep the fuel together after the stagnation, the outer region of the fuel expands, launching a rarefaction wave toward the center. The rarefaction wave propagates at the local sound speed c_s and it takes approximately $t_d = R_f/c_s$ for the whole sphere to decompress and cool down, quenching the fusion reactions. During the decompression, only the high-density portion of the fuel inside the radius $R(t) = R_f - c_s t$ is burning. Since the total number of reactions is proportional to the time integral of the burning fuel volume, we can define an effective confinement time t_c as $\int_0^{t_d} V(t)dt = V_0 t_c$, where $V_0 = 4\pi R_f^3/3$. The integration gives $t_c = t_d/4$. If the number of fused atoms is small, $n \ll n_0$, then the total number of reactions becomes $N = n_0^2 \langle \sigma v \rangle V_0 t_c / 4$. The ratio $f = N/N_0$ is commonly referred to as a burn fraction, where $N_0 = n_0 V_0 / 2$

is the initial number of DT pairs. Substituting N into f gives $f = n_0 R_f \langle \sigma v \rangle / 8 c_s = \rho_m R_f / (8 c_s m_{\text{DT}} \langle \sigma v \rangle)$, where m_{DT} is the DT ion mass. The combination $8 c_s m_{\text{DT}} \langle \sigma v \rangle$ has a minimum value of 6 g/cm^2 at the ignition conditions; to have an efficient burn, the fuel must reach $\rho_m R_f > 1 \text{ g/cm}^2$ at peak compression (more accurate calculations show that $f = 0.3$ at $\rho_m R_f = 3 \text{ g/cm}^2$). Using such an estimate, we can determine the maximum density of the assembled fuel and convergence ratio of the shell at ignition. Assuming that a fraction f_H of the laser energy E_L goes into the shell kinetic energy $M v_{\text{imp}}^2 / 2$, the shell mass M can be expressed as $M = 2 f_H E_L / v_{\text{imp}}^2$. The fraction f_H is a product of the hydrodynamic efficiency (defined as a ratio of the shell kinetic energy to the absorbed laser energy, typically $\sim 10\%$ for a direct-drive implosion) and the laser absorption fraction of ~ 0.6 . This yields $f_H \sim 0.06$. The fuel mass at stagnation can be rewritten as $M = 4\pi(\rho_m R_f)^3 / 3\rho^2$. Equating the two expressions for the mass, we obtain the fuel density at the peak compression

$$\rho_m = v_{\text{imp}} \sqrt{\frac{2\pi(\rho_m R_f)^3}{3f_H E_L}}. \quad (1)$$

The value of $\rho_m R_f \simeq 2 \text{ g/cm}^2$ is fixed by the fuel burnup fraction. The implosion velocity cannot be much less than $3 \times 10^7 \text{ cm/s}$ to have a temperature increase inside the hot spot during the shell deceleration (energy gain exceeds the energy losses at such a velocity). Using these values gives $\rho_m (\text{g/cm}^3) \simeq 160 / \sqrt{E_L (\text{MJ})}$, where the laser energy is measured in megajoules. For an $E_L = 1 \text{ MJ}$ facility, $\rho_m = 160 \text{ g/cm}^3 \simeq 630 \rho_{\text{DT}}$, where $\rho_{\text{DT}} = 0.25 \text{ g/cm}^3$ is the density of cryogenic uncompressed DT mixture at $T = 18 \text{ K}$. To find the shell convergence ratio $C_r = R_0 / R_f$ required to achieve such a high density, we write the mass conservation equation $4\pi\rho_{\text{DT}} R_0^3 (1 - f_A) / A_0 = 4\pi\rho_m R_f^3 / 3$, where $A_0 = R_0 / \Delta_0$ is the initial aspect ratio, R_0 and Δ_0 are the inner radius and thickness of the undriven shell, and f_A is the fraction of the shell mass ablated during the implosion. For a typical direct-drive ignition design, $f_A \simeq 0.8$. This leads to

$$C_r \simeq \left(\frac{5}{3} A_0 \frac{\rho_m}{\rho_{\text{DT}}} \right)^{1/3}. \quad (2)$$

Taking $A_0 = 4$ and $\rho_m / \rho_{\text{DT}} = 630$ gives $C_r = 16$.

So far, we considered only conditions for the high- ρR fuel assembly. To initiate the burn wave inside the main fuel, as mentioned earlier, the hot spot must first reach ignition con-

ditions. Since the reaction rate is proportional to p^2 ($dn/dt \sim n^2 \langle \sigma v \rangle$) and $\langle \sigma v \rangle \sim T^2$ for $T > 6 \text{ keV}$, this gives $dn/dt \sim p^2$, high pressure must be achieved inside the hot spot. We can estimate the pressure evolution inside the hot spot during the deceleration phase by considering an adiabatic compression of a gas by a spherical piston. The adiabatic condition relates the pressure and density as $p \sim \rho^{5/3}$. Then the mass conservation yields $\rho R^3 = \rho_d R_d^3$ or $\rho \sim R^{-3}$, where ρ_d and R_d are the mass density and radius at the beginning of deceleration. This gives

$$p = p_d \left(\frac{R_d}{R} \right)^5. \quad (3)$$

Strictly speaking, the hot-spot compression cannot be considered as adiabatic during the deceleration phase because of thermal conduction effects. A detailed calculation including thermal conduction losses,³ however, shows that an R^{-5} law is valid in a more general case (not including α deposition). This can be easily explained if we consider pressure as an internal energy density. The thermal conduction deposits part of the hot-spot energy into heating the inner layer of the surrounding cold shell. The heated layer then ablates and the ablated mass returns the lost energy back into the hot spot. With the help of Eq. (3), we can calculate the shell trajectory during the deceleration using Newton's law;

$$M \frac{d^2 R}{dt^2} = 4\pi p R^2. \quad (4)$$

Integrating the latter equation gives

$$v^2 = v_{\text{imp}}^2 + \frac{4\pi p_d R_d^3}{M} (1 - C_{rd}^2), \quad (5)$$

where $C_{rd} = R_d / R$. At stagnation, $v = 0$ and Eq. (5) yields the total convergence ratio

$$C_{rd} \sim \sqrt{1 + \frac{E_k}{E_i}}, \quad (6)$$

where $E_k = M v_{\text{imp}}^2 / 2$ and

$$E_i = \frac{4\pi}{3} \frac{p_d}{(\gamma - 1)} R_d^3 = 2\pi p_d R_d^3$$

is the shell kinetic energy and the total internal energy of the gas at the beginning of the deceleration phase, respectively, and γ is the ratio of specific heats [we used $\gamma = 5/3$ in Eq. (6)]. The relation (6) is satisfied only approximately since it does not take into account the pressure increase due to α deposition. Such an effect is important, however, only near stagnation. Using the limit $E_k \gg E_i$, the maximum pressure takes the form

$$p_m = \frac{1}{p_d^{3/2}} \left(\frac{E_k}{3V_d} \right)^{5/2}, \quad (7)$$

where $V_d = 4\pi R_d^3/3$. Equation (7) shows that to achieve the hot-spot ignition (high pressure) we must minimize, for a given kinetic energy, the gas pressure and radius R_d at the beginning of shell deceleration (when the reflected shock starts interacting with the shell). The next section will explain how such a minimization is achieved in a direct-drive ignition target.

Direct-Drive Ignition Target Design

High density and convergence ratio requirements put a limitation on the maximum entropy increase in the shell during an implosion. Let us assume that the pressure increases from its initial value p_0 inside the shell to the ablation pressure p_a at the maximum laser intensity. The density ρ is at its maximum when the shell entropy increase is zero ($\Delta s = 0$) during the compression (adiabatic implosion); $\rho/\rho_0 = (p_a/p_0)^{1/\gamma} e^{-\Delta s/c_p}$, where c_p is the specific heat at constant pressure and ρ_0 is the initial density. It is not feasible, however, to drive a perfectly adiabatic implosion. Shock waves, radiation preheat, hot-electron preheat, and others increase the entropy during the shell compression. We can minimize the hydrodynamic part in the entropy change, nevertheless, by accurately timing all hydrodynamic waves launched into the target during the laser drive. The shell entropy is commonly characterized by the adiabat $\alpha = p/p_F$, which is defined as the ratio of the shell pressure p to the Fermi-degenerate pressure (mainly because of electrons) p_F calculated at the shell density. The Fermi pressure of an electron gas has the form $p_F = \mu \rho^{5/3}$, where $\mu = (3\pi^2)^{2/3} \hbar^2 Z^{5/3} / 5m_i^{5/3} m$, m and m_i are electron and ion masses, respectively, \hbar is the Planck constant, and Z is the ion charge. For fully ionized DT, $\mu = 2.15 [\text{Mbar}/(\text{g}/\text{cm}^3)^{5/3}]$. Since the shell entropy during an implosion is a crucial parameter, the target design in ICF is characterized by the adiabat value. For example, an “ $\alpha = 3$ design” means that the pressure inside the shell during the implosion in such a design is three times larger than the Fermi-degenerate pressure of the fully ionized DT.

Next we consider the simplest direct-drive target design, which consists of a spherical DT-ice shell filled with DT gas. The main fuel in the shell is kept at cryogenic temperatures (~ 18 K) to maximize the fuel mass and minimize the shell entropy. The initial shell thickness is Δ_0 and the inner shell radius is $R_0 \gg \Delta_0$. The target is driven by a laser pulse that consists of three distinct regions: a low-intensity foot, a transition region, and the main drive [see Fig. 106.23(a)]. The main parameters of the laser pulse are the foot length t_0 , end of the rise time t_r , end of the pulse t_{end} , foot power P_0 , and maximum power P_{max} . During the foot, a shock wave (SW1) launched at the beginning of the pulse propagates through the shell. The adiabat of the post-shock material depends on the shock strength, which, in turn, is a function of the laser intensity. Thus, the foot power P_0 is chosen to set the post-shock material on a desired adiabat α . Analytical models^{1,4} predict that the drive pressure and the laser intensity I are related as $p(\text{Mbar}) = 40(I_{15}/\lambda_L)^{2/3}$, where I_{15} is measured in $10^{15} \text{ W}/\text{cm}^2$ and λ_L is the laser wavelength measured in

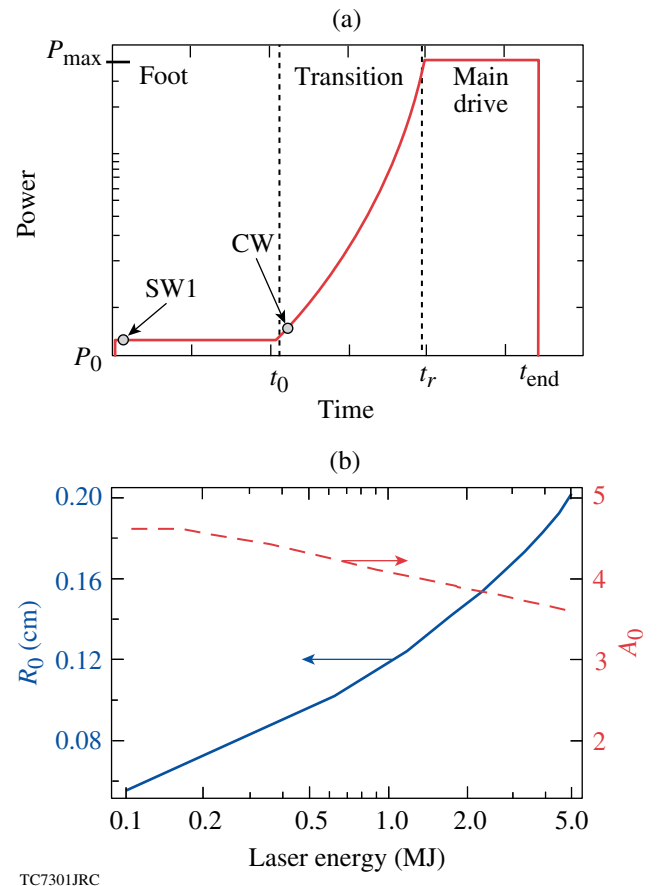


Figure 106.23

(a) Laser drive pulse for a direct-drive target. (b) The dimensions of direct-drive ignition targets versus laser energy ($v_{\text{imp}} = 4.5 \times 10^7 \text{ cm/s}$).

microns. Substituting $p = \alpha\mu\rho_1^{5/3}$ into the latter equation shows that the laser intensity scales with α in a DT shell driven by a $\lambda_L = 0.351 \mu\text{m}$ laser as $I_{12} = 4\alpha^{3/2}$, where the intensity is measured in TW/cm^2 and the post-shock density is $\rho_1 \simeq 4\rho_{\text{DT}} = 1 \text{ g}/\text{cm}^3$ in the strong-shock limit. The $3/2$ power law does not take into account an intensity dependence in the laser absorption. When the latter is included (with the help of numerical simulations), the required laser intensity becomes $I_{12} = 7\alpha^{5/4}$. Using this result, we obtain a relation between the foot power and the shell adiabat; $p_0(\text{TW}) = 90 R_0^2 (1 + 1/A_0)^2 \alpha^{5/4}$. Next, as the laser intensity increases during the transition time, a compression wave (CW) is launched into the shell. To prevent an adiabat increase, such a wave should not turn into a strong shock inside the shell. This determines the intensity slope in the transition region. To maintain an adiabatic compression during the rise time, one can use Kidder's solution⁵ for the drive pressure. This gives the power history during the transition time

$$P = \frac{\hat{P}}{\left[1 - (t/T_c)^2\right]^\omega}, \quad (8)$$

where T_c and \hat{P} are normalization coefficients determined from matching P with P_0 at $t = t_0$ and $P = P_{\text{max}}$ at $t = t_r$. Numerical simulations show that moderate variations in ω ($2 < \omega < 7$) do not significantly affect the shell adiabat. Since there are limitations on the maximum power imposed by both instabilities because of the laser-plasma interaction and damage threshold issues, the laser power cannot follow Eq. (8) at all times. Thus, we assume that the laser power becomes flat after time t_r when P reaches the peak power P_{max} [see Fig. 106.23(a)].

Next, we consider what determines the values of t_0 and t_r . The CW, as any linear sound wave in hydrodynamics, travels with the local sound speed and eventually catches up with the SW1. After coalescence, both the shock strength and the adiabat of the post-shock material increase. Minimizing the shell adiabat, we must prevent the CW and SW1 coalescence inside the shell. This sets the minimum value of t_0 . Conversely, if t_0 is too large, the SW1 and CW will be well separated in time. As the SW1 breaks out at the shell's rear surface, the surface starts to expand, launching a rarefaction wave (RW) toward the ablation front. The RW establishes some velocity, pressure, and density gradients in its tail. Since the CW and RW travel in opposite directions, they meet inside the shell. At this instant, the CW starts to propagate along the hydrodynamic gradients established by the RW. It is well known in hydrodynamics that a sound wave traveling along a decreasing density turns into a shock sooner than a sound wave traveling through a uniform or increasing density. As the CW turns into a shock,

the latter will excessively increase the shell entropy, reducing the shell convergence ratio. The foot duration t_0 can be related to the shell adiabat α and the initial shell thickness Δ_0 . Using Hugoniot jump conditions across the shock, one can easily obtain the shock velocity; neglecting spherical convergence effects, $U_s(p_1 \gg p_0) = \sqrt{(\gamma + 1)p_1/2\rho_0}$, where p_0 and p_1 are the initial and post-shock pressure, respectively. The SW1 transit time through the shell becomes $t_{\text{sh}} = \Delta_0/U_s$. The CW travels through the shock-compressed shell with a thickness $\Delta_c = \Delta_0\rho_0/\rho_1$, where ρ_0 and ρ_1 are the initial and post-shock density, respectively. The CW propagation time is $t_{\text{cw}} = \Delta_c/c_1$, where $c_1 = \sqrt{\gamma p_1/\rho_1}$. Thus, the foot length takes the form $t_0 = t_{\text{sh}} - t_{\text{cw}}$. Using expressions for the shock velocity and the adiabat yields the following equations for t_0 and t_{sh} :

$$t_0(\text{ns}) = 0.016 \frac{\Delta_0(\mu\text{m})}{\sqrt{\alpha}}$$

and

$$t_{\text{sh}}(\text{ns}) = 0.03 \frac{\Delta_0(\mu\text{m})}{\sqrt{\alpha}}, \quad (9)$$

where $\gamma = 5/3$. Similar to t_0 , the rise time t_r is also determined by avoiding an additional strong-shock formation. The transition region cannot be too short; the CW otherwise turns into a shock. The time t_r also cannot be too large. This is due to the formation of a second shock wave (SW2) inside the shell. It is easy to show that an adjustment wave (AW) is formed as the leading edge of the RW breaks out at the ablation front. Each fluid element inside the RW is accelerated according to $dv/dt = -\partial_x p/\rho$. At the head of the RW, ρ is equal to the shell density compressed by the SW1 and CW. When the leading edge reaches the ablation front, the density suddenly drops, creating a large gradient in the acceleration of fluid elements. This forms a local excess in the pressure that starts to propagate in the form of a compression (adjustment) wave along a decreasing density profile of the RW tail. As mentioned earlier, the AW traveling along a decreasing density turns into a shock inside the shell.⁶ Thus the SW2 is formed even for a constant-intensity laser pulse.

The formation of the AW can also be shown by comparing the following density profiles: In the first case, the profile is created by a rarefaction wave traveling across a uniform-density foil. For the second profile, we take a solution of the motion equation for an accelerated foil. The solution for a rarefaction wave profile can be found using a self-similar analysis.⁷ Calculated at the breakout time of the leading edge, the density becomes

$$\rho = \rho_{a1} \left(\frac{\bar{x} + d_1}{d_1} \right)^3, \quad (10)$$

where \bar{x} is the position in the frame of reference moving with the ablation front ($\bar{x} = 0$ at the ablation front), $\gamma = 5/3$, and d_1 is defined as $\rho(-d_1) = 0$. Conversely, during the shell acceleration, the density profile can be found by solving Newton's equation

$$\rho g = \frac{\partial p}{\partial x}. \quad (11)$$

Assuming that the entropy is uniform across the entire shell, the pressure is related to the density as $p = \mu\alpha\rho^{5/3}$, and the solution of Eq. (11) takes the form

$$p = p_a \left(1 + \frac{\bar{x}}{d_2} \right)^{5/2}, \quad (12)$$

where $d_2 = 5\mu^{3/5}\alpha^{3/5}p_a^{2/5}/2g$. Then, the adiabatic relation $\rho = (p/\mu\alpha)^{3/5}$ gives

$$\rho = \rho_{a2} \left(\frac{\bar{x} + d_2}{d_2} \right)^{3/2}. \quad (13)$$

The comparison of Eqs. (10) and (13), keeping the same mass for the two profiles, gives the relation between the shell thicknesses

$$d_2 = \frac{5}{8} \left(\frac{p_{a1}}{p_{a2}} \right)^{3/5} d_1. \quad (14)$$

Since $p_{a1} \leq p_{a2}$ (the shell is accelerated during the main pulse where the intensity reaches the maximum value), we conclude that the shell during the acceleration should be more compact than that produced by a rarefaction wave; $d_2 < d_1$. This is possible only if a compression wave is launched into the shell at the beginning of the acceleration.

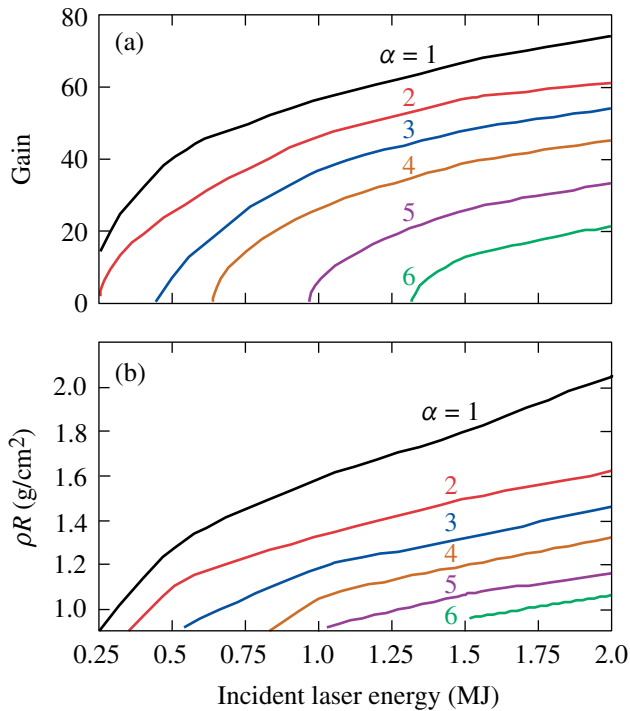
Even though the SW2 cannot be avoided, its strength and effect on target performance can be minimized by appropriately choosing t_r . An intensity rise prior to the leading edge of the RW breakout at the ablation front helps to steepen the density profile, reducing the AW strength. If t_r is too large and the SW2 formation occurs during the drive-pressure rise, the SW2 will be too strong, raising the pressure in the vapor. Thus, t_r must be between the SW1 breakout at the rear surface and the leading edge of the RW breakout at the ablation front (in other

words, the laser must reach the peak power while the leading edge of RW is inside the shell). This concludes the pulse-shape specification for a simple direct-drive ignition design.

Next, we determine the optimum target radius R_0 and shell thickness Δ_0 for a given laser energy. The following effects must be considered: After the SW1 breaks out at the back of the shell, a transmitted shock is formed in the vapor. This shock reaches the center, reflects, and eventually interacts with the incoming shell. During the reflected-shock propagation through the shell, the shell decelerates (deceleration phase of an implosion). If R_0 is too large, the laser is turned off well before the beginning of the deceleration phase. The shell then coasts inward between the end of the drive pulse and beginning of deceleration. Both the front and back surfaces of the shell expand, in the frame of reference moving with the main fuel, during the coasting phase, reducing the shell density. To maximize the density, the duration of the coasting phase must be minimized. This sets an upper limit on R_0 . In the opposite case, when R_0 is too small, the reflected shock interacts with the shell while the laser pulse is still on. The pressure inside the shell in this case increases above the drive-pressure value and the shell acceleration therefore goes to zero, preventing an effective transfer of the laser absorbed energy into the kinetic energy of the shell. Thus, the end of the pulse in an optimized design should occur after the main shock reflection from the target center, but before the beginning of the deceleration phase.

Accounting for the optimization arguments listed earlier, we plot the shell radius and initial aspect ratio $A_0 = R_0/\Delta_0$ versus the incident laser energy in Fig. 106.23(b), keeping the maximum laser intensity at $I_{\max} = 10^{15}$ W/cm² and the implosion velocity at $v_{\text{imp}} = 4.5 \times 10^7$ cm/s. Calculations show that the target dimensions do not have a strong dependence on the shell adiabat. The shell radius is fitted well with a 1/3-power law $R_0 = 0.06[E_L(\text{MJ})/0.1]^{1/3}$. The shell thickness, on the other hand, has a stronger energy dependence; $\Delta_0 = 0.012[E_L(\text{MJ})/0.1]^{1/2.6}$. A deviation from the $E_L^{1/3}$ scaling in Δ_0 (which is expected from a simple $E_L \sim D^3$ argument, where D is a scale length of the problem) is due to a scale-length dependence in the laser absorption (the smaller the target, the steeper the density scale length, and, therefore, the smaller absorption fraction). This results in an increased initial aspect ratio for the lower laser energies, as shown in Fig. 106.23(b).

Using the obtained target dimensions and laser pulse shapes, the gain curves and the maximum shell ρR can be calculated with a one-dimensional hydrocode. These are shown in Fig. 106.24. Figure 106.24(a) indicates that the designs with the



TC7302JRC

Figure 106.24

 (a) Gain curves and (b) maximum ρR for ignition direct-drive targets.

shell adiabat up to $\alpha = 6$ are expected to ignite on the National Ignition Facility with the incident laser energy $E_L = 1.5$ MJ.

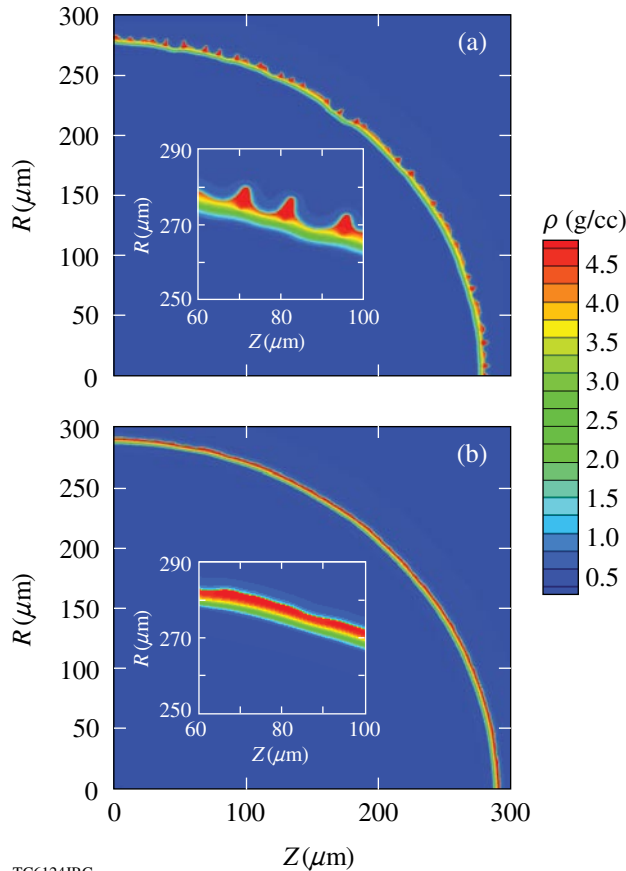
Stability

Hydrodynamic instabilities put severe constraints on target designs because they limit the maximum convergence ratio and temperature of the hot spot.^{1,8} The dominant hydrodynamic instability in an ICF implosion is the Rayleigh–Taylor (RT) instability. The RT instability inevitably occurs in systems where the heavier fluid is accelerated by the lighter fluid.⁹ Such conditions arise during the shell compression in ICF implosions where the heavier shell material is accelerated by the lighter blowoff plasma. The RT instability growth amplifies the shell distortions seeded by initial surface roughness and laser nonuniformities (laser “imprint”). If allowed to grow to substantial amplitudes, the shell nonuniformities reduce the shell ρR and the neutron yield. Fortunately for ICF implosions, the thermal conduction that drives the ablation process creates several stabilizing effects that reduce both the nonuniformity seeding and the RT growth rates.^{10,11} Seeding due to the laser nonuniformity is determined by how quickly the plasma atmosphere is created around the imploding shell. The laser irradiation is absorbed at some distance from the cold shell. The larger this distance (the conduction zone), the larger the smoothing effect

of the thermal conductivity within the conduction zone and the smaller the laser imprint. The RT modes are also stabilized by the thermal conductivity that drives the mass ablation of the shell material. The ablation process is characterized by the ablation velocity V_a , which is defined as the ratio of the mass ablation rate to the shell density $V_a = \dot{m}/\rho_{sh}$. The larger the value of the ablation velocity, the larger the ablative stabilization. Taking thermal smoothing and ablative stabilization into account, one can make a general statement that the higher the initial intensity of the drive laser pulse (larger P_0), the smaller the nonuniformities and the more stable the implosion. Indeed, the higher intensity tends to create the conduction zone in a shorter time, reducing the laser imprint. In addition, the initial shock launched by the higher-intensity pulse is stronger, resulting in higher shell adiabat. This reduces the shell density, increasing the ablation velocity. Furthermore, a lower density leads to an increase in the shell thickness and a reduction in the perturbation feedthrough from the ablation front to the shell’s rear surface (which becomes unstable during the deceleration phase of the implosion). There is a price to pay, however, for the greater stability. As the stronger shock propagates through the shell, it places the shell material on a higher adiabat. This leads to a reduction in target gain and shell ρR , as shown in Fig. 106.24. A common practice in designing direct-drive targets is to find the delicate balance between a reduction in the target performance due to an increase in the adiabat and the increase in shell stability.

In optimizing the target design, one can take into consideration that the RT modes are surface modes peaked at the ablation surface of the shell. To reduce the instability growth, it is therefore sufficient to raise the adiabat only at the outer region of the shell, which ablates during the implosion. If the inner portion of the shell is kept on a lower adiabat, the shell and vapor compressibility will not be reduced during the final stage of implosion and the neutron yields will be unaffected by this selective adiabat increase (adiabat shaping). The shell adiabat is shaped by launching a shock, whose strength decreases as it propagates through the shell.¹² This places an adiabat gradient directed toward the ablation front. A time variation in the shock strength is imposed by replacing the foot with an intensity picket in front of the main-drive pulse. The picket launches a strong shock that propagates through the shell. As the laser intensity drops at the end of the picket, the shocked material starts to expand and a rarefaction wave is launched toward the shock. After the rarefaction and the shock coalesce, the shock strength decays, reducing the adiabat of the shock-compressed material. Implementing the adiabat shaping to the direct-drive ignition target designs shows a significant improvement in shell

stability without compromising the target gain. This is illustrated in Fig. 106.25, where two target designs with (a) a foot and (b) an intensity picket in front of the main drive are shown at the end of the acceleration phase. The isodensity contours are obtained using the two-dimensional hydrocode *ORCHID*.¹³ An improvement in the shell stability increases our confidence in the success of the direct-drive ignition campaign on NIF.



TC6124JRC

Figure 106.25
Isodensity contours of the (a) standard and (b) picket OMEGA $\alpha = 3$ target designs.

ACKNOWLEDGMENT

This work was supported by the U.S. Department of Energy Office of Inertial Confinement Fusion under Cooperative Agreement No. DE-FC52-92SF19460, the University of Rochester, and the New York State Energy Research and Development Authority. The support of DOE does not constitute an endorsement by DOE of the views expressed in this article.

REFERENCES

1. J. D. Lindl, *Inertial Confinement Fusion: The Quest for Ignition and Energy Gain Using Indirect Drive* (Springer-Verlag, New York, 1998).
2. M. D. Rosen, *Phys. Plasmas* **6**, 1690 (1999).
3. R. Betti, K. Anderson, V. N. Goncharov, R. L. McCrory, D. D. Meyerhofer, S. Skupsky, and R. P. J. Town, *Phys. Plasmas* **9**, 2277 (2002).
4. W. M. Manheimer, D. G. Colombant, and J. H. Gardner, *Phys. Fluids* **25**, 1644 (1982).
5. R. E. Kidder, *Nucl. Fusion* **14**, 53 (1974).
6. R. Betti, V. Lobatchev, and R. L. McCrory, *Phys. Rev. Lett.* **81**, 5560 (1998).
7. L. D. Landau and E. M. Lifshitz, *Fluid Mechanics*, 2nd ed., Course of Theoretical Physics, Vol. 6 (Butterworth-Heinemann, Newton, MA, 1987).
8. S. Atzeni and J. Meyer-ter-Vehn, *The Physics of Inertial Fusion: Beam Plasma Interaction, Hydrodynamics, Hot Dense Matter*, International Series of Monographs on Physics (Clarendon Press, Oxford, 2004).
9. S. Chandrasekhar, in *Hydrodynamic and Hydromagnetic Stability*, International Series of Monographs on Physics (Clarendon Press, Oxford, 1961).
10. J. Sanz, *Phys. Rev. Lett.* **73**, 2700 (1994).
11. V. N. Goncharov, R. Betti, R. L. McCrory, P. Sorotokin, and C. P. Verdon, *Phys. Plasmas* **3**, 1402 (1996).
12. V. N. Goncharov, J. P. Knauer, P. W. McKenty, P. B. Radha, T. C. Sangster, S. Skupsky, R. Betti, R. L. McCrory, and D. D. Meyerhofer, *Phys. Plasmas* **10**, 1906 (2003).
13. R. L. McCrory and C. P. Verdon, in *Computer Applications in Plasma Science and Engineering*, edited by A. T. Drobot (Springer-Verlag, New York, 1991).

Tests of the Hydrodynamic Equivalence of Direct-Drive Implosions with Different D₂ and ³He Mixtures

Introduction

Ignition and high gain in inertial confinement fusion (ICF)^{1–3} requires an understanding of how the choice of materials affects implosion dynamics. ICF ignition targets are typically spherical capsules with an outer shell made of plastic or beryllium, a cryogenic layer of deuterium–tritium (DT) ice, and gaseous DT at the center. The direct-drive approach to ICF⁴ implodes the target by direct illumination using multiple laser beams. Laser ablation of the capsule’s outer surface drives the remaining payload inward, compressing and heating it to a state where nuclear fusion can occur.

Surrogate materials or configurations provide a convenient test bed to study different aspects of ignition designs.^{5,6} These surrogates are chosen to best mimic the implosion characteristics of the original design. For example, although ignition designs use an equal mole DT mixture, pure D₂ is commonly used as a surrogate. The different mass densities, however, can cause a difference in implosion dynamics (in particular through the Atwood number, which differs by a factor of 2 at the fuel–shell interface during the deceleration phase⁷).

To explore the effects of fill composition on the implosion dynamics of surrogate fuels, a series of experiments using different ratios of D₂ and ³He was performed. Evaluation of surrogate materials is best done when the materials are chosen to be as nearly hydrodynamically equivalent as possible. D and ³He have a special property in which they have the same value of $(1 + Z)/A$, allowing mixtures of D₂ and ³He to be chosen such that the mass density and the total particle density upon full ionization are identical. This results in the same Atwood number (affecting hydrodynamic instabilities^{2,7}) and the same equation of state (EOS).

An additional advantage of these surrogate targets is that products from the D–D nuclear reaction can be measured for all mixtures, whereas measuring the D–D products from a DT implosion has proven difficult for ignition-relevant implosions because of the large background of D–T neutrons. A final advantage of D₂ and ³He mixtures is their emission of D–³He protons

that have been extensively used to diagnose ICF implosions on OMEGA.^{8–10} **Experimental Setup** (p. 90) is a description of the setup and diagnostics used in the experiments. **Expected Scaling** (p. 92) describes the yield scaling expected of hydrodynamically equivalent implosions. **Experimental Observations** (p. 93) describes the results observed in the experiments as well as comparisons to the expected scaling and 1-D radiation-hydrodynamic simulations. The **Discussion** (p. 97) details possible explanations, and a **Summary** is given on p. 99.

Experimental Setup

Direct-drive implosions were conducted on OMEGA,¹¹ with 60 beams of frequency-tripled (351-nm) UV light in a 1-ns square pulse and a total energy of 23 kJ. SG4 phase plates¹² and 2-D, 1-THz bandwidth smoothing by spectral dispersion of the laser beam were used;¹³ the beam-to-beam energy imbalance was typically between 2% and 4% rms. The spherical targets were CH-shell capsules with diameters between 860 μm and 880 μm; a wall thickness of 15, 20, 24, or 27 μm; and a flash coating of about 0.1-μm aluminum.

The gaseous fill of the capsules was composed of mixtures of D₂ and ³He such that the atomic composition varied from pure D to nearly pure ³He. Two classes of fill pressure were used, low (equivalent to 3-atm D₂) and high (equivalent to 15-atm D₂), with predicted convergence ratios of 37 and 14, respectively. The mixtures within each class are considered hydrodynamically equivalent in that they have the same mass density (and therefore the same Atwood number during the deceleration phase) and, upon full ionization (above a few electron volts), the same total particle density and EOS (ideal monatomic).

Capsule fills are hydrodynamically equivalent if the fill pressures of D₂ (X atm) and ³He (W atm) are chosen to obey

$$X = \frac{3}{4}W = X_0, \quad (1)$$

where X_0 is the hydrodynamically equivalent pure-D₂ fill pressure, which is equal to either 3 atm or 15 atm in this article. The deuterium ion fraction by atom f_D scales with X and X_0 as

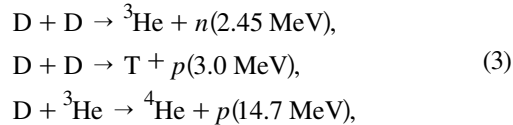
$$f_D = \frac{3X}{X + 2X_0}. \quad (2)$$

Since there are only two components to the fill gas, $f_{\text{He}} = 1 - f_D$.

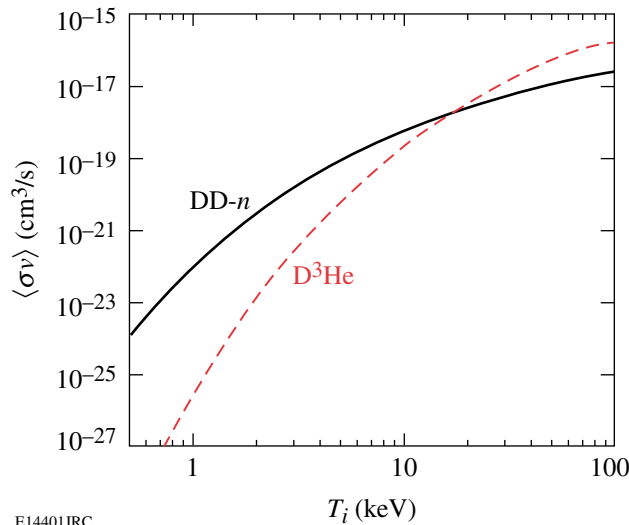
Two standard gas mixtures were used to fill targets of all types: pure D_2 ($f_D = 1.0$) and a D_2 - ${}^3\text{He}$ mixture with a 1:1 atomic ratio ($f_D = 0.5$). A series of shots with different mixtures of D_2 and ${}^3\text{He}$ was undertaken for the 20- and 24- μm -thick, high-pressure capsules. In addition to the premixed $f_D = 1.0$ and 0.5 compositions, compositions with $f_D = 0.07, 0.27,$ and 0.78 were used.¹⁴

The error in the fill composition for the “standard” ($f_D = 0.5$) D_2 - ${}^3\text{He}$ mixture is about 1% of f_D , since it comes premixed. Fill composition errors for the other composition ratios, which must be mixed to order, are also small—less than 3% (Ref. 15) of f_D . This error estimate includes uncertainties in the original fill pressure as well as uncertainties in the leak rates of D_2 and ${}^3\text{He}$ through the storage cell and through the target shell as it is handled before shot time. The total fill pressure is known to better than 10% and is independent of the fill composition.¹⁵

The following primary nuclear reactions occur in implosions of targets filled with mixtures of D_2 and ${}^3\text{He}$:



where the number in parentheses is the mean birth energy of the second product. Figure 106.26 shows the temperature dependence of the thermal reactivities of the DD - n and $D^3\text{He}$ reactions.



E14401JRC

Figure 106.26
 DD - n and $D^3\text{He}$ thermal reactivities as a function of ion temperature.

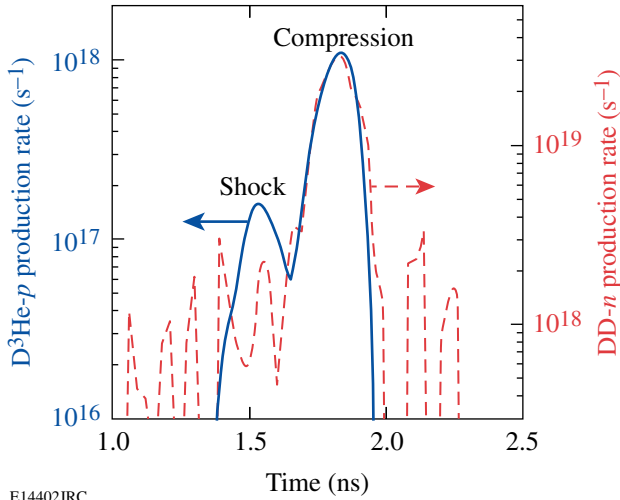
dence of the thermal reactivities of the D - ${}^3\text{He}$ reaction and the n branch of the D - D reaction, as determined by Bosch and Hale.¹⁶ The branching probability of the n and p branches of the D - D reaction are nearly equal over the temperatures of interest.

The principle diagnostics for this work were neutron time-of-flight (nTOF) scintillators¹⁷ to measure the neutron branch of the D - D reaction and multiple wedged-range-filter (WRF) proton spectrometers⁸ to measure the protons from the D - ${}^3\text{He}$ reaction. The nTOF detectors measure neutron yield and DD burn-averaged ion temperature determined from the Doppler broadening of the neutron signal.

The WRF spectrometers measure the $D^3\text{He}$ proton spectrum with high resolution (~ 100 keV). Transient magnetic fields¹⁸ in the implosion corona can redistribute the initially isotropic proton flux emitted by the capsule by 20% rms (typical).⁸ The average of the multiple (2 to 7) spectrometers is used to obtain an estimate of the total yield. The mean downshift of the $D^3\text{He}$ protons from their birth energy of 14.7 MeV is used to infer the areal density (ρR) of the imploded capsule averaged over the $D^3\text{He}$ proton production.⁸

An alternative measurement of the burn-averaged ion temperature is given by the “ratio method.”¹⁹ The ratio of primary yields can be used to infer the ion temperature using the thermal reactivities (Fig. 106.26) and the fuel composition. The ratio of DD - n to $D^3\text{He}$ reactivities changes by more than three decades from 1 keV to 10 keV, giving a determination of temperature that is not highly sensitive to the exact yields. Differences in burn duration or burn volume of the two constituent reactions result in only minor corrections to the inferred temperature (for example, see the very similar burn histories for DD - n and $D^3\text{He}$ compression in Fig. 106.27). This correction is small mainly because both reactions are dominated by the high-temperature region near the center.

Temporal diagnostics of the nuclear products include the neutron temporal diagnostic (NTD)²⁰ for measuring the DD - n burn history and the proton temporal diagnostic (PTD) for measuring the $D^3\text{He}$ burn history.^{21,9} The $D^3\text{He}$ burn history typically exhibits two periods of proton emission:²² The first is the “shock burn,” which occurs after the first convergence of the shock, near the end of the coasting phase, and before the capsule has fully compressed. About 300 ps later is the “compression burn” (see Fig. 106.27), which occurs during the deceleration and stagnation phases. Spectral measurements of the emitted $D^3\text{He}$ protons from such capsules can often be decomposed into such “shock” and “compression” components because of the different areal densities they pass through while escaping the capsule (~ 10 mg/cm²



E14402JRC

Figure 106.27 Measured D-³He proton (solid) and DD-*n* (dashed) nuclear production histories of a 24- μ m-thick CH shell filled with 6 atm of D₂ and 12 atm of ³He (shot 38525). Distinct shock and compression components are seen in the D-³He production history, whereas there is no evidence of neutrons at shock time in the DD-*n* production history. The noise level in the burn histories is about 10¹⁸/s for DD-*n* and less than 10¹⁶/s for D³He.

at shock and ~ 60 mg/cm² during compression). Because of the much weaker temperature dependence of the DD-*n* reactivity, the contribution of the high-temperature, low-density shock burn phase to the total yield is much lower than for D³He (typically 0.5% to 1% rather than 5% to 20%).

One-dimensional radiation-hydrodynamic simulations of these implosions were done using the code *LILAC*²³ with a flux limiter of 0.06. Composition scaling simulations were run by changing the initial fill composition while using the same target and laser conditions. To obtain yields of both reactions using compositions of $f_D = 0.0$ and 1.0, the results of those simulations were post-processed as having a trace of the minority species.

Expected Scaling

The nuclear yield is the spatial and temporal integral of the product of reactant densities times the temperature-dependent thermal reactivity of the nuclear reaction under consideration;

$$Y_n = \int \frac{1}{2} n_D^2(\vec{r}, t) \langle \sigma v \rangle_{DD-n} d^3 \vec{r} dt, \quad (4)$$

$$Y_p = \int n_D(\vec{r}, t) n_{^3\text{He}}(\vec{r}, t) \langle \sigma v \rangle_{D^3\text{He}} d^3 \vec{r} dt,$$

where Y_n and Y_p are the D-D neutron and D-³He proton yields, n_D and $n_{^3\text{He}}$ are the number densities of D and ³He, and $\langle \sigma v \rangle$

is the local thermal reactivity averaged over a Maxwellian ion velocity distribution with temperature T_i . The particle densities and ion temperature will, in general, be functions of position and time. The factor of 0.5 in the DD-*n* yield accounts for the double-counting of identical reactants.

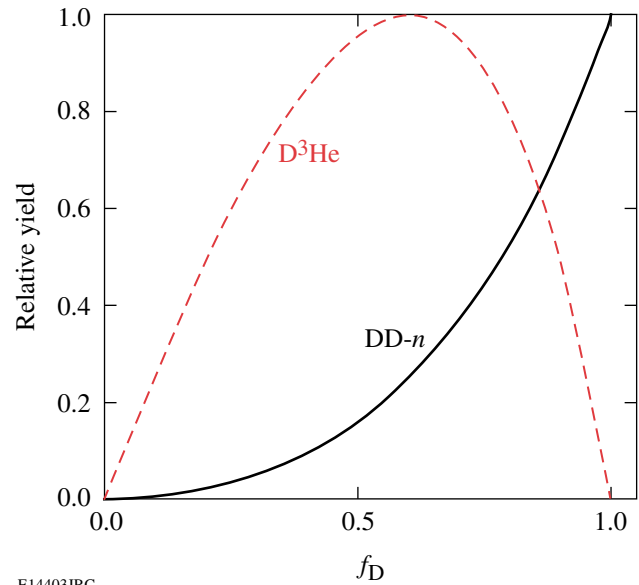
For the hydrodynamically equivalent mixtures of D₂ and ³He considered here and using the relation $n_i = \rho / A m_p = \rho / (3 - f_D) m_p$, the yields can be re-expressed in terms of f_D ;

$$Y_n = \frac{f_D^2}{(3 - f_D)^2} \int \frac{\rho^2(\vec{r}, t)}{2 m_p^2} \langle \sigma v \rangle_{DD-n} d^3 \vec{r} dt, \quad (5)$$

$$Y_p = \frac{f_D(1 - f_D)}{(3 - f_D)^2} \int \frac{\rho^2(\vec{r}, t)}{m_p^2} \langle \sigma v \rangle_{D^3\text{He}} d^3 \vec{r} dt,$$

where m_p is the proton mass and ρ is the mass density. The factor $(3 - f_D)^2$ is equal to A^2 and adjusts for the slightly different ion number densities of D₂ and ³He plasmas at equal mass density. The advantage of this form is that the dependence on the fill composition that determines the difference between hydrodynamically equivalent targets is taken out of the integral.

Figure 106.28 shows the predicted scaling of the D-D neutron and D-³He proton yields as a function of fill composition for hydrodynamically equivalent fuels. Although the character of the composition scaling is very different for the different nuclear



E14403JRC

Figure 106.28 Yield dependence of the DD-*n* and D³He reactions on the D fraction by atom (f_D).

reactions, both curves are independent of the implosion dynamics, so the composition contribution to the yield can be factored out.

All subsequent yields in this article will be scaled according to Eq. (6) unless otherwise noted;

$$\tilde{Y}_n = Y_n \frac{(3 - f_D)^2}{f_D^2}, \quad (6)$$

$$\tilde{Y}_p = Y_p \frac{(3 - f_D)^2}{f_D(1 - f_D)},$$

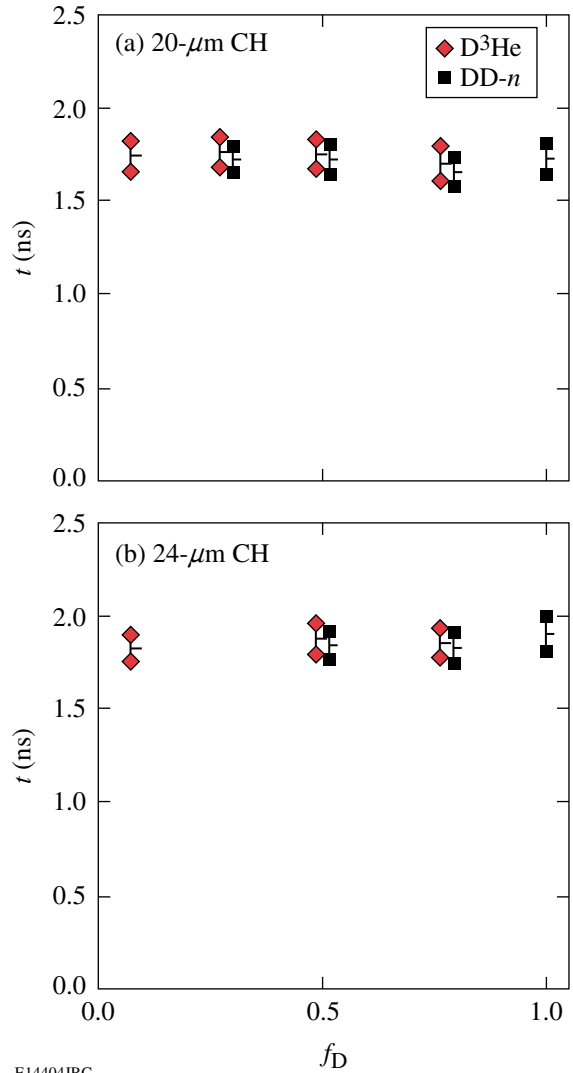
where \tilde{Y}_n and \tilde{Y}_p denote the scaled DD-*n* and D³He yields, respectively.

Experimental Observations

The hydrodynamic equivalence of D₂ and ³He mixtures is most clearly demonstrated by measurements of implosion timing. The time of peak neutron emission (DD-*n* bang time) as well as the duration of the neutron emission (characterized by the full width at half maximum as measured by the NTD) are independent of f_D . In addition, the time of peak proton emission during the compression phase (D³He compression bang time) and the duration of proton emission (characterized by the FWHM of the compression peak as measured by PTD) are also independent of f_D . Figure 106.29 plots the bang time and burn duration of both nuclear products as a function of f_D for both 20- and 24- μm -thick CH shells. Bang times and burn durations of the two nuclear products are also in good agreement with each other, an example of which can be seen fully in Fig. 106.27.

The measured yield of these hydrodynamically equivalent implosions deviates from the anticipated scaling shown in Fig. 106.28. The deviation of the scaled DD-*n* and D³He compression yields (\tilde{Y}_n and $\tilde{Y}_p - c$) for 20- and 24- μm CH shells with high-pressure fills is shown in Fig. 106.30. The yields have been scaled to the fill composition according to Eq. (6) and, in addition, have been normalized to the yield at $f_D = 0.5$ to emphasize the composition scaling for different measurements. Yields from targets with D-rich and ³He-rich fuels are typically twice as high as yields from targets with $f_D = 0.5$. This trend is seen for both DD-*n* and D³He yields and for both 20- and 24- μm shells.²⁴

This observed deviation is not seen in 1-D simulations (dashed line in Fig. 106.30), which instead more nearly follows the hydrodynamically equivalent scaling with only minor deviations. Table 106.VIII shows the absolute yields of the normalization points at $f_D = 0.5$ as observed experimentally



E14404JRC

Figure 106.29

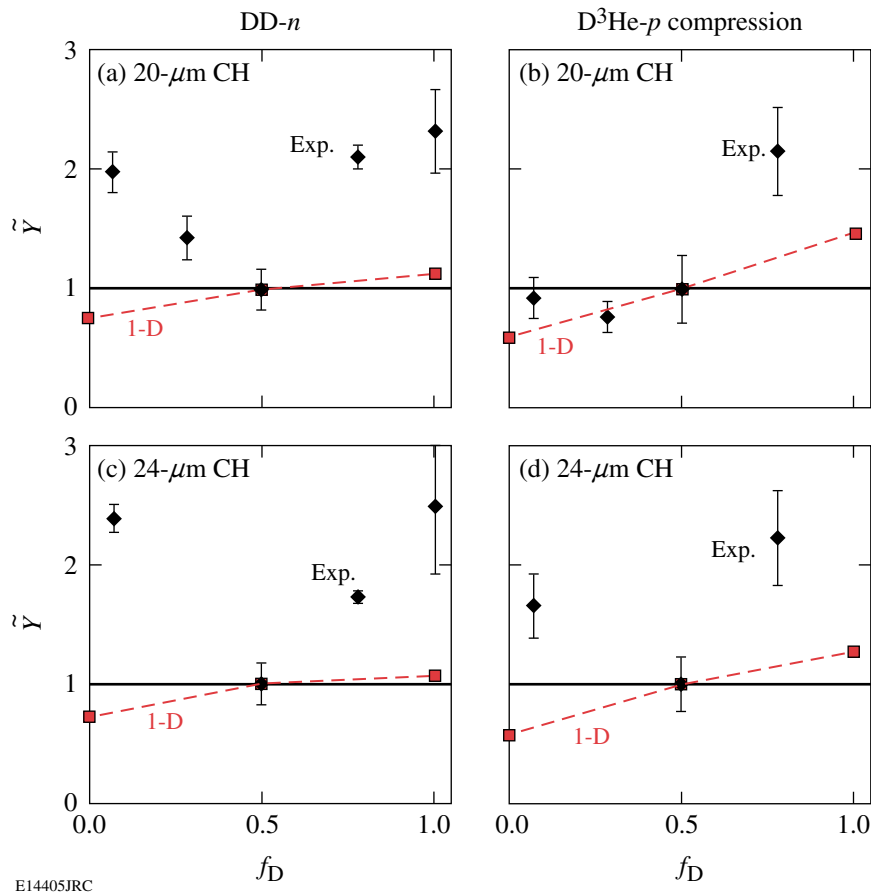
Nuclear bang time and burn duration as a function of fill composition for implosions with (a) 20 μm and (b) 24 μm of CH. Open diamonds and solid squares are the times of the half maximum of the peak emission of the D-³He protons and DD-neutrons, respectively.

and as calculated by *LILAC* as well as the absolute DD-*n* yield at $f_D = 1.0$. The DD-*n* experimental yield over calculated yield (YOC) is 21% for $f_D = 0.5$ and 42% or 48% for $f_D = 1.0$.

A comparison of the YOC for DD-*n* and D³He on shots with $f_D = 0.5$ illustrates the utility of simultaneous measurement of two nuclear reactions. As shown in Table 106.VIII, the D³He compression YOC is about 35% compared to the DD-*n* YOC of 21%. The difference in the YOC's for the two nuclear reactions is due to their probing the deviation between the simulated and actual implosion in different ways as a result of their different temperature sensitivities.

Table 106.VIII: Absolute (unscaled) compression yields of DD-*n* for $f_D = 1.0$ and 0.5 shots and D^3He for $f_D = 0.5$ shots as observed experimentally and as calculated by *LILAC*. The experimental yield over calculated yield (YOC) is also shown.

Shell	Type	$f_D = 1.0$	$f_D = 0.5$	
		$Y_n (\times 10^{10})$	$Y_n (\times 10^{10})$	$Y_{p-c} (\times 10^8)$
20- μm CH	Observed	18.7	1.29	6.28
20- μm CH	Calculated	44.6	6.29	18.4
20- μm CH	YOC	42.0%	20.5%	34.1%
24- μm CH	Observed	9.0	0.58	1.46
24- μm CH	Calculated	18.7	2.80	4.22
24- μm CH	YOC	48.1%	20.7%	34.6%



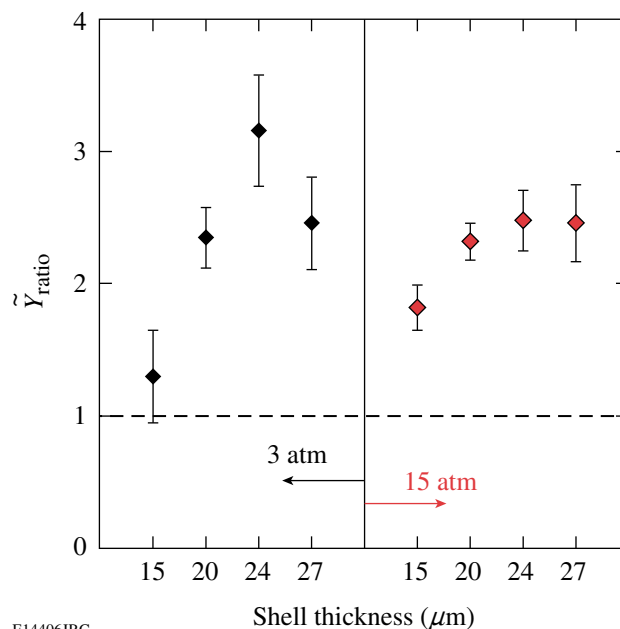
E14405JRC

Figure 106.30

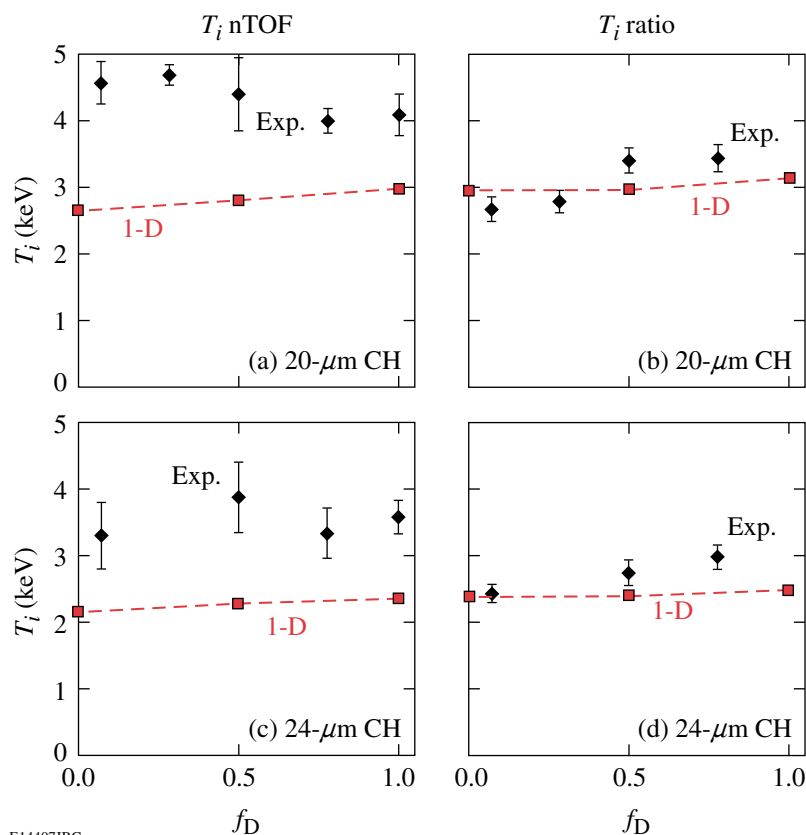
Scaled DD-*n* and D^3He compression yields for high-pressure ($X_0 = 15$ atm) fills of shells with 20 and 24 μm of CH. (a) \tilde{Y}_n , 20 μm ; (b) \tilde{Y}_{p-c} , 20 μm ; (c) \tilde{Y}_n , 24 μm ; (d) \tilde{Y}_{p-c} , 24 μm . All yields have been scaled to fill composition according to Eq. (6) and normalized to the yields at $f_D = 0.5$. True hydrodynamically equivalent implosions would scale to the same yield (solid line). 1-D simulations with *LILAC* (open squares, dashed line) deviate slightly from hydrodynamic equivalence but not nearly as much as experimental measurements (solid diamonds). The diamonds are the average yield and standard deviation from similar capsules. The 20- μm plots show data reduced from a total of 42 shots, and the 24- μm plots show data reduced from a total of 24 shots.

The “factor of 2” deviation of the yield scaling seen in these 20- and 24- μm CH shell, high-pressure composition campaigns has also been seen over a diverse set of target configurations. Targets with 15-, 20-, 24-, and 27- μm -thick CH shells and with both high and low fill pressures were filled with the two standard compositions; $f_D = 1.0$ and 0.5. Implosions of targets with both composition types emit DD-neutrons, and therefore a comparison of \tilde{Y}_n for like implosions with different compositions was done. Figure 106.31 shows the ratio of scaled yields $\tilde{Y}_n(f_D = 1.0)/\tilde{Y}_n(f_D = 0.5)$ for these implosions. The points at 15 atm and at 20 and 24 μm are the same as the points at $f_D = 1.0$ in Figs. 106.30(a) and 106.30(c). Data reduced from 118 shots predominantly gives a ratio greater than two where a ratio of 1 is anticipated for all capsule types.

The observed ion temperatures are not sufficient to explain the observed yield deviation. The mean ion temperature was measured using two methods: nTOF Doppler broadening and the yield ratio method. The nTOF does not show a trend in the ion temperature, whereas the ion temperature from the ratio method suggests increasing temperatures for higher D content fuels (see Fig. 106.32). Post-processing of 1-D LILAC simulations gives burn-averaged temperatures that are not strongly dependent on fill composition. Areal density measurements



E14406JRC
Figure 106.31
The ratio of measured \tilde{Y}_n for $f_D = 1.0$ shots over \tilde{Y}_n for $f_D = 0.5$ shots. The ratio anticipated by the scaling in Fig. 106.28 is 1 (horizontal dashed line) for all target parameters. The points are the ratio of scaled average yields, and the errors are the quadrature sum of the standard deviations of the mean of the two fill compositions. The plot shows data reduced from 118 shots.



E14407JRC
Figure 106.32
Ion temperature as a function of fill composition, as determined by the nTOF for high-pressure fills of (a) 20- μm and (c) 24- μm shells and using the ratio method for (b) 20 μm and (d) 24 μm . The diamonds are the average and standard deviation of experimental observations. The squares and dashed lines are 1-D LILAC.

using the downshift of primary D^3He protons (D^3He fuels) or secondary D^3He protons (pure D_2 fuel) show a lower value at compression time for $f_D = 0.5$ (for $24\text{-}\mu\text{m}$ shells, Fig. 106.33), suggesting slightly less compression for those shots.

A similar deviation from the anticipated scaling is also seen for the D^3He shock yield (\tilde{Y}_{p-s}), which is emitted about 300 ps earlier than the compression yield and is produced under very different conditions before the start of the deceleration phase and the onset of turbulent mixing²² at temperatures twice as high as

that at compression time and at mass densities less than 10% of those at compression time. Figure 106.34 shows the scaled D^3He shock yield and the shock-yield-averaged ρR for implosions with $24\text{-}\mu\text{m}$ CH shells. The results at shock time are reminiscent of the results at compression time with a lower scaled yield and ρR for the $f_D = 0.5$ shots than for D-rich or 3He -rich mixtures.

A summary of results from figures in this section is listed in Table 106.IX for different mixtures of high-pressure fills in shells with 20 and $24\text{ }\mu\text{m}$ of CH.

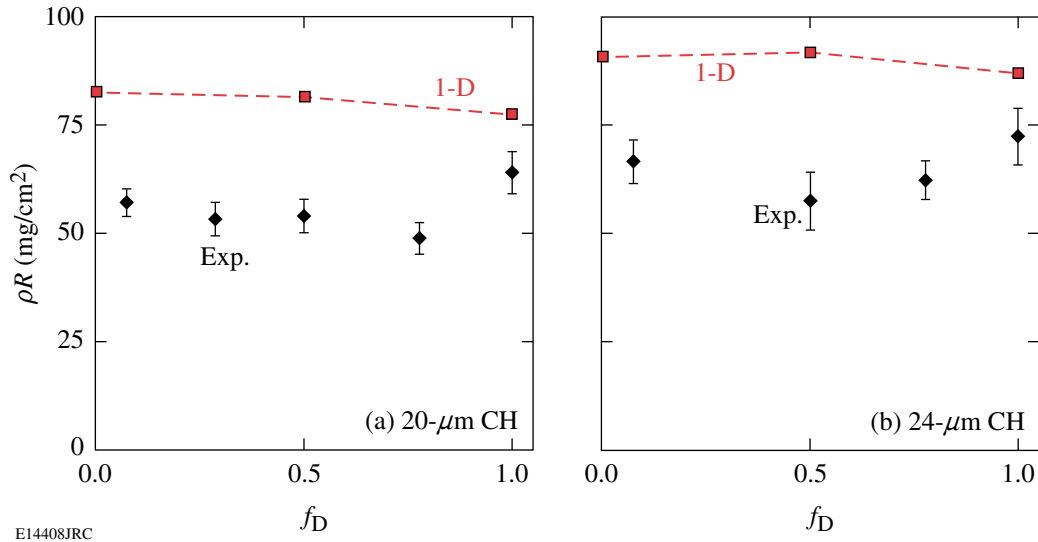


Figure 106.33 Inferred compression burn averaged ρR as a function of fill composition for high-pressure fills of (a) $20\text{-}\mu\text{m}$ -thick and (b) $24\text{-}\mu\text{m}$ -thick shells. The diamonds are the average and standard deviation of experimental observations. The squares and dotted lines are 1-D LILAC. For each plot, the higher ρR corresponds to more compression since all targets started with the same shell thickness.

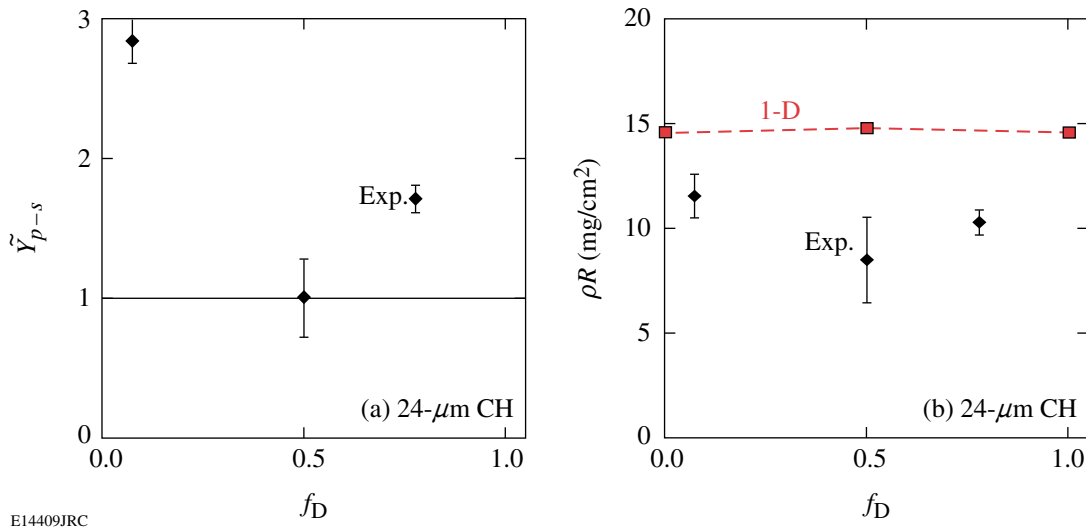


Figure 106.34 D^3He shock results for $24\text{-}\mu\text{m}$ CH capsules. (a) Scaled shock yield and (b) shock-yield-averaged ρR as a function of fill composition. The solid line is hydrodynamically equivalent scaling. The squares and dotted line are 1-D LILAC. Diamonds are the average and standard error of experimental observations.

Table 106.IX: D fraction by atom, number of shots averaged, DD- n , D³He compression and shock yields (scaled by fill composition and normalized to $f_D = 0.5$), ion temperature, areal density, and DD bang time for high-pressure fills for two different shell thicknesses.

Shell	f_D	Number of shots	$ \tilde{Y}_n $	$ \tilde{Y}_{p-c} $	$ \tilde{Y}_{p-s} $	T_i nTOF (keV)	T_i ratio (keV)	ρR (mg/cm ²)	t_{bang} (ns)
CH[20]	1.00	22	2.32	–	–	4.1	–	64	1.73
CH[20]	0.78	5	2.10	2.15	0.77	4.0	3.4	49	1.65
CH[20]	0.50	8	1.00	1.00	1.00	4.4	3.4	54	1.72
CH[20]	0.28	4	1.43	0.77	0.85	4.7	2.8	53	1.73
CH[20]	0.07	3	1.98	0.93	1.23	4.6	2.7	57	–
CH[24]	1.00	10	2.48	–	–	3.6	–	72	1.91
CH[24]	0.78	2	1.73	2.22	1.71	3.3	3.0	62	1.83
CH[24]	0.50	9	1.00	1.00	1.00	3.9	2.7	58	1.87
CH[24]	0.07	3	2.38	1.65	2.84	3.3	2.4	64	–

Discussion

A closer look at the possibility of a measurement error is certainly warranted when observations deviate so far from the scaling derived from simple principles as well as from computer simulations. The individual measurement error on a given shot is about 10% for both DD- n and D³He yields; however, the shot-to-shot yield variation for nominally identical shots is closer to 20% rms. Averaging the results from many like shots reduces the standard deviation of the mean considerably, in most cases below 10%. Systematic yield uncertainties in the diagnostics are unlikely to cause the yield scaling. The yield measurements for the two nuclear reactions use different diagnostics, using different principles, yet measured the same deviation.

The deviation in the yield scaling from Eq. (4) must then be explained through the differences in composition, temperature, density, burn volume, or burn duration of the target during the implosion. According to temporal measurements of nuclear burn histories, the implosion timing does not depend on the fill composition. Uncertainty in the composition is at most a couple of percent, which is not enough to affect the yields by a factor of 2. In addition, composition errors affect the DD- n and D³He yield scaling in different ways (Fig. 106.28), yet the same deviation is seen for both.

The observed trend of the ratio-inferred ion temperature could be part of the story because of the strong dependence of the thermal reactivities of both reactions at the temperatures of interest. The DD- n and D³He reactivities scale approximately as T_i^4 and T_i^7 near $T_i = 3$ keV. A linear fit through the observed ratio-inferred T_i in Fig. 106.32(d) was used to adjust

the hydrodynamically equivalent \tilde{Y}_n scaling. The solid curve in Fig. 106.35(a) plots this T_i ratio yield scaling against the observed yields from Fig. 106.30(c). This corrected scaling looks better for D-rich fuels but deviates further than the uncorrected hydrodynamically equivalent scaling from the observed yields for ³He-rich fuels. Since there was no clear trend in the nTOF-derived temperatures, a similar yield scaling fit was not done using the nTOF temperatures.

The two remaining factors of fuel density and burn volume are related to the compression of the capsule, which can be inferred by measurements of ρR . A simple model of the implosion that assumes that the shell temperature and shell aspect ratio at bang time does not depend on fill composition determines that the yield scales approximately as $(\rho R)^3$. The open circles in Fig. 106.35(b) plot this ρR yield scaling against the observed yields from Fig. 106.30(c). Higher ρR 's were observed for high and low D concentrations compared to the 50/50 mixture. The shape predicted from the $(\rho R)^3$ scaling is in qualitative agreement with the measurements, though it does not show quite as strong a scaling.

Although additional measurements suggest that some combination of ion temperature and density might be sufficient to explain the observed yield deviation, these factors must come from some physical mechanism, a number of which will be explored below.

The deviation from the assumed hydrodynamic equivalence is unlikely to be explained by 2-D or 3-D hydrodynamic effects, including hydrodynamic instabilities and turbulent mixing that

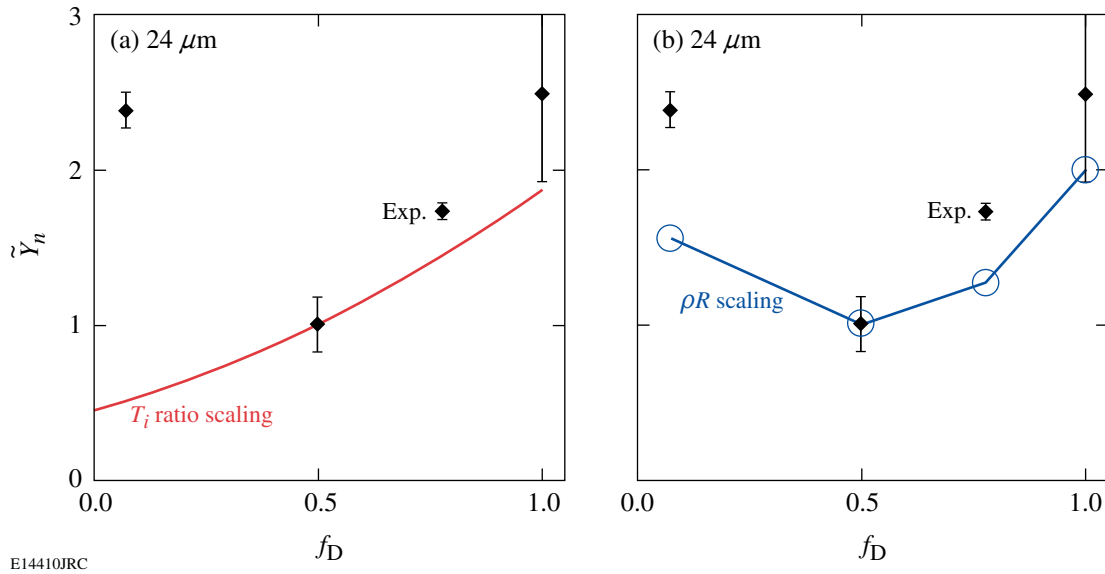


Figure 106.35

Measured (solid diamonds) DD- n yields as a function of f_D for 24- μm shells with high pressure from Fig. 106.30(c). In these plots, the hydrodynamically equivalent scaling has been adjusted to take into account the effects of measured ion temperature and areal density on the yield. (a) The solid line is a T_i -corrected scaling curve, based on a linear fit to the experimental T_i ratios in Fig. 106.32(d). (b) The open circles and connecting line include a ρR correction based on the measured ρR values shown in Fig. 106.33(b).

would reduce the burn volume and truncate the burn duration. A similar trend was experimentally observed over a wide range of physical situations in which 2-D hydrodynamic effects would likely have behaved very differently. Implosions with thicker shells are considered to be more hydrodynamically stable,²⁵ yet the same yield trend is seen for 20- and 24- μm shells with a high fill pressure. Implosions with a low fill pressure are considered less hydrodynamically stable, yet the yield trend is the same as for the high fill pressure (Fig. 106.31). A similar trend is also seen for D³He shock burn measurements, despite the fact that it has been shown that there is no atomic-level mixing in the burn region at shock time.²² Thus, pure hydrodynamics cannot explain the observed differences.

A wealth of data seems to exclude pure hydrodynamic differences between these mixtures as the mechanism for the observed variation in their yields (as it should be since they were chosen to be hydrodynamically equivalent). The deviation from hydrodynamic equivalence is likely to be due to the microscopic details of the mixture. It may have something to do with the variation in the average Z in the fuel, which varies from 1 (pure D₂) to nearly 2 (³He rich), the difference in ion masses or a subtlety in the statistical treatment of mixtures.

Bremsstrahlung radiation scales as $\sim \rho^2 T_e^{1/2} Z^3 / A^2$, which for these mixtures differs by a factor of 3.6 from pure D₂ (low)

to pure ³He, assuming the same density and temperature. A factor of 3 difference in the radiated power may then trigger differences in the absorption in the CH and initiate changes in the implosion dynamics. However, the yield discrepancy trend is about the same for cases with significantly different radiative properties, such as for low-pressure and high-pressure fills as well as at both shock and compression time. The difference in density in these scenarios radically affects the efficiency of bremsstrahlung radiation. In addition, the yield deviation is not monotonic with the D fraction, so bremsstrahlung radiation seems unlikely as the sole mechanism.

Thermal conduction in these dynamic implosions can be difficult to calculate because of nonequilibrium conditions and other nonlocal effects. To get a sense of the scaling, however, consider the Spitzer–Harm electron thermal conduction²⁶

$$q_{\text{SH}} = -K \nabla T,$$

$$K \propto \delta(Z) \frac{T_e^{5/2}}{Z m_e^{1/2} \ln \Lambda},$$

$$\delta(Z) = \frac{Z + 0.24}{Z + 0.42}. \quad (7)$$

Ignoring the Coulomb logarithm variation, pure D_2 has a 32% higher classical conductivity than pure ${}^3\text{He}$ and is 17% higher than the standard D_2 - ${}^3\text{He}$ mixture (using “average” ions). Ion thermal conduction has a similar form, but with a much stronger Z dependence.²⁷ Ion conduction is relatively small when the ion and electron temperatures are equal but can become important when the ion temperature is higher, such as for shock heating. But for both types of thermal conduction, the trend is again monotonic with a D fraction.

Shock heating initially puts most energy into heating the ions, with more energy going to heavier ions.²⁸ Equal-density mixtures of D_2 and ${}^3\text{He}$ will absorb the same total amount of energy from a shock front, but mixtures with a higher concentration of ${}^3\text{He}$ will have a higher initial ion temperature due to the higher average ion mass (and corresponding lower ion density). A slight difference in this initial state of the gas might, after compression, be enough to change the dynamics and the resulting nuclear yields. The compression condition will be quite a bit different for the different implosion types (high and low pressure, thin and thick shells), yet the same deviation is seen in many cases. It is also difficult to explain the nonmonotonic trend with this picture.

It is possible that there is stratification of the ion species during the deceleration phase. The scaled performance of the “pure” fuels seems to be greatest, so perhaps the mixture of different species is important. During the deceleration phase, the ${}^3\text{He}$ concentration might be slightly enhanced near the center. The hot center will then have a lower nuclear yield due to scarcer D ions. In this picture, though, the ${}^3\text{He}$ -rich fuels should also have a reduced yield, so the nonmonotonic trend is again a problem.

The plausibility of stratification can be considered using simple arguments. Because of the high density during the compression phase, any concentration enhancement will have to come through a difference in diffusion of the D and ${}^3\text{He}$ ions. With plasma parameters typical of the fill early in the compression burn (4 keV, 3 g/cc), it is found that the time it takes even one particle to diffuse across the capsule is very much longer than the implosion time.

Kinetic effects could play an important role in the observed yield scaling. A non-Maxwellian velocity distribution could significantly alter nuclear production, particularly at the time of shock collapse, where the distribution is far from Maxwellian. It has also been suggested that yield degradation could result from the loss of ions in the tail of the distribution, which

normally dominate the nuclear production. The longer mean free paths of the ions in the tail may allow them to escape the fuel region if the $\rho R < 10$ mg/cm² (Ref. 29). It is not sufficient, though, that kinetic effects only change the nuclear production; a kinetic effect must change the nuclear production nonmonotonically with the D fraction and by a factor of 2 between pure and mixed D and ${}^3\text{He}$.

Many processes used to explain the observed yield scaling have been considered here but no single mechanism is sufficient to explain the trend.

Summary

In summary, experimental observations of the scaling of nuclear yields from implosions with hydrodynamically equivalent mixtures of D_2 and ${}^3\text{He}$ deviate from the scaling determined using a simple consideration of composition ratios as well as from a scaling based on 1-D radiation-hydrodynamic simulations. This deviation is particularly puzzling since the trend is not monotonic with the D fraction; the scaled $D^3\text{He}$ yield is lower than the scaled yields on both the D_2 -rich and ${}^3\text{He}$ -rich sides.

The same scaling deviation is observed in diverse physical situations, including implosions of targets with initial fill pressures of 3 and 15 atm and target shell thicknesses of 15, 20, 24, and 27 μm of CH. A similar yield scaling deviation is observed for both DD- n and $D^3\text{He}$ yields despite the drastically different dependence of their yields on composition and temperature. Overall, a similar scaling deviation is seen for both the shock and compression components of the $D^3\text{He}$ yield, corresponding to times separated by several hundred picoseconds and reflecting very different plasma conditions.

It has been shown that measurements of the burn-averaged ion temperature, using two different methods, are insufficient to explain the entire yield scaling deviation. Errors in the initial fill composition of the D_2 and ${}^3\text{He}$ mixtures and differences in the implosion timing have also been excluded. Measurements of the burn-averaged areal density ρR suggest that D_2 and ${}^3\text{He}$ mixtures with a f_D near 0.5 might experience less compression, resulting in a lower yield.

A number of possible mechanisms that may cause the scaling are considered, but no dominant mechanism has been identified. Differences in the radiative and transport properties of different D_2 and ${}^3\text{He}$ mixtures are included in 1-D simulations, but apparently do not have as great an effect on the yield as what was observed. Hydrodynamic instabilities in 2-D and

3-D appear to be ruled out. The initial gas state set by the converging shock, ion species stratification, and kinetic effects were also considered.

This study raises some concern as to the near equivalence of D₂ as a DT fuel surrogate for studying implosion dynamics. Even when the mass density of the D₂ and ³He mixtures is the same, we see discrepancies in the yield although it is not clear what mechanism causes the discrepancy and whether it is due to a difference in the average Z, ion masses, or transport properties of mixed materials. To explore such issues, further scrutiny of the ion conductivity and its effects on implosion dynamics is underway, which may be an important factor because of its strong Z dependence.

An investigation of the yield scaling at constant Z could be accomplished by using different fuel mixtures, including mixtures of D and T, and an extension of this study with mixtures of D₂, ³He, and either H₂ or ⁴He. Experiments are being actively planned that would vary the D and T mixture with the intention of simultaneously measuring the absolute yield of both DT and DD,³⁰ the results of which will have direct relevance for ignition target fills and will take us a step closer to understanding the present conundrum.

ACKNOWLEDGMENT

The authors express their gratitude to the OMEGA engineers and operations crew who supported these experiments. This work was supported in part by the U.S. Department of Energy Office of Inertial Confinement Fusion (Grant No. DE-FG03-03NA00058), by the Lawrence Livermore National Laboratory (Subcontract No. B543881), and by the Laboratory for Laser Energetics (Subcontract No. 412160-001G) under Cooperative Agreement DE-FC52-92SF19460, University of Rochester, and New York State Energy Research and Development Authority.

REFERENCES

1. J. Nuckolls *et al.*, *Nature* **239**, 139 (1972).
2. J. D. Lindl, *Inertial Confinement Fusion: The Quest for Ignition and Energy Gain Using Indirect Drive* (Springer-Verlag, New York, 1998).
3. S. Atzeni and J. Meyer-ter-Vehn, *The Physics of Inertial Fusion: Beam Plasma Interaction, Hydrodynamics, Hot Dense Matter*, International Series of Monographs on Physics (Clarendon Press, Oxford, 2004).
4. S. E. Bodner, D. G. Colombant, J. H. Gardner, R. H. Lehmborg, S. P. Obenschain, L. Phillips, A. J. Schmitt, J. D. Sethian, R. L. McCrory, W. Seka, C. P. Verdon, J. P. Knauer, B. B. Afeyan, and H. T. Powell, *Phys. Plasmas* **5**, 1901 (1998).
5. F. J. Marshall, J. A. Delettrez, V. Yu. Glebov, R. P. J. Town, B. Yaakobi, R. L. Kremens, and M. Cable, *Phys. Plasmas* **7**, 1006 (2000).
6. R. L. McCrory, R. E. Bahr, R. Betti, T. R. Boehly, T. J. B. Collins, R. S. Craxton, J. A. Delettrez, W. R. Donaldson, R. Epstein, J. Frenje, V. Yu. Glebov, V. N. Goncharov, O. Gotchev, R. Q. Gram, D. R. Harding, D. G. Hicks, P. A. Jaanimagi, R. L. Keck, J. Kelly, J. P. Knauer, C. K. Li, S. J. Loucks, L. D. Lund, F. J. Marshall, P. W. McKenty, D. D. Meyerhofer, S. F. B. Morse, R. D. Petrasso, P. B. Radha, S. P. Regan, S. Roberts, F. Séguin, W. Seka, S. Skupsky, V. Smalyuk, C. Sorce, J. M. Soures, C. Stoeckl, R. P. J. Town, M. D. Wittman, B. Yaakobi, and J. D. Zuegel, *Nucl. Fusion* **41**, 1413 (2001).
7. S. P. Regan, J. A. Delettrez, V. Yu. Glebov, V. N. Goncharov, J. P. Knauer, J. A. Marozas, F. J. Marshall, R. L. McCrory, P. W. McKenty, D. D. Meyerhofer, P. B. Radha, T. C. Sangster, S. Skupsky, V. A. Smalyuk, C. Stoeckl, J. R. Rygg, J. A. Frenje, C. K. Li, R. D. Petrasso, and F. H. Séguin, *Bull. Am. Phys. Soc.* **50**, 113 (2005).
8. F. H. Séguin, J. A. Frenje, C. K. Li, D. G. Hicks, S. Kurebayashi, J. R. Rygg, B.-E. Schwartz, R. D. Petrasso, S. Roberts, J. M. Soures, D. D. Meyerhofer, T. C. Sangster, J. P. Knauer, C. Sorce, V. Yu. Glebov, C. Stoeckl, T. W. Phillips, R. J. Leeper, K. Fletcher, and S. Padalino, *Rev. Sci. Instrum.* **74**, 975 (2003).
9. J. A. Frenje, C. K. Li, F. H. Séguin, J. Deciantis, S. Kurebayashi, J. R. Rygg, R. D. Petrasso, J. Delettrez, V. Yu. Glebov, C. Stoeckl, F. J. Marshall, D. D. Meyerhofer, T. C. Sangster, V. A. Smalyuk, and J. M. Soures, *Phys. Plasmas* **11**, 2798 (2003).
10. F. H. Séguin, J. L. DeCiantis, J. A. Frenje, S. Kurebayashi, C. K. Li, J. R. Rygg, C. Chen, V. Berube, B. E. Schwartz, R. D. Petrasso, V. A. Smalyuk, F. J. Marshall, J. P. Knauer, J. A. Delettrez, P. W. McKenty, D. D. Meyerhofer, S. Roberts, T. C. Sangster, K. Mikaelian, and H. S. Park, *Rev. Sci. Instrum.* **75**, 3520 (2004).
11. T. R. Boehly, D. L. Brown, R. S. Craxton, R. L. Keck, J. P. Knauer, J. H. Kelly, T. J. Kessler, S. A. Kumpan, S. J. Loucks, S. A. Letzring, F. J. Marshall, R. L. McCrory, S. F. B. Morse, W. Seka, J. M. Soures, and C. P. Verdon, *Opt. Commun.* **133**, 495 (1997).
12. F. J. Marshall, J. A. Delettrez, R. Epstein, R. Forties, R. L. Keck, J. H. Kelly, P. W. McKenty, S. P. Regan, and L. J. Waxer, *Phys. Plasmas* **11**, 251 (2004).
13. S. Skupsky and R. S. Craxton, *Phys. Plasmas* **6**, 2157 (1999).
14. The $f_D = 0.78$ shots plotted on the 20- μm -CH figures actually had 19- μm -thick shells.
15. M. J. Bonino, Laboratory for Laser Energetics, private communication (2006).
16. H.-S. Bosch and G. M. Hale, *Nucl. Fusion* **32**, 611 (1992).
17. R. A. Lerche and T. J. Murphy, *Rev. Sci. Instrum.* **63**, 4880 (1992).
18. Tangential electric fields have not been excluded as the cause for the anisotropic proton emission, but for these implosions there is no radial E field when the protons are emitted.
19. C. K. Li, D. G. Hicks, F. H. Séguin, J. A. Frenje, R. D. Petrasso, J. M. Soures, P. B. Radha, V. Yu. Glebov, C. Stoeckl, D. R. Harding, J. P. Knauer, R. L. Kremens, F. J. Marshall, D. D. Meyerhofer, S. Skupsky, S. Roberts, C. Sorce, T. C. Sangster, T. W. Phillips, M. D. Cable, and R. J. Leeper, *Phys. Plasmas* **7**, 2578 (2000).
20. R. A. Lerche, D. W. Phillion, and G. L. Tietbohl, *Rev. Sci. Instrum.* **66**, 933 (1995).

21. C. Stoeckl, V. Yu. Glebov, S. Roberts, T. C. Sangster, R. A. Lerche, R. L. Griffith, and C. Sorce, *Rev. Sci. Instrum.* **74**, 1713 (2003).
22. R. D. Petrasso, J. A. Frenje, C. K. Li, F. H. Séguin, J. R. Rygg, B. E. Schwartz, S. Kurebayashi, P. B. Radha, C. Stoeckl, J. M. Soures, J. Delettrez, V. Yu. Glebov, D. D. Meyerhofer, and T. C. Sangster, *Phys. Rev. Lett.* **90**, 095002 (2003).
23. J. Delettrez, R. Epstein, M. C. Richardson, P. A. Jaanimagi, and B. L. Henke, *Phys. Rev. A* **36**, 3926 (1987).
24. Except for the D^3He yield from 3He -rich, 20- μm -thick target implosions.
25. S. P. Regan, J. A. Delettrez, V. N. Goncharov, F. J. Marshall, J. M. Soures, V. A. Smalyuk, P. B. Radha, B. Yaakobi, R. Epstein, V. Yu. Glebov, P. A. Jaanimagi, D. D. Meyerhofer, T. C. Sangster, W. Seka, S. Skupsky, C. Stoeckl, D. A. Haynes, Jr., J. A. Frenje, C. K. Li, R. D. Petrasso, and F. H. Séguin, *Phys. Rev. Lett.* **92**, 185002 (2004).
26. L. Spitzer, Jr. and R. Härm, *Phys. Rev.* **89**, 977 (1953).
27. S. I. Braginskii, in *Reviews of Plasma Physics*, edited by Acad. M. A. Leontovich (Consultants Bureau, New York, 1965), Vol. 1, p. 205.
28. Ya. B. Zel'dovich and Yu. P. Raizer, *Physics of Shock Waves and High-Temperature Hydrodynamic Phenomena*, edited by W. D. Hayes and R. F. Probstein (Dover Publications, Mineola, NY, 2002).
29. D. B. Henderson, *Phys. Rev. Lett.* **33**, 1142 (1974).
30. Only recent technological advances have made the detection of DD neutrons in the background of DT neutrons feasible. See V. Yu. Glebov, D. D. Meyerhofer, T. C. Sangster, C. Stoeckl, S. Roberts, C. A. Barrera, J. R. Celeste, L. S. Dauffy, C. J. Cerjan, D. C. Eder, R. L. Griffith, S. W. Haan, B. A. Hammel, S. P. Hatchett, N. Izumi, J. R. Kimbrough, J. A. Koch, O. L. Landen, R. A. Lerche, B. J. MacGowan, M. J. Moran, E. W. Ng, T. W. Phillips, P. M. Song, R. Tommassini, B. K. F. Young, S. E. Caldwell, G. P. Grim, S. C. Evans, L. Disdier, M. Houry, I. Lantuejoul, G. A. Chandler, G. W. Cooper, R. J. Lepeer, R. E. Olson, C. L. Ruiz, M. A. Sweeney, S. P. Padalino, C. Horsfield, and B. A. Davis, "Development of Nuclear Diagnostics for the National Ignition Facility," to be presented at the 16th Topical Conference on High-Temperature Diagnostics, Williamsburg, VA, 7–11 May 2006.

Deterministically Polarized Fluorescence from Uniaxially Aligned Single-Dye Molecules

Introduction

In single-photon sources (SPS's) based on single-emitter fluorescence, a laser beam is focused into an area containing a low concentration of single emitters so that only one emitter becomes excited. The single emitter produces a single photon at a time.^{1–4} There are various known methods for the production of single photons at definite time intervals, which are based on a single atom,^{5,6} a single trapped ion,⁷ a single molecule,^{8–10} a single color center in diamond,¹¹ or the Coulomb-blockade effect in a micropin junction with quantum well as the active layer.^{12–14} Tremendous progress has been made in the realization of SPS's based on excitonic emission from single heterostructured semiconductor quantum dots excited by pulsed laser light (see Refs. 1 and 3). In heterostructured quantum-dot SPS's,^{15–28} microcavities have been used for spontaneous emission enhancement in the form of a whispering-gallery-mode resonator (turnstile device), 1-D photonic band gap, 3-D pillar microcavity, and 2-D photonic crystals. A weakness of heterostructured quantum-dot SPS's is that they operate *only at liquid-helium temperatures*. In addition, they are not readily tunable. To date, three approaches have been suggested for *room-temperature* SPS's: single molecules,^{8–10,29–37} colloidal semiconductor quantum dots (nanocrystals),^{38,39} and color centers in diamond.^{11,40–43} The color-center source suffers from the challenge that it is not easy to couple out the photons and that the spectral bandwidth of the light is typically quite large (~120 nm).

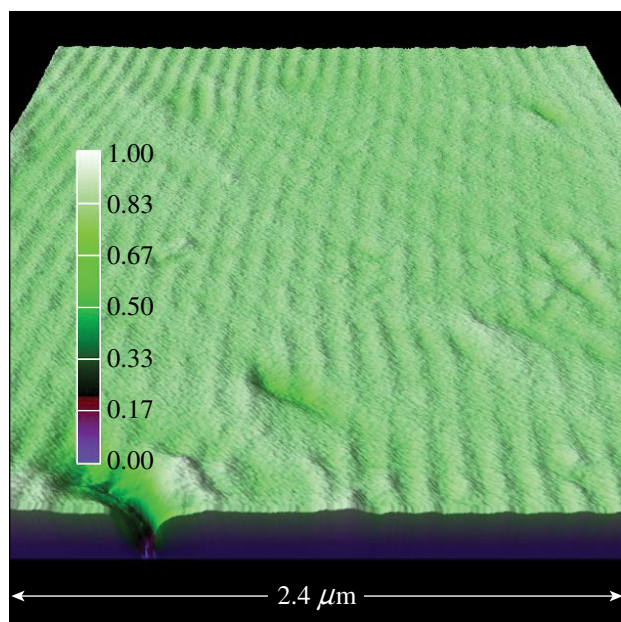
Both single molecules and colloidal semiconductor nanocrystals dissolved in a proper solvent can be embedded in photonic crystals to circumvent the deficiencies that plague the other systems. Colloidal semiconductor nanocrystals dissolved in PMMA were placed inside a 2-D photonic crystal cavity.⁴⁴ The nanocrystal emission at room temperature mapped out the cavity resonances and was enhanced relative to the bulk emission. A planar cavity was recently used to control the single-dye molecule fluorescence spectra and decay rate.⁴⁵ The primary problems with using fluorescent dyes and colloidal semiconductor nanocrystals in cavities are the emitters bleaching and blinking, nontunability of the source, and nondeterministic polarization of photons.

Our solution is based on a new material concept using single-emitter excitation in specially prepared *liquid crystal hosts*, which can exist both as monomers (fluid media) and oligomers or polymers. The advantages of using liquid crystal hosts are that they may be self-assembled in structures with photonic band-gap properties, and, at the same time, such a host can protect the emitters from bleaching. This source is a *room-temperature* alternative to cryogenic SPS's based on semiconductor heterostructures. In addition, the liquid crystal host provides both polarization purity and tunability of the source. Recent advances in liquid crystal technology, especially in the fabrication of electric-field/temperature-controlled 1-D, 2-D, and 3-D photonic crystal structures and the infiltration of photonic crystals with liquid crystals, can be used in SPS preparation with properties that other SPS methods failed to provide.

Recently we reported a first demonstration of dye-fluorescence antibunching in liquid crystal hosts^{35–37} that is evidence of the single-photon nature of the source. One-dimensional (Fig. 106.36) and two-dimensional (Fig. 106.37) photonic crystal structures were prepared.^{35–37,46} One-dimensional photonic band-gap structures in cholesteric liquid crystals possess an additional advantage over conventional 1-D photonic crystals. Because the refractive index n varies gradually rather than abruptly in cholesterics, there are no losses into the waveguide modes, which, in the case of conventional 1-D photonic crystals, arise from total internal reflection at the border between two consecutive layers with a different n . These waveguide losses can reach ~20%.

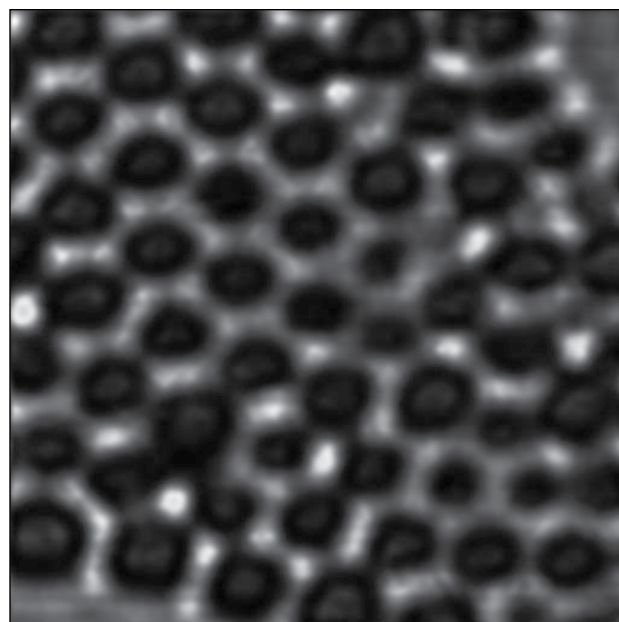
In addition, we observed a significant diminishing of dye bleaching by special preparation of liquid crystals; dye molecules did not bleach for periods of more than one hour under cw excitation.^{35–37} (The first impressive experiments on avoiding dye bleaching in the hosts have been reported in Refs. 9 and 30. In Ref. 9, single terrylene-dye molecules in a *p*-terphenyl molecular crystal host did not bleach during several hours of pulsed, several-megahertz, pulse-repetition-rate excitation).

This article highlights another advantage of liquid-crystal hosts—*deterministically polarized* fluorescence from single-



G7148JRC

Figure 106.36
Perspective view of the AFM topographical image of a 1-D photonic band gap, planar-aligned, glassy, cholesteric liquid crystal.



G7149JR

Figure 106.37
Near-field optical image of a 2-D photonic crystal self-assembly of a glassy cholesteric liquid crystal ($5\text{-}\mu\text{m} \times 5\text{-}\mu\text{m}$ scan).

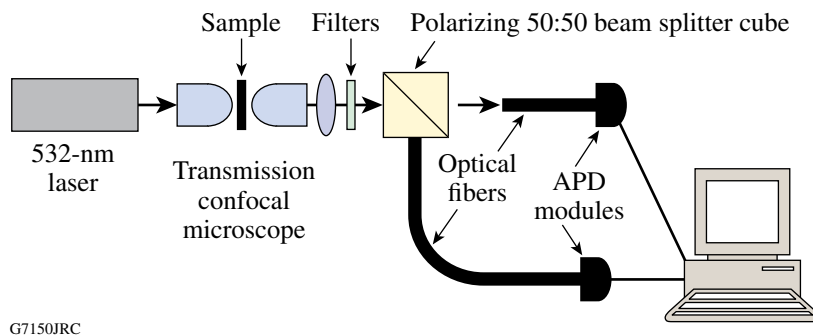
dye molecules.^{47–49} Single molecules of DiIC₁₈(3) dye were embedded in a planar-aligned, glassy, *nematic* liquid crystal host and were aligned by liquid crystal molecules.

Experimental Setup

Single-molecule fluorescence microscopy was carried out on a Witec alpha-SNOM device in confocal transmission mode. Figure 106.38 shows the schematic of this experiment. The dye-doped liquid crystal sample was placed in the focal plane of a 1.4 numerical aperture, oil-immersion microscope objective. The sample was attached to a piezoelectric, XYZ translation stage. Light emitted by the sample was collected by a confocal setup using a 1.25 numerical aperture, oil-immersion objective with an aperture in the form of an optical

fiber. The cw, spatially filtered (through a single-mode fiber), 532-nm, diode-pumped, Nd:YAG laser output excited single molecules. In focus, the intensities used were of the order of several kW/cm^2 .

For polarized fluorescence measurements, we used a 50/50 polarizing beam splitter cube (as opposed to our antibunching correlation measurements,^{35–37} in which a nonpolarizing beam splitter was used) with the confocal microscope apertures in the form of a 100- μm -core optical fiber placed in each arm of the beam splitter's output (Fig. 106.38). Residual transmitted excitation light was removed by two consecutive dielectric interference filters, yielding a combined rejection of better than 6 orders of magnitude at 532 nm.



G7150JRC

Figure 106.38
Experimental setup.

Photons in the two arms were detected by identical cooled avalanche photodiode modules (APD) in single-photon-counting Geiger mode (Perkin Elmer SPCM AQR-14).

Experimental Results: Deterministically Polarized Single-Molecule Fluorescence

For these experiments, we used DiIC₁₈(3) dye (Fig. 106.39) in planar-aligned, glassy, nematic liquid crystal hosts⁵⁰ with a concentration of $\sim 10^{-8}$ M. The nematic liquid crystal state of this material, which exists at elevated temperatures, is preserved at room temperature by slowly cooling the liquid crystal to the glassy state with frozen nematic order. We prepared ~ 100 -nm-thick films of this glassy, nematic liquid crystal that was doped with dye molecules that were aligned deterministically through photoalignment using Staralign LPP coating and linearly polarized UV light. This new alignment technique prevents material contamination by particulates. We succeeded in the preparation of such an alignment over areas exceeding $10 \text{ mm} \times 10 \text{ mm}$ (Refs. 47–49).

Figure 106.40 shows images of single-molecule fluorescence for polarization components (a) perpendicular and (b) parallel to the alignment direction under 532-nm cw excitation. These two components in the sample plane have been separated with a polarizing beam splitter cube (Fig. 106.38). Figure 106.40 clearly shows that for this sample, the polarization direction of the fluorescence of single molecules is predominantly in the direction perpendicular to the alignment of liquid crystal molecules. It is important that the background levels of Figs. 106.40(a) and 106.40(b) are the same (~ 10 counts/pixel or ~ 640 counts/s). The single-molecule fluorescence signal at maximum exceeds this background by up to 15 times.

The polarization anisotropy is defined here as $\rho = (I_{\text{par}} - I_{\text{perp}}) / (I_{\text{par}} + I_{\text{perp}})$, where I_{par} and I_{perp} are fluorescence intensities for polarization components parallel and perpendicular to the alignment direction.⁵¹ Processing the images in Fig. 106.40 shows that from a total of 38 molecules, 31 molecules have a negative ρ value (Fig. 106.41). The same

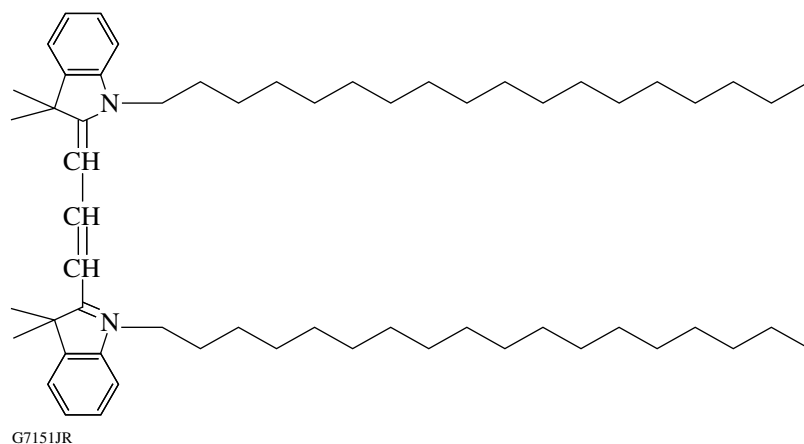


Figure 106.39
Molecular structure of DiIC₁₈(3) dye.

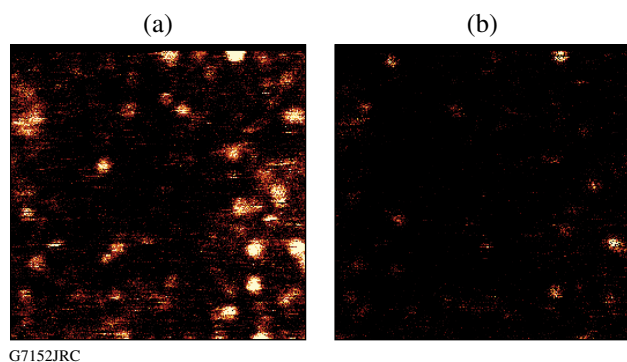


Figure 106.40
Confocal fluorescence microscopy images of DiIC₁₈(3) single-molecule fluorescence in a planar-aligned, glassy, nematic liquid crystal host ($10\text{-}\mu\text{m} \times 10\text{-}\mu\text{m}$ scan): (a) polarization perpendicular to the alignment direction and (b) parallel polarization.

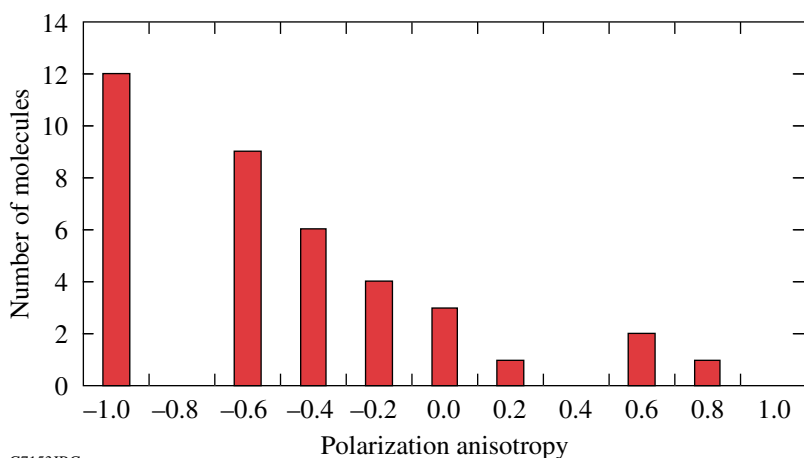


Figure 106.41

A histogram of the polarization anisotropy of 38 molecules of DiIC₁₈(3) dye in a planar-aligned, glassy, nematic liquid crystal host.

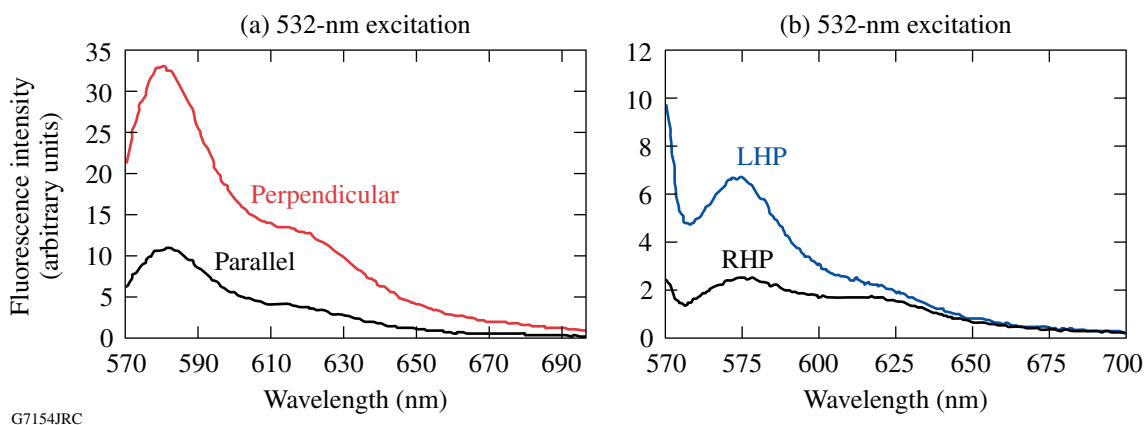
G7153JRC

sign of the polarization anisotropy was obtained in spectrofluorimeter measurements for a sample with a high (~0.5%) by weight concentration of the same dye in a planar-aligned, glassy, nematic liquid crystal layer that is ~4.1- μm thick [Fig. 106.42(a)]. Figure 106.42(b) shows *circular* polarized fluorescence from a planar-aligned, glassy, *chiral*-nematic (cholesteric) liquid crystal layer that is ~4.1- μm thick and has a 0.5% by weight concentration of DiIC₁₈(3) dye.

This predominance of “perpendicular” polarization in Figs. 106.40, 106.41, and 106.42(a) can be explained by the DiIC₁₈(3)’s molecular structure (Fig. 106.39). The two alkyl chains likely orient themselves parallel to the rod-like liquid crystal molecules, but the emitting/absorbing dipoles that are nearly parallel to the bridge (perpendicular to alkyl chains) will be directed perpendicular to the liquid crystal alignment. DiIC₁₈(3) molecules orient in the same manner in cell mem-

branes.^{52,53} It should be noted that in Ref. 54, single terrylene dye molecules were uniaxially oriented in rubbed polyethylene; however, this paper did not provide the results on deterministically polarized fluorescence of single molecules.

Note that the images in Fig. 106.40 were taken by raster scanning the sample relative to the stationary, focused laser beam. The scan direction was from left to right, line by line, from top to bottom. The size of the bright features is defined by the point-spread function of the focused laser beam. These images not only contain information about the spatial position of the fluorescent molecules, but also about the changes of their fluorescence in time. Dark horizontal stripes and bright semicircles instead of circles represent the blinking and bleaching of the molecules in time. Blinking and bleaching are a common single-molecule phenomenon and convincing evidence of the single-photon nature of the source. The explanation of the nature of the long-



G7154JRC

Figure 106.42

Spectrofluorimeter measurements of a polarized fluorescence of DiIC₁₈(3) dye doped in planar-aligned, glassy, liquid crystal hosts under excitation with a nonpolarized, 532-nm light. (a) Fluorescence spectra in a nematic host for different linear polarizations. (b) Fluorescence spectra in a cholesteric host for circular polarization of different handedness.

time blinking from milliseconds to several seconds remains a subject of debate in the literature (see, e.g., Ref. 55).

The maximum count rate of single-molecule images was approximately 10 kcounts/s (~160 counts/pixel with ~4 s per line scan, 256 pixels per line) with a fluorescence molecule lifetime of approximately several nanoseconds. Note that the detector dark counts were fewer than 100 counts/s.

Seven molecules in Figs. 106.40 and 106.41 have either positive or zero anisotropy. These molecules can be either a small amount of impurities in the Staralign photoalignment agent, which have not been bleached even after the UV irradiation of Staralign-coated slips, or impurities of the glassy oligomer host.⁵⁶ Figure 106.43(a) shows single-molecule fluorescence images of the Staralign photoalignment agent before UV irradiation. The single-molecule fluorescence microscopy method is very sensitive to material impurities. We sometimes observed single-molecule fluorescence from the impurities in glassy LC oligomers [Fig. 106.43(b)] even when a chromatographic analysis did not detect them. For this reason, the Polyimide and Nylon 6/6 thin films usually used for buffing alignment were not utilized in our experiments because of the finding that they possess a higher fluorescence count rate than single molecules of fluorescence dyes.

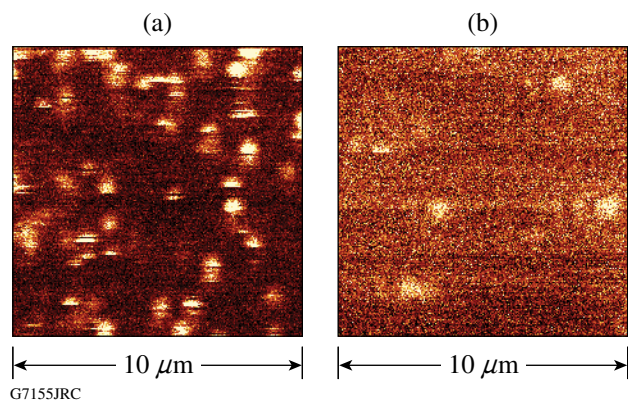


Figure 106.43
Parasitic fluorescence from single-molecule impurities in the Staralign photoalignment agent without (a) UV treatment and (b) undoped oligomer material.

Conclusions

This article shows the advantages of using liquid crystals as the hosts for single-photon sources; deterministically polarized fluorescence from single emitters embedded in liquid crystal hosts was demonstrated for the first time at room temperature. Single-dye molecules were deterministically aligned by liquid crystal molecules in one direction and produced deterministically linearly polarized single photons.

Circularly polarized single photons with deterministic handedness [see, e.g., Fig. 160.42(b) for a high dye concentration] can be produced efficiently using 1-D photonic band gaps in cholesteric liquid crystals matching the dye-fluorescence band. We hope to increase SPS efficiency in cholesteric liquid crystal, 1-D photonic-band-gap structures from the current 4% to at least 40% (see Ref. 35) to narrow the fluorescence bandwidth (to ~1 to 10 nm) and decrease the fluorescent lifetime from a few nanoseconds to the hundreds of picoseconds necessary for high-speed communications. One-dimensional photonic band-gap structures in cholesteric liquid crystals, 2-D/3-D photonic crystals in holographic polymer-dispersed liquid crystals,⁵⁷ a 3-D photonic crystal structure of a liquid crystal blue phase,⁵⁸ and photonic crystals/microstructured fibers infiltrated with liquid crystals^{59,60} may be prepared for this purpose. By using various fluorescence emitters [dye molecules, colloidal semiconductor nanocrystals (dots and rods), carbon nanotubes, and rare-earth ions], it will be possible to extend the working region of the source from the visible to communication wavelengths (1.3 and 1.55 μm).

ACKNOWLEDGEMENT

The authors acknowledge the support by the U.S. ARO under Award No. DAAD19-02-1-0285, NSF Awards ECS-0420888, EEC-0243779, PHY-0242483, and the U.S. Department of Energy Office of Inertial Confinement Fusion Award under Cooperative Agreement No. DE-FC52-92SF19460. The receipt of liquid crystals from Prof. S.-H. Chen is gratefully acknowledged. The authors thank L. Novotny, A. Lieb, A. Trajkovska, and S. Culligan for advice and help; S. Papernov for help in AFM imaging; and J. Dowling for the discussion that provided a better understanding of the fluorescence in chiral-nematic structures.

REFERENCES

1. Y. Yamamoto *et al.*, Prog. Informatics, No. 1, 5 (2005).
2. B. Lounis and M. Orrit, Rep. Prog. Phys. **68**, 1129 (2005).
3. P. Kumar *et al.*, Quantum Information Processing **3**, 215 (2004).
4. P. Grangier, B. Sanders, and J. Vučković, eds., New J. Phys. **6** (2004).
5. A. Kuhn, M. Hennrich, and G. Rempe, Phys. Rev. Lett. **89**, 067901 (2002).
6. J. McKeever *et al.*, Science **303**, 1992 (2004).
7. Ch. Schwedes *et al.*, Phys. Rev. A **69**, 053412 (2004).
8. C. Brunel *et al.*, Phys. Rev. Lett. **83**, 2722 (1999).
9. B. Lounis and W. E. Moerner, Nature **407**, 491 (2000).
10. F. Treussart *et al.*, Phys. Rev. Lett. **89**, 093601 (2002).
11. A. Beveratos *et al.*, Eur. Phys. J. D **18**, 191 (2002).

12. A. Imamoglu and Y. Yamamoto, *Phys. Rev. Lett.* **72**, 210 (1994).
13. J. Kim *et al.*, *Nature* **397**, 500 (1999).
14. E. Moreau *et al.*, *Appl. Phys. Lett.* **79**, 2865 (2001).
15. P. Michler *et al.*, *Science* **290**, 2282 (2000).
16. C. Santori *et al.*, *Phys. Rev. Lett.* **86**, 1502 (2001).
17. J. Vučković *et al.*, *Appl. Phys. Lett.* **82**, 3596 (2003).
18. C. Santori, D. Fattal, and J. Vučković, *Nature* **419**, 594 (2002).
19. W.-H. Chang *et al.*, *Phys. Rev. Lett.* **96**, 117401 (2006).
20. V. Zwiller *et al.*, *Appl. Phys. Lett.* **78**, 2476 (2001).
21. Z. Yuan *et al.*, *Science* **295**, 102 (2001).
22. G. S. Solomon, M. Pelton, and Y. Yamamoto, *Phys. Rev. Lett.* **86**, 3903 (2001).
23. B. Gayral *et al.*, *Appl. Phys. Lett.* **72**, 1421 (1998).
24. D. Englund *et al.*, *Phys. Rev. Lett.* **95**, 013904 (2005).
25. A. Daraei *et al.*, *Appl. Phys. Lett.* **88**, 051113 (2006).
26. D. C. Unitt *et al.*, *Phys. Rev. B* **72**, 033318 (2005).
27. C. Santori *et al.*, *New J. Phys.* **6**, 89 (2004).
28. M. Benyoucef *et al.*, *New J. Phys.* **6**, 91 (2004).
29. W. P. Ambrose *et al.*, *Chem. Phys. Lett.* **269**, 365 (1997).
30. L. Fleury *et al.*, *Phys. Rev. Lett.* **84**, 1148 (2000).
31. F. Treussart *et al.*, *Opt. Lett.* **26**, 1504 (2001).
32. P. Kumar *et al.*, *J. Am. Chem. Soc.* **126**, 3376 (2004).
33. C. W. Hollars, S. M. Lane, and T. Huser, *Chem. Phys. Lett.* **370**, 393 (2003).
34. D. A. Bussian *et al.*, *Chem. Phys. Lett.* **388**, 181 (2004).
35. S. G. Lukishova, A. W. Schmid, A. J. McNamara, R. W. Boyd, and C. R. Stroud, Jr., *IEEE J. Sel. Top. Quantum Electron.* **9**, 1512 (2003).
36. S. G. Lukishova, A. W. Schmid, C. M. Supranowitz, N. Lippa, A. J. McNamara, R. W. Boyd, and C. R. Stroud, Jr., *J. Mod. Opt.* **51**, 1535 (2004).
37. *LLE Review Quarterly Report* **94**, 97, Laboratory for Laser Energetics, University of Rochester, Rochester, NY, LLE Document No. DOE/SF/19460/485, NTIS Order No. PB2006-106666 (2003). Copies may be obtained from the National Technical Information Service, Springfield, VA 22161.
38. B. Lounis *et al.*, *Chem. Phys. Lett.* **329**, 399 (2000).
39. G. Messin, *Opt. Lett.* **26**, 1891 (2001).
40. A. Beveratos *et al.*, *Phys. Rev. Lett.* **89**, 187901 (2002).
41. C. Kurtsiefer *et al.*, *Phys. Rev. Lett.* **85**, 290 (2000).
42. R. Brouri *et al.*, *Opt. Lett.* **25**, 1294 (2000).
43. A. Beveratos *et al.*, *Phys. Rev. A* **64**, 061802(R) (2001).
44. I. Fushman, D. Englund, and J. Vučković, *Appl. Phys. Lett.* **87**, 241102 (2005).
45. M. Steiner *et al.*, *ChemPhysChem* **6**, 2190 (2005).
46. S. G. Lukishova and A. W. Schmid, "Near-Field Optical Microscopy of Cholesteric Oligomeric Liquid Crystal Layers," to be published in *Molecular Crystals and Liquid Crystals*.
47. S. G. Lukishova, A. W. Schmid, R. Knox, P. Freivald, R. W. Boyd, and C. R. Stroud, Jr., presented at Quantum Optics II, Cozumel, Mexico, 6–9 December 2004. For presentation see <http://speckle.inaoep.mx/QOII/ppts/Lukishova.pdf>.
48. S. G. Lukishova, A. W. Schmid, R. Knox, P. Freivald, R. W. Boyd, C. R. Stroud, Jr., and K. L. Marshall, in *Conference on Lasers and Electro-Optics/Quantum Electronics and Laser Science and Photonic Applications, Systems and Technologies 2005* (Optical Society of America, Washington, DC, 2005), Paper QTuE6.
49. S. G. Lukishova, A. W. Schmid, R. Knox, P. Freivald, R. W. Boyd, C. R. Stroud, Jr., and K. L. Marshall, presented at IQEC/CLEO 2005, Tokyo, Japan, 11–15 July 2005 (Paper JWH1-2).
50. H. M. P. Chen, D. Katsis, and S. H. Chen, *Chem. Mater.* **15**, 2534 (2003).
51. I. Chung, K. T. Shimizu, and M. G. Bawendi, *Proc. Natl. Acad. Sci. USA* **100**, 405 (2003).
52. B. C. Stevens and T. Ha, *J. Chem. Phys.* **120**, 3030 (2004).
53. D. Axelrod, *Biophys. J.* **26**, 557 (1979).
54. J. Y. Butter *et al.*, *ChemPhysChem* **7**, 261 (2006).
55. F. Vargas *et al.*, *J. Chem. Phys.* **117**, 866 (2002).
56. S. G. Lukishova, A. W. Schmid, R. P. Knox, P. Freivald, A. McNamara, R. W. Boyd, C. R. Stroud, Jr., and K. L. Marshall, "Single-Photon Source for Quantum Information Based on Single Dye Molecule Fluorescence in Liquid Crystal Host," to be published in *Molecular Crystals and Liquid Crystals*.
57. M. J. Escuti, J. Qi, and G. P. Crawford, *Opt. Lett.* **28**, 522 (2003).
58. W. Cao *et al.*, *Nature Materials* **1**, 111 (2002).
59. E. Yablonovitch, *Nature* **401**, 539 (1999).
60. T. Larsen *et al.*, *Opt. Express* **11**, 2589 (2003).

Fiber-Coupled Single-Photon Detectors Based on NbN Superconducting Nanostructures for Practical Quantum Cryptography and Photon-Correlation Studies

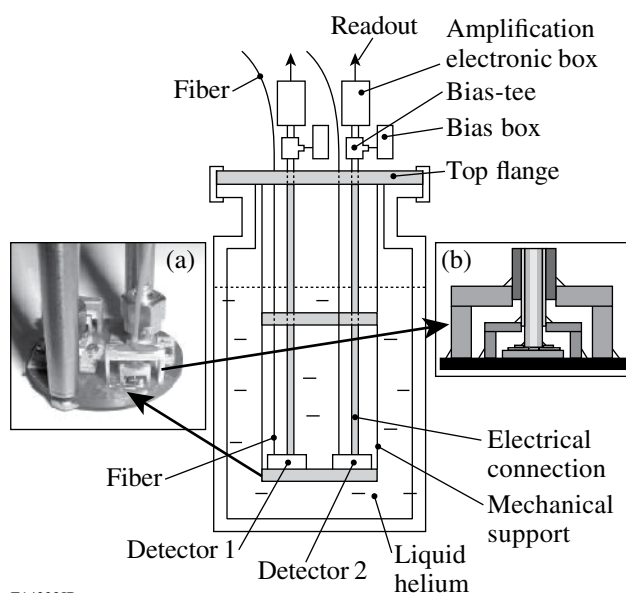
Practical quantum cryptography (QC) systems require ultrafast and high-quantum-efficiency (QE) single-photon detectors (SPD's)¹ with precise timing characteristics² and sufficiently low dark counts. For fiber-optic QC systems, SPD's working at the standard near-infrared (NIR) telecommunication wavelengths, namely 1.3 μm and/or 1.55 μm , with counting rates well above 10 MHz are required. In this wavelength range, the most popular InGaAs avalanche photodiodes have limited applicability because of their very large dark counts and significant afterpulsing.

We have already reported on our development of novel superconducting SPD's (SSPD's) based on nanostructured NbN superconducting meanders maintained at temperatures far below the NbN critical temperature T_c .³⁻⁵ The physics of the SSPD operation principle have been explained within a phenomenological, hot-spot formation photoresponse model.^{6,7}

The purpose of this article is to present the design and performance of a system of two integrated single-photon detectors based on two fiber-coupled SSPD's. Our two-channel system is designed for implementation in the telecommunication wavelength QC as well as for antibunching-type correlation studies of NIR photons emitted by quantum dots. Contrary to previous designs of fiber-coupled superconducting photon detectors, which required either room-temperature⁸ or cryogenic⁹ fiber positioning and adjustment, we developed a permanent optical-fiber coupling, which allows multiple thermal cycling of our detectors, robust performance, and room-temperature-like operation.

Figure 106.44 presents schematics of a complete cryogenic construction of our detectors. The insert is placed and sealed inside a standard liquid helium transport dewar. Two NbN SSPD's are glued on the bottom flange insert, as shown in Fig. 106.44(a), with the photon input and electrical output provided via a single- or multimode fiber and a semirigid coaxial cable, respectively. The SSPD nanostructures under study were fabricated according to a technological procedure described in detail in Ref. 10. We used 10- $\mu\text{m} \times 10\text{-}\mu\text{m}^2$ NbN superconducting meander-type structures with 4-nm-thick,

120-nm-wide stripes and a 0.6 filling factor (stripe width to stripe width plus separation ratio). The implemented devices were characterized by the critical current density of 2 to 6 MA/cm² at 4.2 K and $T_c \approx 10$ K.



E14323JR

Figure 106.44 Schematic of the two-channel, single-photon detector operating in a helium transport dewar. (a) Cryogenic end plate with two detectors pigtailed to fibers and the electrical output SMA connectors and cryogenic semirigid cables. (b) Cross section of the fiber detector's mechanical holding structure with a fiber positioning photoresist ring.

For accurate coupling between the SSPD and the fiber, we used a specially designed micromechanical photoresist ring placed directly over the SSPD. The 30- μm -thick coupling rings were fabricated using a photolithography process and positioned over the NbN meander with an accuracy of $\leq 1 \mu\text{m}$ using the meander's original alignment marks.¹¹ A cross section of the photoresist ring and the fiber attachment mechanical support (two bridge-like aluminum holders) is presented in Fig. 106.44(b). Outside the dewar, as indicated in Fig. 106.44, each electrical channel was connected through a broadband

(0.08 to 26 GHz) bias-tee to a constant-voltage biasing circuit and a two-stage amplifier with 62-dB total gain and 0.05- to 4-GHz bandwidth. Optical fibers were equipped with standard FC-type connectors. The transport dewar, filled with 60 liters of helium, allowed for over 2 months of uninterrupted operation of our detectors.

We have so far fabricated a total of ten detectors (five integrated pairs) of which eight were coupled with single-mode fibers and two with multimode fibers. The basic qualification of the detector performance was the measurement of the system QE (SQE)^{3,12,13} using highly attenuated, 40-ps-wide, 1540-nm-wavelength, 1-MHz repetition rate pulses from a semiconductor laser. The photon flux was precisely calibrated at the room-temperature fiber input (FC connector) and was the measure of the number of photons per optical pulse incident on the SSPD.

The detection probabilities (DP's) of several of our devices versus the number of photons per pulse delivered by the fiber to the NbN structure are presented in Fig. 106.45. The measurements were performed for the bias current $I_b = 0.95 I_C$, where I_C is the SSPD critical current at 4.2 K. The behavior observed

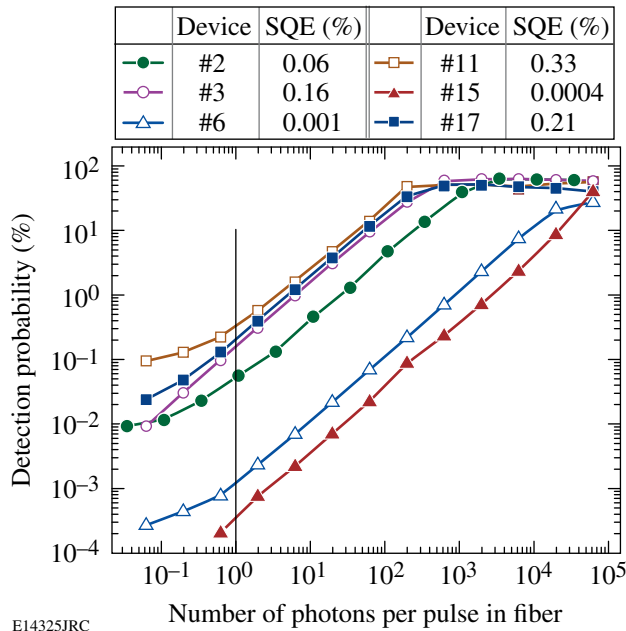


Figure 106.45
Photoreponse detection probability dependencies of the tested fiber-coupled NbN SSPD's on an average number of photons of the 1540-nm wavelength per pulse illuminating the detectors. For comparison purposes, the SQE value of the multimode fiber device #3 has been adjusted by taking into account the actual number of photons reaching the SSPD area. The thin vertical line indicates the 1 photon/pulse flux and corresponds to the SQE definition.

in Fig. 106.45 is in very good agreement with our previous observations.³⁻⁶ At low-incident photon fluxes, our experimental data show the linear DP dependence, demonstrating the single-photon detection mechanism.⁶ At high-light power levels, we observe DP saturation at the 100% level as virtually all laser pulses are counted. We define the SQE of our detectors by taking the DP value at the photon flux level corresponding to an average of one photon per pulse.

The SQE values for our best, average, and worst detectors are collected in Table 106.X with the device QE (DQE) values measured for the 1550-nm wavelength immediately after the SSPD fabrication. Taking the SQE/DQE ratio for each device, we have estimated and listed (see Table 106.X) the coupling factor K between the SSPD structure and the fiber. Simple calculations show (see Ref. 11) that the maximum $K \geq 0.9$ can be achieved when the fiber detectors' vertical separation is $< 20 \mu\text{m}$. However, K decreases rapidly with increasing horizontal misalignment and, for deviations $\geq 8 \mu\text{m}$ K , drops below 0.1. Table 106.X demonstrates that only device #11 exhibits a relatively large $K = 0.333$ factor while the "average" K is only 0.03, suggesting significant misalignment in the horizontal plane. Since the photoresist ring anchoring the fiber was positioned with $1\text{-}\mu\text{m}$ precision, we suspect that the observed low K values have their origin in an uncontrolled fiber tilting, resulting in an angled front surface of the fiber pigtailed to the detector. Thicker photoresist rings with tighter control of the inner circle diameter should significantly improve K .

Table 106.X: Device and system QE values for single-mode, 12- μm core diameter, fiber-coupled NbN SSPD detectors.

Detector #	DQE (%)	SQE (%)	Coupling factor K
11	1.0	0.33	0.333
2	2.1	0.06	0.029
17	6.4	0.21	0.033
6	2.0	0.001	0.0005
15	2.1	0.0004	0.0002

The reason for very low K values in devices #6 and #15 are apparently microcracks of the fiber core, which are likely to happen during the very first cooling cycle of the detector. The latter seems to be supported by the fact that in all our devices K remained unchanged after the initial one or two thermal cycles (300 K to 4.2 K and back) and the fatal detector failures were typically observed during/after the first cooldown. Postmortem mechanical inspection showed the fiber cracks in the damaged detectors.

The performance of detectors equipped with multimode (50- μm core diameter) fibers was not as good as expected (see, e.g., device #3 in Fig. 106.45) and the corresponding SQE and K values were rather low. The photon beam profile in the core of a multimode fiber has a Gaussian distribution; thus, even in case of optimum alignment, only $\sim 10\%$ of the power from the fiber reaches our 100 μm^2 SSPD. It is clear that larger area (e.g., $10 \times 20 \mu\text{m}^2$ or even $20 \times 20 \mu\text{m}^2$) SSPD's and fibers with reduced core diameters are needed to make the multimode fiber devices practical.

The dark count measurements performed on our detectors with the fiber room-temperature input blocked and biased at $I_b = 0.95 I_C$ resulted in 2 (device #6) to 90 (device #11) counts per second, clearly depending on the detector's K factor. The observed dark counts are significantly higher than that measured in our earlier free-space NbN detectors.³ The apparent reason is the 300-K thermal background radiation picked by the fiber's room-temperature end.

The SSPD's used to fabricate our fiber-coupled detectors were large-area meanders to maximize K . As recently documented,^{14,15} such structures exhibit large kinetic inductance, which limits their photoresponse temporal characteristics. In our time-domain measurements, we used 5-GHz-bandwidth, single-shot and 50-GHz-bandwidth, sampling oscilloscopes for capturing transient waveforms and for jitter studies, respectively. Figure 106.46 shows a photoresponse signal (dotted line) of one of our detectors. The measured transient is characterized

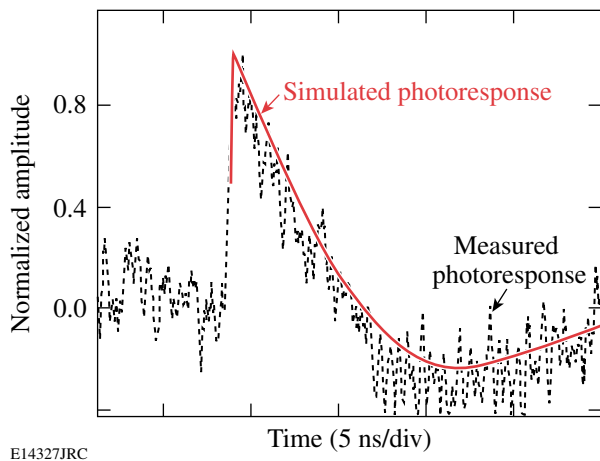


Figure 106.46 Time-resolved photoresponse of a fiber-coupled, 100- μm^2 area SSPD (dotted line) and the simulated signal (solid line) based on the calculated 420-nH value of the SSPD kinetic inductance and the 0.05- to 4-GHz bandwidth amplifier.

by a 250-ps rise time, 5-ns fall time, and a full width at half maximum (FWHM) equal to about 2.5 ns. We compared the measured pulse shape with numerical simulations (solid line) based on a model developed in Ref. 15 and confirmed that the kinetic inductance was responsible for a nanosecond-wide photoresponse of large-area SSPD's.

The experimental jitter profile (not shown) had a Gaussian shape and exhibited a FWHM of 35 to 37 ps for detectors with single-mode fibers. We note that the jitter measured in the fiber-coupled detectors is two times longer than the 18-ps value reported earlier for free-space-coupled SSPD's.³ The large kinetic inductance of the SSPD's may contribute to the jitter increase, although we believe that the excess jitter is due to such extrinsic elements as the laser-diode jitter and relatively long (>1 m) fiber and electrical cables.

Finally, we used our integrated, two-detector system in cross-correlation-type experiments. A train of 500-fs-wide (stretched by the fiber) pulses from a Ti:sapphire laser with a 940-nm wavelength and an 82-MHz repetition rate was split by a 50/50 beam splitter and directed simultaneously to the two detectors. Next, the signal from each detector was sent to a discriminator and fed to a start/stop-type correlator. The detector with a low SQE of 0.005% worked as a start device, while our best (#11) detector provided the stop signal. The resulting experimental second-order correlation function is shown in Fig. 106.47. The correlation signal is very clean and exhibits a FWHM of 390 ps, which can be regarded as the

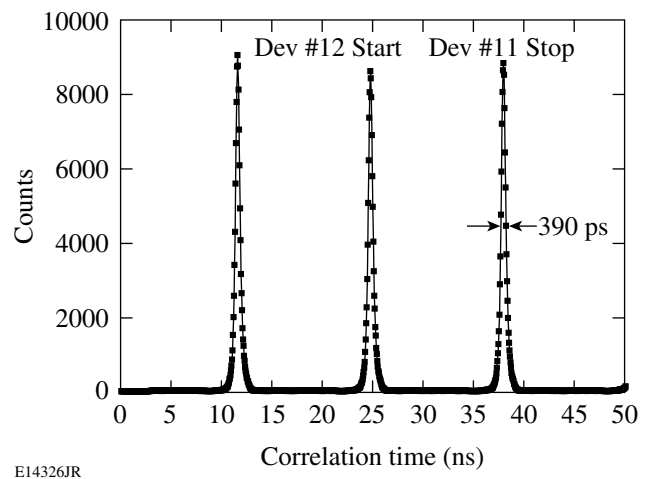


Figure 106.47 Experimental cross-correlation function of a pair of fiber-coupled detectors measured for 500-fs-wide incident optical pulses. The measured correlation FWHM is 390 ps.

figure of merit of the complete detection system (amplifiers, discriminator, correlator, cables, terminators, and detectors) since the incident optical pulses are negligibly short. We note that, despite a relatively long (few nanosecond in duration) response times of our detectors, the correlation pulses are sub-nanosecond. The latter, we believe, is due to the very low jitter and the short (250-ps) photoresponse rise time of the SSPD's and demonstrates the ability of our fiber-coupled detectors to successfully perform antibunching-type correlations observed in photons emitted by true single-photon sources such as single quantum dots.¹⁶

In conclusion, we have fabricated and tested fiber-based, single-photon detectors with a SQE of 0.3% at the 1550-nm telecommunication wavelength and fiber-coupling factor of up to 33%. The integrated two-detector arrangements can be placed inside a standard helium dewar and, from the operator's point of view, can be regarded as a room-temperature system. Our detectors are intended as practical devices for fiber-based QC systems since, despite their relatively low SQE, they are characterized by a counting rate above 200 MHz, jitter below 40 ps, and dark-count rates below 100 Hz. We have also demonstrated that the system cross-correlation time of two detectors counting femtosecond optical pulses is as low as 390 ps, making our fiber-coupled SSPD's very attractive for time-resolved, antibunching-type studies of single-photon sources. Our current research focuses on an improvement of the SQE and we expect to reach the 3% to 5% level because of the increase in DQE of our SSPD's and the achievement of reproducible K values of 30% or more. Very-large-area meander structures and devices coupled to quarter-wave resonators will be also implemented, especially in detectors with multimode fibers.

ACKNOWLEDGMENT

The authors would like to thank Dr. Marc Currie for his assistance in early time-resolved photoresponse measurements and Prof. Atac Imamoglu for his support. This work was supported by the Polish Ministry of Science under Project No. 3 T11B 052 26 (Warsaw), RFBR 03-02-17697 and INTAS 03-51-4145 grants (Moscow), CRDF grants RE2-2531-MO-03 (Moscow) and RE2-2529-MO-03 (Moscow and Rochester), and US AFOSR FA9550-04-1-0123 (Rochester). Additional support was provided by the MIT Lincoln Laboratory and BBN Technologies grants.

REFERENCES

1. J. C. Livas *et al.*, in *Free-Space Laser Communication Technologies VII*, edited by G. S. Mecherle (SPIE, Bellingham, WA, 1995), Vol. 2381, pp. 38–47.
2. C. Kurtsiefer *et al.*, in *Quantum Optics in Computing and Communications*, edited by S. Liu, G. Guo, H.-K. Lo, and N. Imoto (SPIE, Bellingham, WA, 2002), Vol. 4917, pp. 25–31.
3. A. Verevkin, A. Pearlman, W. Słysz, J. Zhang, M. Currie, A. Korneev, G. Chulkova, O. Okunev, P. Kouminov, K. Smirnov, B. Voronov, G. N. Gol'tsman, and R. Sobolewski, *J. Mod. Opt.* **51**, 1447 (2004).
4. A. Korneev, P. Kouminov, V. Matvienko, G. Chulkova, K. Smirnov, B. Voronov, G. N. Gol'tsman, M. Currie, W. Lo, K. Wilsher, J. Zhang, W. Słysz, A. Pearlman, A. Verevkin, and R. Sobolewski, *Appl. Phys. Lett.* **84**, 5338 (2004).
5. G. N. Gol'tsman, K. Smirnov, P. Kouminov, B. Voronov, N. Kaurova, V. Drakinsky, J. Zhang, A. Verevkin, and R. Sobolewski, *IEEE Trans. Appl. Supercond.* **13**, 192 (2003).
6. G. N. Gol'tsman, O. Okunev, G. Chulkova, A. Lipatov, A. Semenov, K. Smirnov, B. Voronov, A. Dzardanov, C. Williams, and R. Sobolewski, *Appl. Phys. Lett.* **79**, 705 (2001).
7. A. D. Semenov, G. N. Gol'tsman, and A. A. Korneev, *Physica C* **351**, 349 (2001).
8. A. J. Miller *et al.*, *Appl. Phys. Lett.* **83**, 791 (2003).
9. J. Zhang, N. Boiadjeva, G. Chulkova, H. Deslandes, G. N. Gol'tsman, A. Korneev, P. Kouminov, M. Leibowitz, W. Lo, R. Malinsky, O. Okunev, A. Pearlman, W. Słysz, K. Smirnov, C. Tsao, A. Verevkin, B. Voronov, K. Wilsher, and R. Sobolewski, *Electron. Lett.* **39**, 1086 (2003).
10. G. N. Gol'tsman, A. Korneev, I. Rubtsova, I. Milostnaya, G. Chulkova, O. Minaeva, K. Smirnov, B. Voronov, W. Słysz, A. Pearlman, A. Verevkin, and R. Sobolewski, *Phys. Stat. Sol. C* **2**, 1480 (2005).
11. P. Grabiec, W. Słysz, M. Węgrzecki, J. Bar, W. Milczarek, G. N. Gol'tsman, A. Verevkin, and R. Sobolewski, Poland Patent No. P-367391 (patent pending, 2004).
12. A. Verevkin, J. Zhang, R. Sobolewski, A. Lipatov, O. Okunev, G. Chulkova, A. Korneev, K. Smirnov, G. N. Gol'tsman, and A. Semenov, *Appl. Phys. Lett.* **80**, 4687 (2002).
13. W. Słysz, M. Węgrzecki, J. Bar, P. Grabiec, M. Górska, C. Latta, V. Zwiller, A. Pearlman, A. Cross, A. Korneev, P. Kouminov, K. Smirnov, B. Voronov, G. Gol'tsman, A. Verevkin, M. Currie, and R. Sobolewski, in *Infrared Photoelectronics*, edited by A. Rogalski, E. L. Dereniak, and F. F. Sizov (SPIE, Bellingham, WA, 2005), Vol. 5957, pp. 310–319.
14. R. H. Hadfield *et al.*, *Appl. Phys. Lett.* **87**, 203505 (2005).
15. A. J. Kerman *et al.*, *Appl. Phys. Lett.* **88**, 111116 (2006).
16. V. Zwiller *et al.*, *Appl. Phys. Lett.* **78**, 2476 (2001).

Transition Metal Dithiolenes Near-IR Dyes and Their Applications in Liquid Crystal Devices

Introduction

The development of an ideal series of dyes for liquid crystal (LC) device applications represents a formidable synthesis challenge for chemists. To be considered useful for applications in LC devices, the class of dyes under consideration must have (1) a high solubility in the host matrix; (2) good long-term chemical, thermal, and optical stability; (3) low impact on the LC order parameter; (4) a large molar absorptivity; (5) low electrical conductivity; (6) large dichroic ratio; and (7) a λ_{\max} located in the region of interest that can be tuned to some extent by relatively simple modifications in molecular structure. Dyes that possess all or nearly all of these properties are, for the most part, readily available for visible-region applications because of the large market for information display applications, which has provided

incentive for the synthesis of a large number of highly suitable compounds. In comparison, the total range of dyes that are suitable for applications in the near-IR region is limited to around ten chemical classes. The majority of these dyes were designed for laser applications such as *Q*-switching and are either ionic or highly polar in nature and, thus, only soluble in polar solvents (e.g., acetone and methanol). Their solubility in LC hosts is very poor (around 0.01 to 0.05 wt%), which limits their potential absorption efficiency in an LC device to an optical density (OD) of <0.1 for a 25- μm material path length. Table 106.XI compares the physicochemical properties, solubility, and absorption characteristics of the currently known classes of near-IR absorbing dyes. Only five dye classes are soluble in nonpolar solvents and thus could be expected to show reasonable solubility in an LC

Table 106.XI: The properties of near-IR dyes evaluated as potential guest–host dopants for LC devices.

Dye class	Species	λ_{\max} range (nm)	Solvents	Solubility in LC hosts (wt%)
Cyanine	Organic cationic	735 to 1100	Polar (acetone, methanol)	0.01 to 0.05 (<i>Q</i> -switch 5)
Azulenium	Organic cationic	728	Polar (acetone, methanol)	—
Pyrylium/ thiapyrylium	Organic cationic	748 to 879	Polar (acetone, methanol)	—
Iminium	Organic cationic	725 to 1090	Polar (acetone, methanol)	—
Squarilium/ croconium	Organic cationic	700 to 845	Polar (acetone, methanol)	—
Transition metal dithiolenes	Organometallic (zerovalent or anionic)	600 to 1600	Nonpolar (hexane, toluene)	10
Quinones/ anthraquinones	Organic zerovalent	748 to 810	Nonpolar (hexane, toluene)	2 to 3
Phthalocyanines	Organometallic zerovalent	630 to 830	Nonpolar (hexane, toluene)	—
Azo	Organic or organometallic zerovalent	700 to 900	Nonpolar (hexane, toluene)	2 to 3
Indoanilines	Organic zerovalent	660 to 800	Nonpolar (hexane, toluene)	—

host. Transition metal dithiolenes stand out as the most promising and interesting candidate of this group. They are highly soluble in nonpolar solvents (including LC hosts), their wavelength range spans from 600 nm in the visible to 1600 nm in the near IR (the latter wavelength is of special importance in military and telecommunications applications), and they possess excellent thermal and photochemical stability.

Interest in transition metal dithiolenes and their properties has been steadily increasing in recent years. They have been investigated as passive infrared absorbers for thermal imaging, photography, lithography, and electrophotography;¹ *Q*-switching-saturable absorbers for lasers,² optical limiters, and, in all-optical switching,^{3,4} “unimolecular metals” exhibiting metal-like conductivity down to 0.6 K;⁵ a “redox switch” for the binding and release of simple aliphatic olefins;⁶ and as guest–host dyes for LC electro-optic devices for near-IR applications.^{7,8} Earlier work by Muller–Westerhoff⁹ and Ohta¹⁰ established that these materials can possess numerous different stable LC phases depending on the structure of the terminal functional groups. This attribute was shown to be important for applications in LC guest–host systems since the presence of LC mesomorphism allows higher dye concentrations to be added to the LC host without substantially reducing its order parameter.^{7,8}

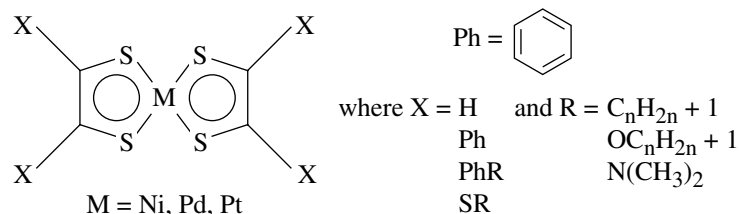
In this article we present an overview of the physical and optical properties of transition metal dithiolene complexes that make them of special interest for near-IR applications in LC devices and discuss in detail our past and present research efforts in the design, synthesis, and characterization of both nonchiral and enantiomerically enriched forms of these interesting series of materials. The latter compounds are of special interest for device applications because of their low melting points (below room temperature in many cases) and ability to induce chirality in a nematic LC host when added as a dye dopant. As such, they could provide two separate modes of tunability when introduced into a liquid crystal material: (1) an electronic absorption mode that is tunable by alteration of the molecular structure through synthesis and (2) a selective reflection mode that is tunable by composition (concentration of the chiral dye in the host), electric field, and temperature. Some specific application examples for transition

metal dithiolenes as near-IR dyes in LC electro-optical devices are also given. We conclude by presenting our most recent results that demonstrate the capability of computational chemistry to predict, prior to synthesis, both the near-IR electronic absorbance spectra and the helical twisting power (HTP) of transition metal dithiolenes as a function of molecular structure.

Properties of Transition Metal Dithiolenes

Transition metal dithiolene complexes^{11,12} in which the central metal is in a zerovalent state (oxidation number = 0) exhibit strong absorption bands in the 600- to 1600-nm region of the spectrum and are highly soluble in nonpolar organic solvents (e.g., toluene and hexane) as well as LC materials. The central metal can be any transition metal capable of forming square planar complexes, but complexes based on nickel, palladium, and platinum are the most common. Figure 106.48 shows the generic molecular structure of the transition metal dithiolene core.

The strong near-IR absorption maximum observed in transition metal dithiolenes is a function of both extensive electron delocalization about the dithiolene ring system and the interaction of this delocalized system with available *d*-orbitals on the central metal (Fig. 106.49).¹³ This interaction can be described using the linear combination of the atomic orbitals–molecular orbital (LCAO–MO) theory in which the atomic orbitals of the individual atoms are combined to form a series of lower-energy “bonding” and higher-energy “antibonding” molecular orbitals. The absorption of photons of sufficient energy results in the promotion of electrons from occupied (bonding) molecular orbitals to unoccupied (antibonding) molecular orbitals. The lowest-energy transition, and thus the one that occurs at the longest wavelength, is the transition between the highest occupied molecular orbital (HOMO) and the lowest unoccupied molecular orbital (LUMO) and is referred to as the “band gap.” This HOMO–LUMO transition is the one responsible for the strong near-IR absorption in the transition metal dithiolenes.^{11,13} A secondary electronic transition of weaker energy also occurs in the visible region between 500 and 600 nm in these materials. A change in the oxidation state of the metal eliminates the near-IR absorption, greatly strengthens absorption in the visible region, and renders the complexes soluble only in polar solvents. Substi-

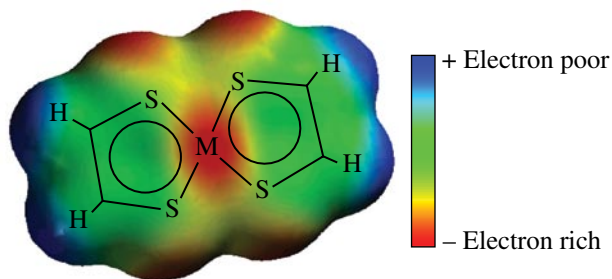


G4947aJR

Figure 106.48

The general molecular structure of transition metal dithiolenes. The physical properties of the complex are determined by the nature of the terminal functional groups, designated as X.

tution of the central metal with a different zerovalent transition metal also produces changes in the near-IR λ_{\max} . Platinum and palladium complexes show a 20- to 30-nm hypsochromic (blue) shift and bathochromic (red) shift, respectively, as compared to nickel complexes with the same ligand structure.



G4948aJRC

Figure 106.49

Ground-state charge distribution map of the nickel dithiolene core. The sulfur and nickel atoms are the most electron-rich areas in the molecule.

The nature of the functional groups attached to the metal dithiolene core has a large effect on both the position of the electronic absorption maximum and the solubility of the dye in the host matrix. Conventional wisdom teaches that the best way to shift the electronic absorption maximum to longer wavelengths is to maximize the extent of electron delocalization by utilizing aromatic ring structures with an extensive π -delocalization capability (phenyl, naphthyl, and anthracenyl) either as functional groups or incorporated within the central core of

the molecule. Although effective, this approach has the dual disadvantage of increasing the melting point of the complex while decreasing its solubility. Counterintuitively, we found that thioether groups bonded directly to the dithiolene core not only shift the near-IR absorption of the complex to longer wavelengths but also *enhance* their solubility in LC hosts. As a direct result of this finding, we focused our attention on preparing new transition metal dithiolene complexes based on thioether terminal groups. Because platinum dithiolene complexes absorb at shorter wavelengths and palladium complexes have proven to be very difficult to synthesize and isolate in a form pure enough for device applications, we continued to use nickel as the central metal of choice for these new materials.

Absorbance Dichroism

Transition metal dithiolenes are excellent candidates for near-IR guest–host devices because of their high molar absorptivity (>30,000), remarkable thermal and photochemical stability, and high solubility in LC hosts as compared to other near-IR dyes. Figure 106.50 (top) shows the field-induced dichroism of a mixture of 1% of the nematic liquid crystalline metal complex “BisBuSDNi” in the nematic LC K-15 measured in a 24- μm -thick, antiparallel-rubbed cell with (1) no field applied and (2) a 10-V, 100-KHz square wave applied to switch the cell into the homeotropic orientation. The drop in absorbance indicates positive dichroism; the contrast ratio at 860 nm is 5:1. An OD of 2.4 is easily achievable in the off state, and OD’s of 3.5 have been measured in similar cells at higher dye concentrations.⁷

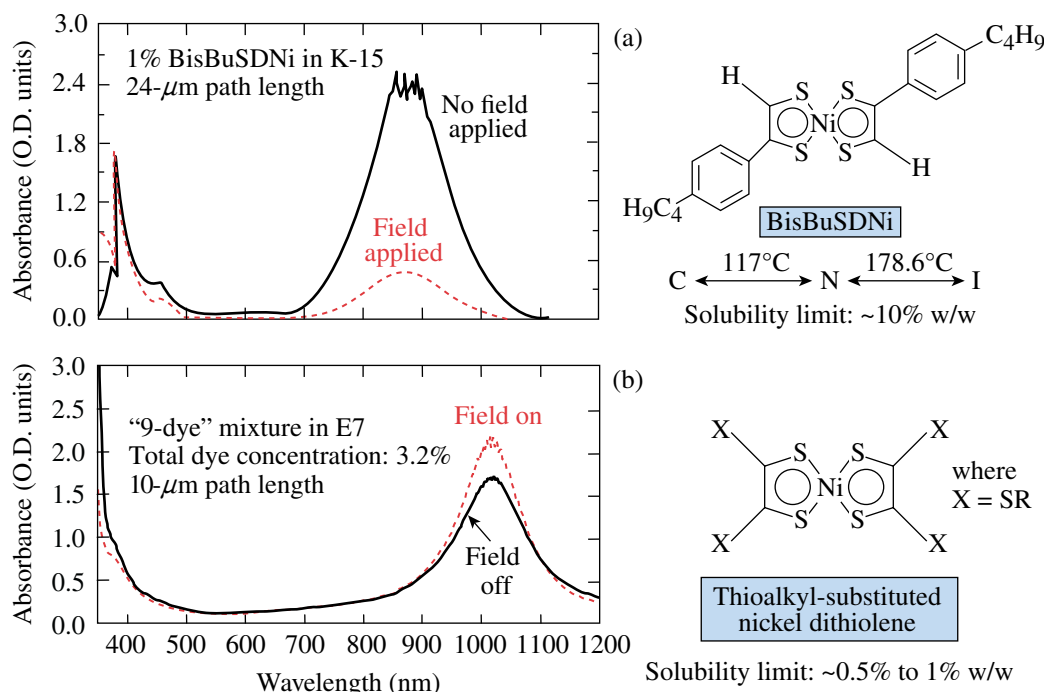


Figure 106.50

(a) Change in absorbance with applied voltage for a 1% concentration of “BisBuSDNi” in a 24- μm -thick, antiparallel-rubbed cell. An OD of 3.5 at 860 nm is achievable at higher dye concentrations. (b) Field-induced dichroic behavior of a mixture of nine thioalkyl-substituted nickel dithiolene dyes in Merck E7. Increasing the number of terminal substituents from two to four and altering their structure changes the sign of the dichroism from positive to negative.

G5972aJRC

Changes in molecular structure can cause substantial changes in both the position of the dye λ_{\max} and the nature of the field-induced dichroism. Figure 106.50 (bottom) shows the field-induced behavior of a mixture of nine thioalkyl-substituted nickel dithiolenes in Merck E7. The total dye concentration was 3.2%, and the cell path length was 10 μm . This new series of dyes shows a small degree of *negative* dichroism, whereas the materials synthesized previously showed only *positive* dichroism.

Solubility in an LC Host

Solubility testing of thioalkyl-substituted nickel dithiolenes in the LC host E7 (Merck) was conducted at selected concentrations between 0.3 wt% to 1 wt% along with several phenyl-substituted nickel dithiolenes as reference compounds. Each dye was dissolved into 2 ml of the host by heating the host/dye mixture to 100°C with stirring for several hours. Upon cooling, each sample was filtered through a 0.45- μm Teflon membrane filter to remove any insoluble material. All samples were checked daily, both visually and by microscopic inspection at 100 \times magnification, for evidence of dye precipitation. For samples that showed precipitation, new mixtures were prepared at lower concentrations until a stable dye concentration was achieved.

Computational chemistry methods were employed in a parallel and complementary effort to aid in predicting the appropriate functional group combinations that would yield materials with the desired solubility and spectroscopic parameters.¹⁴ Because limitations in the computational methods precluded solubility calculations in either anisotropic solvents or solvent systems composed of mixtures of compounds, Merck CB-15,

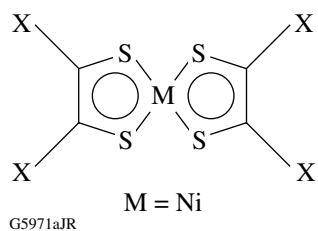
an isotropic chiral cyanobiphenyl compound, was used to establish *qualitative* solubility trends.

The solubility of a given solute in a solvent can be approximated by calculating its solvation energy and comparing this value with the bonding, or “reorganization,” energy. The solvation energy ΔG_{solv} is defined as¹⁵

$$\Delta G_{\text{solv}} = \Delta G_{\text{elec}} + \Delta G_{\text{cov}} + \Delta G_{\text{disp}} + \Delta G_{\text{vib}} + \Delta G_{\text{lib}} + \Delta G_{\text{other}} \quad (1)$$

where ΔG_{solv} is the solvation energy, ΔG_{elec} is the electrostatic solute–solvent interaction, ΔG_{cov} is the energy to form a solute-shaped cavity, ΔG_{disp} is the London and van der Waals interactions, ΔG_{vib} is the change in vibrational energy due to damping, ΔG_{lib} is the conversion of rotations and translations to librations, and ΔG_{other} is the solvent enthalpic and entropic structure (PV term, etc.). The value ΔG_{solv} can be used as a qualitative indicator of general solubility of the dye solutes in the same host with a larger positive value generally indicating a greater solubility in the solvent host matrix. Table 106.XII gives a compilation of melting points, near-IR absorbance, and solubility (calculated versus experimental results) for a series of substituted nickel dithiolenes complexes with substituted phenyl and alkylthio terminal groups. General trends that can be drawn from the data in Table 106.XII are, that as the terminal groups are changed from substituted phenyl to alkylthio, (1) the melting points of the complexes drop drastically, (2) the near-IR λ_{\max} of the complexes are shifted substantially to longer wavelengths,

Table 106.XII: Comparison of melting points, near-IR absorbance maxima, and solubility data (both calculated and experimental) for a series of phenyl-substituted and alkylthio-substituted nickel dithiolenes in Merck CB-15 and E7 hosts. A larger *positive* value for ΔG_{solv} indicates higher solubility.



Terminal (X) group	Melting point (°C)	λ_{\max} in E7 (nm)	CB-15		Merck E7
			Solubility limit (wt%)	ΔG_{solv}	Solubility limit (wt%)
–SC ₈ H ₁₇	73	1020	1.0	–7.6725	0.50
–SC ₇ H ₁₅	81.5	1020	0.5 to 1.0	–7.7164	0.50
–SC ₄ H ₉	101	1020	0.5 to 1.0	–7.7190	0.50
–PhC ₄ H ₉	228 to 230	910	0.3 to 0.5	–14.4373	0.50
–PhN(CH ₃) ₂	280 to 283	1056	0.3 to 0.5	–17.4080	0.05
–PhOC ₉ H ₁₉	184 to 189	970	0.1 to 0.3	–21.6724	0.30
–PhOC ₄ H ₉	246 to 248	970	0.1 to 0.3	–21.6950	0.30

and (3) the solubility of the complexes in both CB-15 and E7 (both calculated and experimental) increases.

Materials Synthesis

The synthesis of nickel dithiolenes and their precursor ligands was conducted using modifications of literature methods and have been reported elsewhere. Three basic methods have been employed, depending on the degree of substitution desired in the complex and its overall symmetry. Mesogenic nickel dithiolenes were synthesized by a

modification⁷ of an earlier three-step procedure reported by Mueller–Westerhoff *et al.*,^{9,11} as shown in Fig. 106.51. Although relatively simple, this method has some disadvantages in that the products are difficult to separate from the tarry by-products formed from phosphorous pentasulfide and, as a result, the yield of purified product is very low (5% to 15%). A second method that is useful for the preparation of alkylthio-substituted nickel dithiolenes is based on literature methods reported by Wainwright and Underhill,¹⁶ N. Svenstrup *et al.*,¹⁷ and A. Charlton *et al.*,¹⁸ as shown in Fig. 106.52. The method

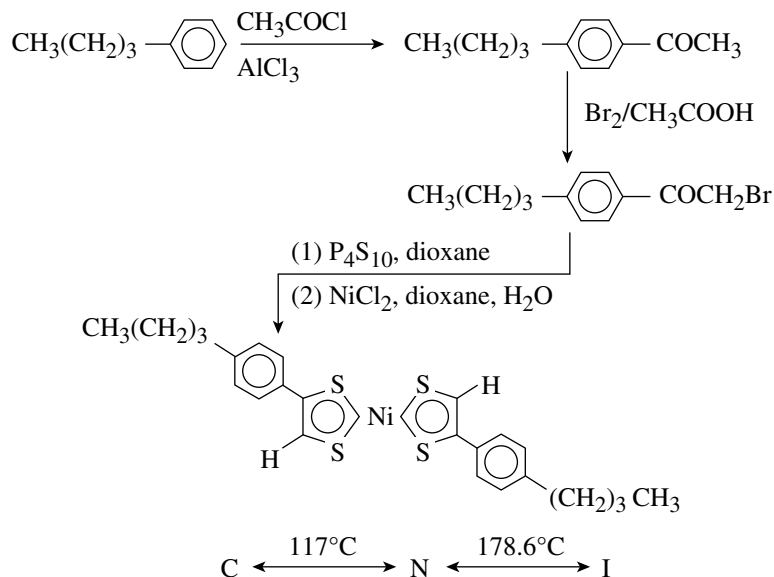


Figure 106.51

The synthesis method for rod-like nickel dithiolenes compounds possessing a liquid crystal phase.

G6947JR

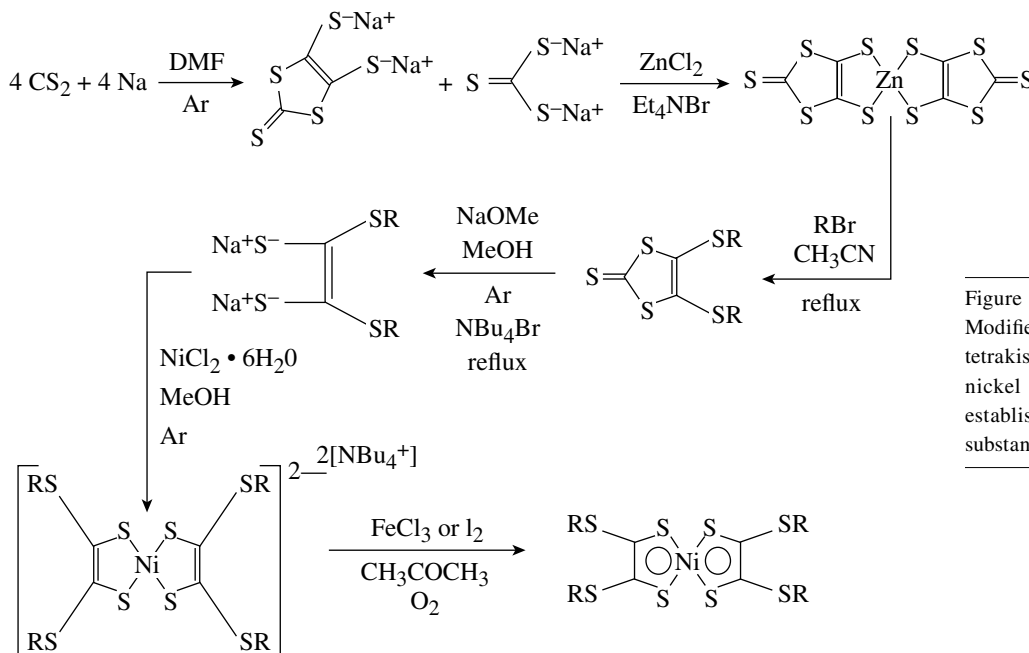


Figure 106.52

Modified synthesis scheme for preparation of tetrakis(alkylthio) bis(ethylene-1,2-dithiolenes) nickel(0) complexes. Modifications to the established literature procedures resulted in substantially improved yields of product.

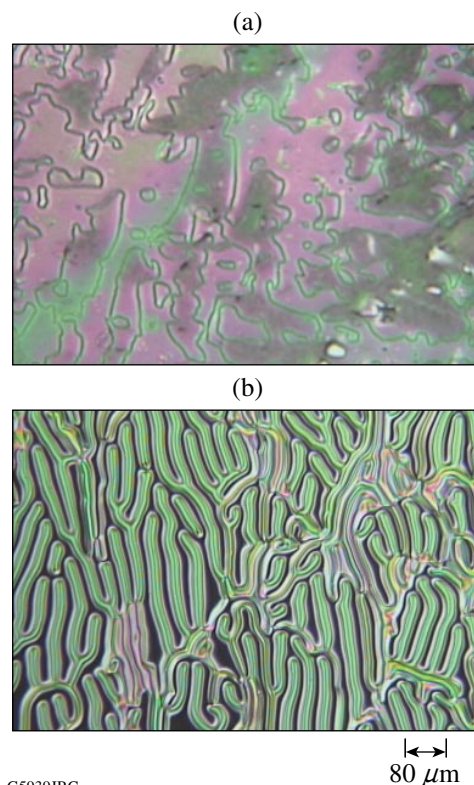
G4954JR

is applicable to both chiral and nonchiral terminal groups. For nonchiral terminal groups, yields of the complexes ranged from 27% to 68%, while yields of complexes with bulkier, enantiomerically enriched terminal groups were substantially lower (5%–10%). A third method allows the insertion of a flexible alkyl spacer ranging from 2 to 9 carbons between the thio group attached to the dithiolenene core and an enantiomerically enriched chiral terminal group based on nonracemic carboxylic acids or alcohols, as shown in Fig. 106.53. The large, flexible, and bulky terminal groups make them somewhat difficult to isolate and purify. Currently, the overall yields for these materials are quite low, ranging from a few percent up to around 15% for materials with shorter alkyl spacer groups.

Enantiomerically Enriched Nickel Dithiolenene Complexes

Table 106.XIII gives the generic structure and physical properties, respectively, of these nickel dithiolenene complexes with enantiomerically enriched terminal groups. The most remarkable feature of this series of chiral materials is how rapidly and dramatically their melting points decrease as the length and breadth of the terminal groups increase. With the exception of the *S*-(+)-2-methylbutylthioether derivative, all of the other materials are liquids at room temperature.

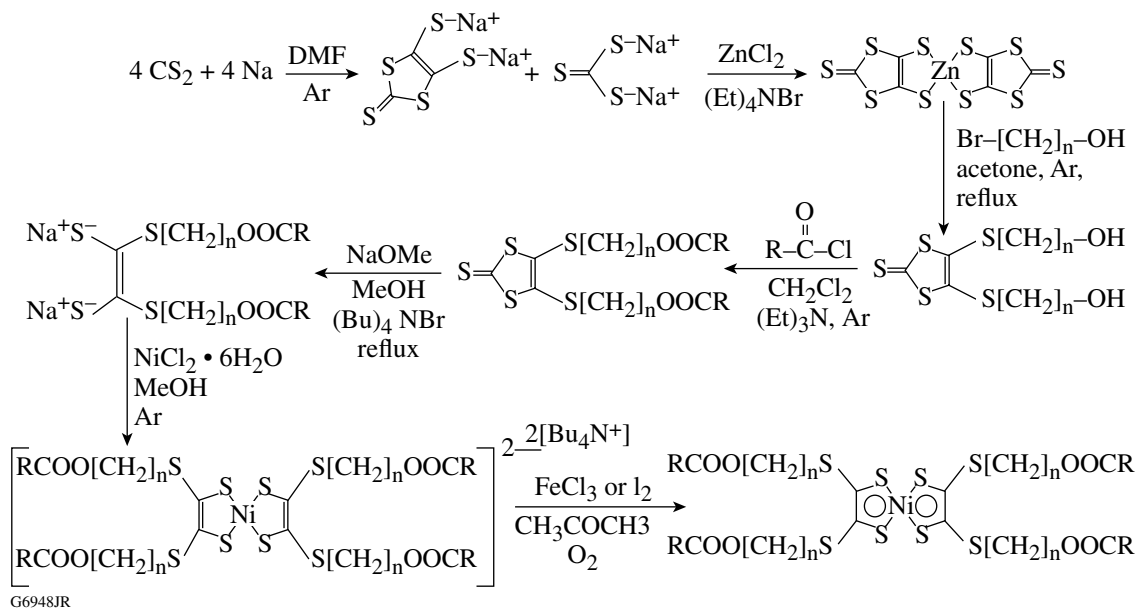
Another interesting attribute of these new chiral metal dithiolenenes is that they are capable of inducing a chiral nematic phase when added to a nematic LC host. Figure 106.54 shows



G5939JRC

 80 μm

Figure 106.54
Chirality transfer to an LC host by doping with a chiral nickel dithiolenene complex. (a) Pure Merck E7 and (b) Merck E7 containing 0.5% of the *S*-(+)-2-methylbutylthioether-substituted nickel dithiolenene.



G6948JR

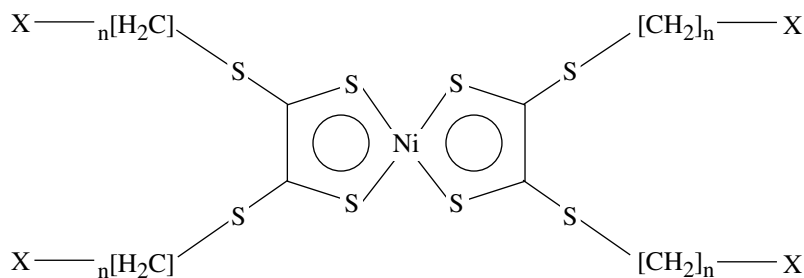
Figure 106.53
Synthesis scheme for chiral transition metal dithiolenenes incorporating a flexible spacer between the terminal groups and the dithiolenene core.

photomicrographs under crossed polarizers of a sample of Merck E7 before and after doping with 0.5% of the S-(+)-2-methylbutylthioether-substituted nickel dithiolenes. The fingerprint texture generated in the doped sample (helical pitch, length = 80 μm) is clear evidence that the chirality of the metal complex has been transferred to the LC host.

Device Applications

Transition metal dithiolenes have many possible commercial, military, and scientific applications in LC electro-optical devices for the near-IR region. Their high solubility in LC hosts, capability of exhibiting mesomorphism, excellent thermal and photochemical stability, dichroic capability, and broad wavelength range have

Table 106.XIII: Physical properties of the new chiral nickel dithiolenes complexes.

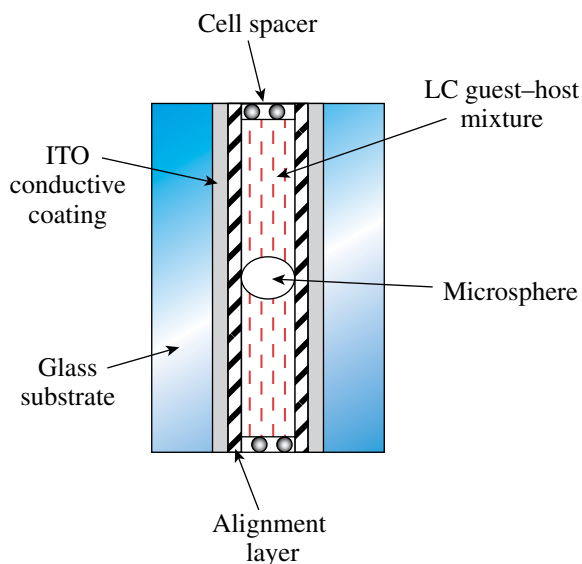


X group	Spacer (n)	MP (°C)	λ_{max} (nm) (a) E7 (b) Toluene	Helical pitch length (E7, μm)
	0	108.5	1020 ^a	80
	0	-43	1020 ^a	30
	3	-45	1009 ^b	
	6	-50	1009 ^b	
	9	-49	1009 ^b	
	3	<25	1008 ^b	
	6	-46	1008 ^b	
	9	-46	1008 ^b	
	3	-52	1005 ^b	
	6	-45	1005 ^b	
	9	-46	1010 ^b	
	3	<25	1011 ^b	
	6	-52	1011 ^b	
	9	<25	1011 ^b	

G5973JR

made them of interest for use in LC devices for near-IR optical modulation, switching, nonlinear optics, and sensor protection.¹⁴ In addition to these applications, nonchiral nickel dithiolenes have been extensively investigated as a component of the liquid crystal point diffraction interferometer (LCPDI), a phase-shifting, common-beam-path interferometer that uses an LC electro-optic device as the modulation element.^{19,20} Because both the object and reference beams follow the same path, the LCPDI is relatively insensitive to the mechanical vibrations, temperature fluctuations, and air turbulence that plague conventional phase-shifting interferometers. The LC host used in the LCPDI must be doped with a dye to compensate for differences in the cross sectional area of the sample and reference beams to ensure good fringe contrast (Fig. 106.55). Ideally, the dye should have as low a dichroism as possible to maintain constant interference fringe contrast with applied voltage. The LCPDI is being investigated as a beamline diagnostic for the 60-beam, 40-TW, 1054-nm OMEGA Laser System used in the Department of Energy's inertial confinement fusion research at the Laboratory for Laser Energetics. The large physical size and the need for vibration isolation make conventional near-IR phase-shifting interferometers impractical for these characterization activities since each of the 60 beams would have to be propagated a long distance across free space to reach the interferometer table. To date, transition metal dithiolenes are the only class of near-IR dyes that have the necessary combination of physical properties suitable for a near-IR LCPDI device.

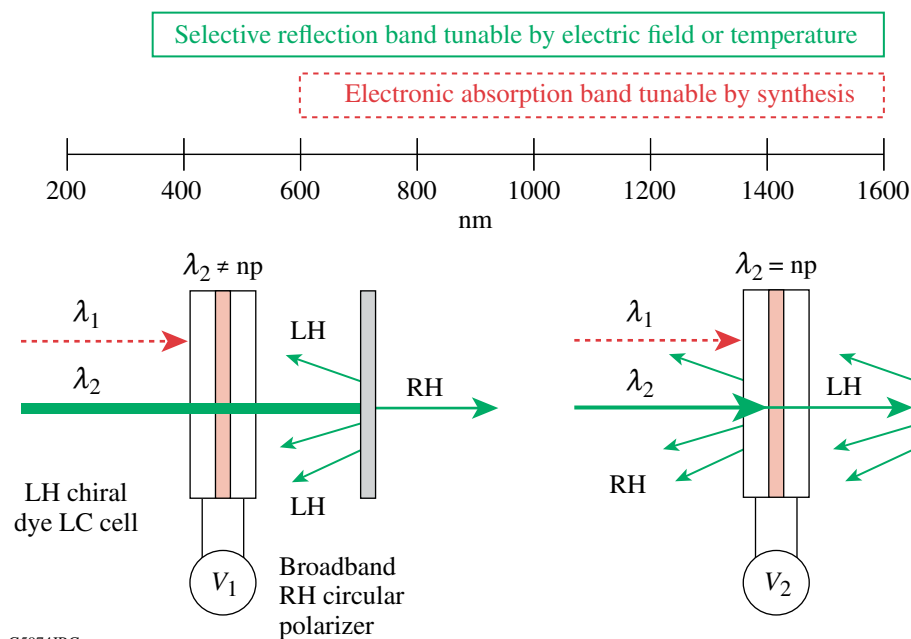
The addition of chirality to the dithiolene core now opens new application possibilities. Since these new materials are non-



G6607JRC

Figure 106.55
A schematic representation of the liquid crystal point diffraction interferometer (LCPDI) device.

centrosymmetric, they may exhibit interesting nonlinear optical properties, either on their own in the liquid state or as a dopant in a suitable host. The demonstrated induction of chirality in nematic phases by doping with a chiral nickel dithiolene suggests the possibility of devices for sensor protection in the near IR that have two modes of tunability: one mode through the absorbance of the nickel dithiolene dye (tunable by synthesis) and a second tunable mode employing selective reflection wavelength shifting induced by electric field or temperature changes (see i.e., Fig. 106.56).



G5974JRC

Figure 106.56
Device concept for sensor protection in the near IR based on chiral nickel dithiolene dyes. The device has two modes of tunability: one mode through the absorbance of the nickel dithiolene dye (tunable by synthesis) and a second tunable mode employing selective reflection wavelength shifting induced by electric field or temperature changes. Selective reflection occurs when the incident wavelength λ equals the product of the average refractive index of the LC material and its pitch length P .

Computational Chemistry Modeling of Nickel Dithiolene Systems

Advances in the science of computational chemistry over the past 20 years, the widespread availability and increasing ease of use of computational chemistry software, and an exponential reduction in the cost and size of extremely powerful computer hardware now make some degree of computational predictive capability for physical properties (e.g., solubility, electronic and vibrational spectra, reactivity, molecular configuration, and chirality) within the reach of nearly every laboratory that is involved in new materials research and development. Previously and out of necessity, researchers would have to follow an empirical approach of synthesizing, isolating, characterizing, and purifying hundreds of different compounds to establish structure–property relationships that could be used to further direct the design and development effort toward the desired goal. Of these hundreds of compounds synthesized, only a handful would have the necessary combination of physical characteristics to be deemed worthy of further study and development. Such a process is not only time consuming, labor intensive (weeks to months to completely synthesize and characterize each compound), and costly, but can also be highly frustrating for organic chemists engaged in the synthesis of new materials—especially for those with limited resources. Modern hardware and user-friendly software now make it possible to model new compounds and their physical properties with remarkable accuracy within a few hours or days, which only a few years ago would have taken from weeks to months of work to achieve the same results.

Nowhere has there been more evidence of the predictive capability of computational chemistry than in the pharmaceutical industry, where computational molecular design techniques have been used to great advantage for a number of years in the rapid development of new drugs with enhanced biological activity and specificity at lower cost. More recently, computational chemical methods have been applied to the molecular engineering and design of liquid crystal materials for use both in the multibillion dollar information display industry and the optoelectronic, photonics, military, and life sciences sectors. In all of these examples, the vast majority of the target materials systems consist of *organic molecules* composed mainly of carbon, hydrogen, and nitrogen in combination with a few other elements (e.g., sulfur, fluorine, and phosphorous). The state of the art in computational chemistry modeling in these materials is well developed, and computational algorithms and procedures are well defined in a large body of existing literature. The application of computational chemistry techniques to transition metal organometallics and particularly the transition

metal dithiolenes, represents a substantial challenge mainly for several reasons that include (1) the lack of previous research activity in the area from which to draw direction from, (2) the extremely small number of parameter files (basis sets) that can adequately account for the unique nature of the coordinate-covalent bonds that are formed in these materials, (3) the intensive computational resources required to accomplish the calculations, and (4) the scarcity of computational chemistry software capable of modeling organometallic systems. In what follows, we describe the computational modeling methodology that we have developed and applied to nickel dithiolene systems to predict, prior to synthesis, properties that include (a) the near-IR electronic absorbance spectra and (b) the helical twisting power (HTP) of the nickel dithiolene complex in a host medium for enantiomerically enriched materials. This effort is believed to be the first time that such calculations of this nature have been attempted in nickel dithiolene systems or in any other transition metal organometallic complex.

1. Modeling of Electronic Transitions States and Near-IR Absorbance Spectra

The process of modeling electronic absorbance spectra is composed of three key steps.

- *The free energy of the molecular structure with respect to its conformation is minimized.*

Molecular mechanics calculations employing Newtonian mechanics and empirical force fields are used to generate a particular molecular conformation that represents an energy-minimized state with respect to bond angles, electrostatic repulsions, and steric factors. This energy-minimized structure represents an approximate equilibrium conformation that must be further refined using quantum mechanical methods.

- *The electron distribution in the molecule is determined, and the available electronic energy levels and excited states are calculated.*

Either semiempirical or *ab initio* quantum mechanical methods can be used for this task. Semiempirical methods use some approximations and are employed when a certain degree of computational accuracy can be sacrificed in exchange for reduced computational resources and run time. *Ab initio* methods provide a much more detailed and accurate description of the quantum mechanical aspects of a molecular structure but do so at a cost of increased computational resource requirements and time. The substantially improved accuracy of *ab initio* calculations made them the preferred method for modeling the

exceedingly complex electronic distribution and excited-state transitions found in nickel dithiolenes.

Ab initio calculations are based on a detailed description of the quantum mechanical aspects of a molecular structure using the Schrödinger equation, defined as

$$H_{\text{op}} \Psi = E\Psi, \quad (2)$$

where H_{op} is defined as the Hamiltonian operator, Ψ as the wave function of the system, and E as the energy of the system. The Hamiltonian of the system represents its kinetic and potential energy. In a three-dimensional system, the Hamiltonian operator is defined as

$$H_{\text{op}} \Psi = \frac{-h^2}{2m} \left(\frac{\partial^2 \Psi}{\partial x^2} + \frac{\partial^2 \Psi}{\partial y^2} + \frac{\partial^2 \Psi}{\partial z^2} \right) + U\Psi, \quad (3)$$

where h is Planck's constant divided by 2π and m is the mass of an electron. The terms x , y , and z are the Cartesian coordinates of an electron with respect to the nucleus, while U refers to the potential energy of the system.²¹

A wave function is a mathematical expression that describes the wave nature of an electron after certain restrictions are placed on it by basis sets, which give specific information on the electronic structure and orbitals of the atoms as well as describing the path and behavior of electrons. The wave function expression is a group of Gaussian-type orbital equations for which the generic equation is

$$\Psi = Nx^l y^m z^n e^{-\alpha r^2}, \quad (4)$$

where x , y , and z are the Cartesian coordinates; l , m , and n are positive integer values that describe the angular momentum of the orbital, r is the distance to the center of the atom, N is the normalization constant, and α represents the orbital exponent of the Gaussian function.

Because the Schrödinger equation cannot be solved directly for a many-electron system, various approximation methods can be used to make it solvable. The Hartree–Fock method uses three approximations to estimate the many-electron wave function; these include (1) the *Born–Oppenheimer approximation* (assumes that all nuclei are motionless with respect to the electron), (2) the *linear combination of atomic orbitals (LCAO) approximation* (assumes that electron orbitals may be expressed as one-electron basis functions centered on each atom), and

(3) the *Hartree–Fock approximation* (which assumes that the sum of all single-electron calculations of a molecule is the same as the multi-electron calculation of the molecule). Because of inaccuracies associated with the Hartree–Fock approximation, the entire Hartree–Fock computational method becomes less accurate with increasing molecular size.²²

Unlike the Hartree–Fock method, which uses an exact Hamiltonian with approximate wave functions written in terms of a product of one-electron functions, the density function theory (DFT) method replaces the many-electron wave function with electronic density as the basic quantity.²³ The DFT method is widely employed in the field of computational chemistry and is considered to be a good method to use with transition metal complexes.

- *Calculation of the allowable ground-state to excited-state transitions that are responsible for the electronic absorbance spectrum.*

The expected excited-state electronic transitions are determined by including the configuration interaction (CI) model in the *ab initio* quantum mechanical calculations. The CI model is derived from Hartree–Fock calculations that are expanded to incorporate electronic excitation and changing shell levels.

Because there was no single software package capable of handling all of the computational tasks, a total of four separate software packages running on two different computing platforms were required. Molecular mechanics computations were conducted using Spartan 4 (Wavefunction, Inc.) on a 2-GHz, dual-processor Intel XEON server. *Ab initio* and electronic spectra calculations were conducted using the open-source computational package GAMESS (General Atomic and Molecular Electronic Structure System) from Iowa State University on a SGI Altix Server using sixteen 2.5-GHz Itanium 2 processors. Input-to-output file format conversions from Spartan to GAMESS were accomplished using Open Babel (www.sourceforge.net), while the final spectral output from GAMESS was processed, displayed, and plotted using the WebMO graphical user interface (<http://webmo.net/index.html>).

Specifying the appropriate conditions to conduct the *ab initio* calculations using GAMESS proved to be extremely challenging. Parameter options and appropriate basis sets for the calculations must be selected and specified properly to achieve valid results. For relatively small organic molecules there is existing literature to guide the selection of appropriate options and parameter sets, but in the case of nickel dithiolenes

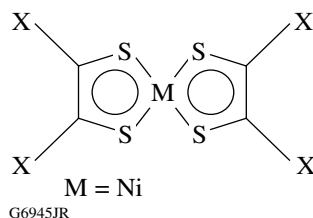
there is no pre-existing body of literature from which to draw guidance. The proper calculation conditions were determined through a combination of (1) an extensive study of the general literature on *ab initio* molecular modeling theory, (2) review of the handful of existing references on *ab initio* modeling in unrelated transition metals and their complexes, and (3) testing the selected modeling parameters and conditions by means of an iterative trial and error process. The calculation options that were ultimately selected and used in testing the model and its application to new nickel dithiolene systems are

- **SCFTYP** (*self-consistent field wave function*): Specifies the basic calculation type that is used. For our work, the restricted Hartree–Fock²⁴ (RHF) and density functional theory²⁵ (DFT) options were used. The RHF method was ultimately chosen for the final calculations because (1) it was found to be more accurate than the DFT method in initial test trials, and (2) since the CI calculations required to calculate the absorbance spectra are based on the RHF calculations, they cannot be run concurrently with the DFT option.
- **CITYP** (*configuration interaction model type*): Includes and specifies CI models in the *ab initio* calculations for electronic spectra calculations.
- **BASIS and GBASIS**: Specifies the type of basis set used for the calculation and what type of basis set function to choose, respectively. The minimal basis sets (GBASIS = STO) and split-valence basis sets (GBASIS = N31) were chosen initially because they were one of the few basis sets that were capable of producing accurate calculations for the electronic structure of nickel dithiolenes. The minimal basis set used was STO-3G (Refs. 26 and 27) with three Gaussian functions. Split-valence basis sets used were 6-31G with six Gaussian functions, and 6-31G(d) (Ref. 28) with both six Gaussian functions and functions that included *d*-orbital calculations. The split-valence basis sets proved to be more accurate because they correctly predicted that valence electrons do most of the bonding. The 6-31G(d) basis set specifies the inclusion of *d*-orbitals in the calculations, thus increasing their accuracy.
- **SCF and DIRSCF**: Specifies whether the self-consistent field wave function will be calculated directly or indirectly.²⁹ Hartree–Fock calculations make use of a large number of two-electron repulsion integrals that are stored and retrieved from hard disk storage. The direct SCF calculation re-evaluates the integrals directly without storing to disk during each Hartree–Fock iteration, which dramatically speeds up processing time.

- **CIS and NSTATE**: Specifies the method for determining the electronic structure³⁰ and how many different peaks in the electronic spectrum should be selected for the calculations, respectively. The optimal value for NSTATE was 10, as lower values would generate inaccurate results while higher values would significantly increase calculation times without any significant gain in accuracy.
- **DAMP**: Aids in allowing the system to converge to an energy minimum state during SCF calculations.^{31,32} *Ab initio* calculations were found to fail consistently in nickel dithiolene systems unless this option was added.

The accuracy of the computational method was tested by modeling a series of nickel dithiolenes reported previously in the literature by Mueller–Westerhoff *et al.*,¹³ calculating the expected near-IR absorbance spectrum and comparing the resultant values to the literature data in several different solvents (Table 106.XIV). A Pearson correlation *r* (a measure of the fit of a least squares linear regression through the data set) between the calculated and experimental near-IR absorbance data was determined for the compounds in Table 106.XIV. The correlation coefficient *R*² describes the proportion of the points that can be accounted for by the linear regression. For the near-IR absorbance data in Table 106.XIV, a correlation coefficient

Table 106.XIV: Calculated and experimental near-IR peak absorbance data for a series of nickel dithiolene compounds previously prepared and reported in the literature.



Terminal group	Experimental solvent	Experimental wavelength (nm)	Calculated wavelength (nm)
X = H	Hexane	720	720.91
X = CH ₃	CHCl ₃	774	843.08
X = CF ₃	Pentane	715	775.05
X = S-C ₄ H ₉	CHCl ₃	1104	1012.31
X = C ₆ H ₅	CHCl ₃	866	845.19
X = 2-naphthyl	CHCl ₃	905	993.08
X ₁ , X ₄ = H X ₂ , X ₃ = C ₆ H ₅	CH ₂ Cl ₂	805	857.78

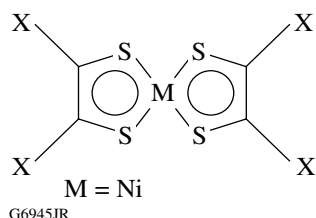
of 0.910117443 was obtained, which represents an excellent correlation between calculated and experimental results for a majority of the compounds modeled, considering that the theoretical model assumes that the molecule is not solvated (i.e., in a vacuum). The excellent correlation is strong evidence of the predictive capability of the computational method and validates its use in predicting electronic transition states in nickel dithiolene systems that have yet to be synthesized.

Table 106.XV shows the results obtained when the new computational method was applied to a series of yet-to-be synthesized nickel dithiolene systems with ligands of varying structure. The goal of this exercise was to be able to establish structure–property relationships that could be used in the design of new materials with an advantageous combination of physical and optical properties (high host solubility, large absorbance oscillator strength, and control of the peak absorbance maximum) through ligand selection. One nickel dithiolene complex with C₆ alkyl terminal groups that has been previously prepared is also included in the table as a reference. One significant trend that can be observed on examination of the table is that the near-IR peak wavelength is red-shifted when

sulfur-containing groups are bonded directly to the dithiolene core, whereas for phenyl groups the near-IR maximum is blue-shifted. This observed trend is somewhat counterintuitive as it is normally accepted that the addition of aromatic groups in conjugation with another aromatic structure generally shifts the absorbance maximum of the molecule to *longer* wavelengths than do alkoxy or thioalkyl groups because of resonance stabilization (the energy gap between electron levels is reduced, thus allowing electronic-state transitions to occur at a lower energy and longer wavelengths). Clearly, the *d*-orbitals on the sulfur-containing terminal groups are providing a greater degree of resonance stabilization in this case than the phenyl groups. The nature of this stabilization is not yet understood and will be investigated in the future.

A serious limitation of the current modeling method is that GAMESS appears to be unable to produce accurate electronic spectral data for nitrogen-containing compounds. Computational failures were routinely encountered in every attempt to model nitrogen-containing nickel dithiolene structures. The same results were obtained in attempts to model even very simple, classical nitrogen-containing organic compounds. The source of the problem at this point is still unresolved, but it appears to be a basic functional issue with GAMESS itself and not with our specific computational methodology or parameter files. An investigation of this issue is ongoing.

Table 106.XV: Predicted electronic spectral maxima for a series of candidate nickel dithiolene compounds that have yet to be synthesized. The first entry in the table is a compound that has been synthesized and included for reference.



Terminal groups	Experimental wavelength (nm)	Predicted wavelength (nm)
X = C ₆ H ₅	866	845.19
X = S-H		1053
X = S-Ph		972
X ₁ , X ₄ = S-H X ₂ , X ₃ = S-Ph		1004
X ₁ , X ₄ = H X ₂ , X ₃ = S-Ph		1038
X ₁ , X ₄ = H X ₂ , X ₃ = S-H		1055

2. Modeling of Chirality and HTP

In an effort to gain a better understanding of the relationship between absolute molecular configuration and optical rotation direction, there has been increasing interest in representing chirality in a more quantitative, mathematical manner. It is somewhat surprising that the computational prediction strategy so successfully exploited by the pharmaceutical industry has only been applied very recently to the prediction of “chiroptical” properties of LC systems for advanced optical and photonics applications. The earliest reported activity in this area was by Lisetski *et al.*,^{33–35} who used atomic coordinates determined either experimentally by x-ray diffraction or computationally from molecular models to calculate the HTP for a series of cholesteryl esters.

More recently, chirality has been determined computationally using two different approaches that are innately different in their level of development, ease of use, and efficiency. The first of these methods, explored in 1995 by Zabrodsky *et al.*,^{32,36} attempts to find the absolute distance between the corresponding atoms of the two configurations of a chiral molecule if they were to be superimposed over one another. One disadvantage

of this method is that it is extremely computationally intensive because of the large number of iterations required to arrive at solutions that are meaningful.

In 1995 Osipov *et al.*,³⁷ building on the work of Listeski *et al.*,^{33–35} proposed a second, simpler method based on the calculation of a “figure of merit” for chirality that they termed the chirality index (G_0). Recently, Solymosi *et al.*³⁸ improved upon the chirality index by introducing a scaling factor that allows comparison between molecules with different numbers of atoms. This scaled chirality index (G_{0S}) is used to find the contributions of individual atoms and atom groups to the overall (global) chirality of the molecule. This scaled chirality index is useful even in its abstract form; any asymmetry, if it exists, will be revealed by the nonzero value of G_{0S} . A symmetrical molecule returns a chirality index value of zero in nearly every case. Promising correlations between G_{0S} and important applications properties such as circular dichroism (CD) and the HTP of a chiral dopant in a liquid crystal host also have been shown by Neal *et al.*,³⁹ and Osipov and Kuball.⁴⁰

The scaled chirality index can be used to compare molecules of different sizes and is constructed to be maximized for a molecule with a strong steric stress and to vanish for any molecule that contains the point symmetry element S_n (a rotation-reflection axis), which would preclude chiral behavior. The chirality index is also capable of predicting the sign of the optical activity.

The numerical expression for the scaled chirality index is

$$G_{0S} = \frac{4!}{N^4} \frac{1}{3} \left\{ \sum_{\substack{\text{all permutations of} \\ i,j,k,l=1}}^N w_i w_j w_k w_l \times \frac{[(\mathbf{r}_{ij} \times \mathbf{r}_{kl}) \times \mathbf{r}_{il}](\mathbf{r}_{ij} \times \mathbf{r}_{jk})(\mathbf{r}_{jk} \times \mathbf{r}_{kl})}{(r_{ij} r_{jk} r_{kl})^n r_{il}^m} \right\}, \quad (5)$$

where \mathbf{r}_{ij} values are the atomic radii of the atoms contained in the chiral group upon which the chirality calculations are conducted and w_i , w_j , w_k , and w_l are values that represent the weighting factors of the individual atoms i thru l . We used this numerical expression to develop a multiplatform, multithreaded computational program to efficiently compute the chirality index for molecules of up to 250 atoms within minutes on most high-performance computer systems. Initial computations were performed on a SGI Origin 2000 server (sixteen 400-MHz

processors) running SGI IRIX 6.5, which would typically complete a chirality index calculation for a molecule with 200 atoms in approximately 4 h. The same code recompiled to run on a SGI Altix server (sixteen 2.5-GHz Itanium 2 processors) running Red Hat Enterprise Linux Release 3 computed the chirality index for the same compound with 200 atoms in approximately 5 min.

Finally, using the scaled chirality index, it is possible to determine the contributions of each atom to G_{0S} using

$$G_{0SA} = G_{0S} - \frac{4!}{N^4} \frac{1}{3} \times \left\{ \sum_{\substack{\text{all permutations of} \\ i,j,k,l=1 \cdots \hat{A} \cdots N}} w_i w_j w_k w_l \times \frac{[(\mathbf{r}_{ij} \times \mathbf{r}_{kl}) \times \mathbf{r}_{il}](\mathbf{r}_{ij} \times \mathbf{r}_{jk})(\mathbf{r}_{jk} \times \mathbf{r}_{kl})}{(r_{ij} r_{jk} r_{kl})^n r_{il}^m} \right\}, \quad (6)$$

where A is a specific atom in a molecule. Knowledge of the individual atom contributions can help to identify which molecular substructures or terminal groups have the greatest influence on the overall chirality of the molecule.

The HTP of a chiral material is essentially a measure of its ability to rotate incident linearly polarized light as a function of its concentration (if it is dissolved in a LC host material) or as a function of path length (if it is pure LC material). The HTP (β_M) is defined mathematically as

$$\beta_M = (pc_W r)^{-1}, \quad (7)$$

where p is the pitch length of the chiral medium³⁹ (the distance needed for polarized light to rotate 360° through the medium), c_W is the weight concentration, and r is the enantiomeric purity of the chiral material. As Eq. (7) shows, a material with a large HTP will be more effective at rotating plane-polarized light at much lower concentrations (or shorter path lengths) than a material with a small HTP. Materials with a large HTP are also more desirable because they can be used in much lower concentrations to achieve an equivalent optical effect, which not only reduces materials and device costs (chiral materials are usually the most expensive component of an LC mixture), but also avoids potential solubility and miscibility problems that occur when higher concentrations of chiral dopants with a small HTP are used.

Recent work by Neal *et al.*³⁹ shows a good correlation between HTP and G_{0S} . The correlation between G_{0S} and HTP has also been validated by the research of Osipov and Kuball,⁴⁰ which lays the foundation for the relationship between CD and HTP. Circular dichroism is observed when an optically active material absorbs left- and right-hand circular polarized light differently as a function of wavelength. The correlation between G_{0S} and HTP was shown to be applicable only to rigid molecular systems.³⁹

For flexible molecules, the scaled chirality index only accounts for one of many possible conformational isomers (“conformer”) of a molecule. Thus, in molecules with a high degree of rotational freedom, a new method has been developed to account for a large number of conformers. This method defines a complex chirality parameter χ_0 based on the Connolly⁴¹ surface of a chiral molecule. This parameter, which can be computed very rapidly, has been used most effectively in conjunction with a Monte Carlo simulation.⁴² In the simulation, a molecule is moved stepwise into millions of different conformations and the parameter is calculated for each conformer. Through this computationally intensive method, the prediction of HTP has been extended to flexible molecules in a limited number of cases.⁴³

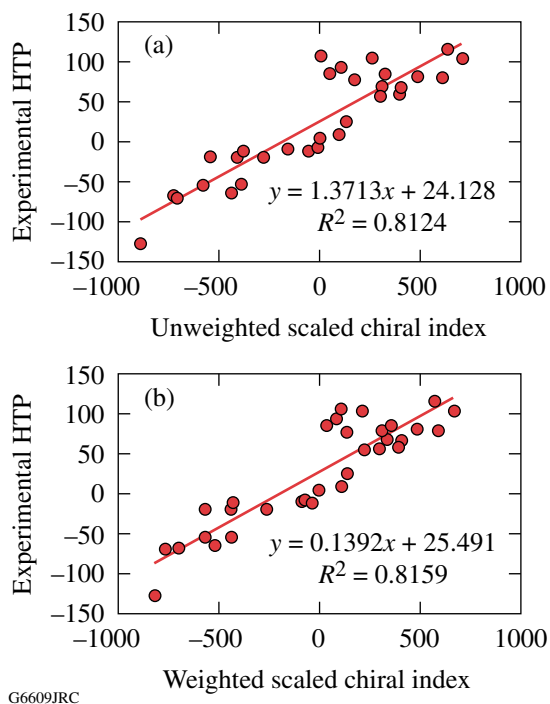
In the bulk of the previous literature on scaled chirality index calculations, the weight factor (w_i) is set to 1.0 to create a uniform density distribution. When using this method, it has been shown through the analysis of individual atom contributions that the main contributors to G_{0S} are (1) atoms located at points of steric stress and (2) atoms located a large distance from the molecular core (these are most frequently hydrogen atoms). Only one other weighting method has ever been applied. Solymosi *et al.*⁴⁴ set the weight of each atom equal to its van der Waals volume in their study of ferroelectric LC systems. This weighting method took into account the effect of excluded volume and was appropriate for use in the prediction of spontaneous polarization.

Our approach substituted the atomic mass into the calculation as the weight ($w_i = \text{atomic mass}$), as first suggested by Solymosi *et al.*³⁸ To our knowledge, we were the first to use atomic mass as the weighting factor for the chirality index.⁴¹ We hypothesized that the application of atomic mass would negate the effects of distance from the molecular core and enhance the effects of steric stress. Because the atoms at the greatest distance from the core are usually hydrogen and those at points of steric stress are carbon and/or other heavier elements, appropriate weighting was expected to enhance the

accuracy of the chirality index and lead to a greater predictive power for important properties like HTP.

Briefly stated, the calculation of the scaled chirality index involves a series of five steps: (1) The desired molecular structure is created and energy minimized using conventional molecular mechanics computational software. (2) All possible groups of four neighboring atoms within the molecule are selected and used to form the corners of a tetrahedral symmetry element. (3) The edge lengths of each tetrahedron are calculated and put into the chirality index equation to compute the chirality for a given tetrahedral element. (4) Summing all tetrahedral element contributions to the chirality gives the overall chirality index (no contributions from symmetric tetrahedra). (5) A scaling factor is applied to compensate for the variation in the number of tetrahedral symmetry elements as a function of molecular size. In our case, the *actual mass of each atom in every tetrahedral element* is taken into account, yielding the *weighted, scaled chiral index* G_{0SW} .

The effectiveness of the new weighted, scaled chirality index calculation was tested by calculating the HTP for six well-known rigid and flexible chiral molecular systems (binaphthol derivatives, helicenes, chiral steroid esters, phenylpropanoic acid derivatives, and mono- and bis-aminoanthraquinones with chiral substituents)⁴¹ and comparing the calculated data to experimental HTP data from the literature.^{45–52} A Pearson correlation of the calculated HTP data to the experimental HTP data was determined for each molecular system and as a global correlation for all systems. The Pearson correlation r is a measure of the fit of a least squares linear regression through the data set. Likewise, the correlation coefficient R^2 describes the proportion of the points that can be accounted for by the linear regression. For rigid molecular systems, the overall correlation was very strong for both the unweighted and weighted chirality indices, as shown by the linear regression fit for the plots of the chiral indices versus the experimental HTP data in Fig. 106.57.⁴¹ Although these molecules are all relatively rigid, the most flexible molecules within the systems appear to have the poorest correlation to experimental HTP data. A close examination of individual atom contributions reveals the benefits that the weighting system was expected to provide: the hydrogen atoms are not large contributors and the effects of steric stress are pronounced. The use of atomic mass predicts HTP more accurately when the experimental HTP is higher than $100 \mu\text{m}^{-1}$. In the case of the flexible systems, although the overall correlations were not as strong (as was expected to be the case from previous work by Neal *et al.*),³⁹ the use of atomic mass to weight the chirality index did enhance the



G6609JRC

Figure 106.57

The weighted (a) and unweighted (b) scaled chiral indices of all 32 rigid molecules plotted against the experimental helical twisting power data. A linear regression is used to determine the strength of the correlation. The R^2 value of the weighted index (0.82) is slightly stronger than that of the unweighted index (0.81).

quality of the correlation between calculated and experimental results significantly.⁴¹

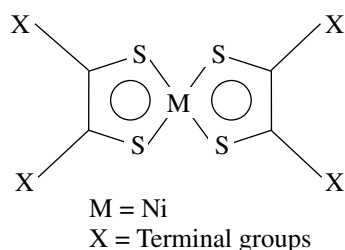
With the effectiveness of the new chirality index method now established, we applied it to the calculation of weighted and scaled chirality indices for the enantiomerically enriched

nickel dithiolenes described previously in **Enantiomerically Enriched Nickel Dithiolenes** (p. 117) and shown in Table 106.XIII. This chirality index data was then used to calculate the theoretical HTP for each chiral metal complex.⁴¹ The results of these calculations, along with available experimental HTP data, are shown in Table 106.XVI. Each X group can contain 1 to 3 chiral centers for a total of 4 to 12 chiral centers in each molecule. The rigid correlation was used both for the first two compounds where there was no spacer group ($n = 0$) and for all compounds with $n \leq 6$, while the flexible correlation was used for compounds with $n > 6$. For the materials with spacer groups, their low melting points made their purification very difficult and, as a result, sufficient quantities of high-purity materials were not available for experimental determination of the HTP.

Comparison of the calculated HTP values for the compounds in Table 106.XVI that contain a spacer group predicts that for materials with the same terminal X group, the HTP is expected to decrease with increasing spacer length. When the flexible spacer length is nine, the calculated HTP values are all generally the same. There is also good agreement between the calculated and experimental values for HTP in the two compounds with no spacer group, which, to a very limited extent, verifies the predictive capability of the approach. A full assessment of the predictive capabilities of the weighted, scaled chirality index requires isolation and purification, in sufficient quantities, of the remaining chiral nickel dithiolenes in Table 106.XVI for experimental HTP studies. This effort is currently in progress.

Because G_{05} can fluctuate dramatically on the basis of the lowest energy state of the energy-minimized conformer,

Table 106.XVI: The chiral X groups and helical twisting power data for a series of nickel dithiolenes IR dyes.



G6945JR

Terminal group	Experimental solvent	Experimental wavelength (nm)	Calculated wavelength (nm)
X = H	Hexane	720	720.91
X = CH ₃	CHCl ₃	774	843.08
X = CF ₃	Pentane	715	775.05
X = S-C ₄ H ₉	CHCl ₃	1104	1012.31
X = C ₆ H ₅	CHCl ₃	866	845.19
X = 2-naphthyl	CHCl ₃	905	993.08
X ₁ , X ₄ = H X ₂ , X ₃ = C ₆ , H ₅	CH ₂ Cl ₂	805	857.78

extreme care must be taken when attempting to use the chirality index as a global predictor for HTP. The high dependence of G_{05} on the minimum conformer energy state also accounts for the poor correlation of the scaled chirality index for flexible molecules. In this case, the computed energy-minimized conformer structure may not completely represent the actual conformer structure (or structures) that would be most likely to occur in nature. A better method for the prediction of HTP would take into account the many possible conformational geometries of a given molecule when computing the chirality through the use of Monte Carlo simulations.

Another limitation of the scaled chirality index method in its present form is that it is capable of accounting for factors such as temperature or dopant/host interactions only in nematic LC hosts. An improved chirality index that can incorporate both of these factors for other LC hosts would allow for a more accurate correlation, including global correlations between different molecular systems.⁵³ If the weighted, scaled chirality index method can be combined with a Monte Carlo simulation of geometric conformers (currently limited by processor speed), this enhanced chirality index could significantly increase the efficiency of chiral materials development. The latter point is the focus of our current and ongoing investigations.

Summary

Transition metal dithiolenes offer exciting new research opportunities in both materials chemistry and device applications. These new dyes are highly soluble in LC hosts, possess excellent thermal and photochemical stability, have structure-dependent dichroism, and can show LC mesomorphism on their own with the proper terminal functional groups. These properties, combined with their broad wavelength range, are all valuable attributes for near-IR LC device applications. The addition of enantiomerically enriched terminal groups to the dithiolene core results in a novel family of near-IR dyes that have low melting points (in many cases well below room temperature) and can induce both chirality and optical absorption when added to a nematic LC material. This new class of "liquid chiral dyes" is expected to give rise to a host of application possibilities in areas such as nonlinear optics and sensor protection.

The application of computational chemistry techniques to transition metal dithiolenes as described in this work represents a substantial technical achievement, given the lack of previous research activity in modeling transition metal organic complexes in general. The computational modeling methodology that we have developed was successfully applied to nickel

dithiolene systems in the prediction of both the near-IR electronic absorbance spectra and (for enantiomerically enriched materials) the helical twisting power in a host medium. These calculations represent what we believe to be the first of this type attempted for nickel dithiolene systems, or, for that matter, in any other transition metal organometallic complex. With these new computational techniques now in hand, the concept of designing and predicting, prior to synthesis, which structural elements will provide the most promising new transition metal dithiolene complexes for optical and photonics applications now becomes a very realistic objective.

ACKNOWLEDGMENT

This work is supported by the U.S. Department of Energy Office of Inertial Confinement Fusion under Cooperative Agreement No. DE-FC52-92SF19460 and the University of Rochester. The support of DOE does not constitute an endorsement by DOE of the views expressed in this article.

REFERENCES

1. H. Suzuki and G. Hayashi, U.S. Patent No. 4,763,966 (15 July 1985).
2. K. Drexhage and U. Mueller-Westerhoff, U.S. Patent No. 3,743,964 (3 July 1973).
3. J.-F. Bai *et al.*, *J. Mater. Chem.* **9**, 2419 (1999).
4. C. S. Winter *et al.*, *Mol. Cryst. Liq. Cryst.* **235**, 181 (1993).
5. H. Tanaka *et al.*, *Science* **291**, 285 (2001).
6. K. Wang and E. I. Stiefel, *Science* **291**, 106 (2001).
7. K. L. Marshall and S. D. Jacobs, *Mol. Cryst. Liq. Cryst.* **159**, 181 (1988).
8. K. L. Marshall, M. J. Guardalben, S. M. Corsello, M. S. Moore, I. A. Lippa, and R. P. Brecker, presented at the 16th Interdisciplinary Laser Science Conference (ILS-XVI), Providence, RI, 22–26 October 2000.
9. U. T. Mueller-Westerhoff *et al.*, *Mol. Cryst. Liq. Cryst. Lett.* **56**, 249 (1980).
10. K. Ohta *et al.*, *Mol. Cryst. Liq. Cryst.* **147**, 15 (1987).
11. U. T. Mueller-Westerhoff, B. Vance, and D. I. Yoon, *Tetrahedron* **47**, 909 (1991).
12. P. Espinet *et al.*, *Coord. Chem. Rev.* **117**, 215 (1992).
13. U. T. Mueller-Westerhoff and B. Vance, in *Comprehensive Coordination Chemistry: The Synthesis, Reactions, Properties, and Applications of Coordination Compounds*, 1st ed., edited by Sir G. Wilkinson, R. D. Gillard, and J. A. McCleverty (Pergamon Press, Oxford, England, 1987), Vol. 2, pp. 595–631.
14. K. L. Marshall, B. Schudel, and I. A. Lippa, in *Liquid Crystals VII*, edited by I.-C. Khoo (SPIE, Bellingham, WA, 2003), Vol. 5213, pp. 201–212.

15. M. Colvin, Lawrence Livermore National Laboratory, Continuum Models of Solvation, 2000, <http://gutenberg.llnl.gov/~colvin/solvation/solv.html> (10 January 2000).
16. C. E. A. Wainwright and A. E. Underhill, *Mol. Cryst. Liq. Cryst.* **234**, 193 (1993).
17. N. Svenstrup *et al.*, *Synthesis* **8**, 809 (1994).
18. A. Charlton *et al.*, *J. Mater. Chem.* **4**, 1861 (1994).
19. K. L. Marshall, B. Klehn, B. Watson, and D. W. Griffin, in *Advanced Characterization Techniques for Optics, Semiconductors, and Nanotechnologies*, edited by A. Duparré and B. Singh (SPIE, Bellingham, WA, 2003), Vol. 5188, pp. 48–60.
20. *LLE Review Quarterly Report* **81**, 37, Laboratory for Laser Energetics, University of Rochester, Rochester, NY, LLE Document No. DOE/SF/19460-335 (1999).
21. K. B. Wiberg, *Physical Organic Chemistry* (Wiley, New York, 1964).
22. W. J. Hehre, *A Guide to Molecular Mechanics and Quantum Chemical Calculations* (Wavefunction, Irvine, CA, 2003).
23. W. J. Hehre, *Ab Initio Molecular Orbital Theory* (Wiley, New York, 1986).
24. C. C. J. Roothaan, *Rev. Mod. Phys.* **23**, 69 (1951).
25. P. M. W. Gill, *Aust. J. Chem.* **54**, 661 (2001).
26. W. J. Hehre *et al.*, *J. Chem. Phys.* **52**, 2769 (1973).
27. M. S. Gordon *et al.*, *J. Am. Chem. Soc.* **100**, 2670 (1978).
28. M. M. Francl *et al.*, *J. Chem. Phys.* **77**, 3654 (1982).
29. M. Häser and R. Ahlrichs, *J. Comput. Chem.* **10**, 104 (2004).
30. R. M. Shroll and W. D. Edwards, *Int. J. Quantum Chem.* **63**, 1037 (1997).
31. E. R. Davidson, *J. Comput. Phys.* **17**, 87 (1975).
32. H. Zaborodsky and D. Avnir, *J. Am. Chem. Soc.* **117**, 462 (1995).
33. L. N. Lisetskii, *Ukr. Fiz. Zh.* **27**, 1321 (1982).
34. G. S. Chilaya and L. N. Lisetski, *Mol. Cryst. Liq. Cryst.* **140**, 243 (1986).
35. L. A. Batrachenko and L. N. Lisetskii, *Zh. Strukt. Khim.* **32**, 146 (1991).
36. H. Zaborodsky, S. Peleg, and D. Avnir, *J. Am. Chem. Soc.* **114**, 7843 (1992).
37. M. A. Osipov, B. T. Pickup, and D. A. Dunmur, *Mol. Phys.* **84**, 1193 (1995).
38. M. Solymosi *et al.*, *J. Chem. Phys.* **116**, 9875 (2002).
39. M. P. Neal *et al.*, *J. Chem. Phys.* **119**, 3567 (2003).
40. M. A. Osipov and H.-G. Kuball, *Eur. Phys. J. E* **5**, 589 (2001).
41. A. G. Noto and K. L. Marshall, in *Liquid Crystals IX*, edited by I.-C. Khoo (SPIE, Bellingham, WA, 2005), Vol. 5936, pp. 157–163.
42. D. J. Earl and M. R. Wilson, *J. Chem. Phys.* **120**, 9679 (2004).
43. D. J. Earl, *Phys. Rev. E* **71**, 021706 (2005).
44. M. Solymosi *et al.*, *Ferroelectrics* **227**, 169 (2002).
45. N. Ferrarini *et al.*, *Liq. Cryst.* **24**, 219 (1998).
46. D. J. Earl and M. R. Wilson, *J. Chem. Phys.* **119**, 10,280 (2003).
47. H.-G. Kuball *et al.*, *Mol. Cryst. Liq. Cryst.* **352**, 195 (2000).
48. M. J. Cook and M. R. Wilson, *J. Chem. Phys.* **112**, 1560 (2000).
49. F. Brandenburger *et al.*, *Liq. Cryst.* **28**, 1035 (2001).
50. Y. Aoki *et al.*, *Mol. Cryst. Liq. Cryst.* **346**, 35 (2000).
51. Y. Aoki *et al.*, *Bull. Chem. Soc. Jpn.* **71**, 2219 (2001).
52. H.-G. Kuball *et al.*, *J. Mater. Chem.* **5**, 2167 (1995).
53. H. Kamberaj *et al.*, *Mol. Phys.* **102**, 431 (2004).

Publications and Conference Presentations

Publications

- Y. V. Artemova, G. S. Bisnovaty-Kogan, I. V. Igumenshchev, and I. D. Novikov, "Black Hole Advective Accretion Disks with Optical Depth Transition," *Astrophys. J.* **637**, 968 (2006).
- M. Bobeica, D. R. Harding, and R. Q. Gram, "An Experimental Method for Measuring the Response of a Target to the Thermal Environment of the Fusion Reaction Chamber," in the *Twenty-First IEEE/NPSS Symposium on Fusion Engineering 2005* (IEEE, Piscataway, NJ, 2005).
- A. C.-A. Chen, J. U. Wallace, S. K.-H. Wei, L. Zeng, S. H. Chen, and T. N. Blanton, "Light-Emitting Organic Materials with Variable Charge Injection and Transport Properties," *Chem. Mater.* **18**, 204 (2006).
- D. Clay, D. Poslusny, M. Flinders, S. D. Jacobs, and R. A. Cutler, "Effect of LiAl_5O_8 Additions on the Sintering and Optical Transparency of LiAlON ," *J. Europ. Ceram. Soc.* **26**, 1351 (2006).
- V. N. Goncharov, O. V. Gotchev, E. Vianello, T. R. Boehly, J. P. Knauer, P. W. McKenty, P. B. Radha, S. P. Regan, T. C. Sangster, S. Skupsky, V. A. Smalyuk, R. Betti, R. L. McCrory, D. D. Meyerhofer, C. Cherfils-Cl  rouin, "Early Stage of Implosion in Inertial Confinement Fusion: Shock Timing and Perturbation Evolution," *Phys. Plasmas* **13**, 012702 (2006).
- O. V. Gotchev, V. N. Goncharov, J. P. Knauer, T. R. Boehly, T. J. B. Collins, R. Epstein, P. A. Jaanimagi, and D. D. Meyerhofer, "Test of Thermal Transport Models through Dynamic Overpressure Stabilization of Ablation-Front Perturbation Growth in Laser-Driven CH Foils," *Phys. Rev. Lett.* **96**, 115005 (2006).
- M. Haurylau, S. P. Anderson, K. L. Marshall, and P. M. Fauchet, "Electrical Modulation of Silicon-Based Two-Dimensional Photonic Bandgap Structures," *Appl. Phys. Lett.* **88**, 061103 (2006).
- S. I. Kudryashov, S. D. Allen, S. Papernov, and A. W. Schmid, "Nanoscale Laser-Induced Spallation in SiO_2 Films Containing Gold Nanoparticles," *Appl. Phys. B* **82**, 523 (2006).
- C. K. Li and R. D. Petrasso, "Stopping, Straggling, and Blooming of Directed Energetic Electrons in Hydrogenic and Arbitrary-Z Plasmas," *Phys. Rev. E* **73**, 016402 (2006).
- K. L. Marshall, A. Trajkovska-Petkoska, T. Z. Kosc, and S. D. Jacobs, "Polymer Cholesteric Liquid Crystal (PCLC) Flake/Fluid Host Suspensions: A Novel Electro-Optical Medium for Reflective Color Display Applications," in *EuroDisplay 2005* (Society for Information Display, San Jose, CA, 2005), pp. 552–554.
- M. Mikulics, S. Wu, M. Marso, R. Adam, A. F  rster, A. van der Hart, P. Kordo  , H. L  th, and R. Sobolewski, "Ultrafast and Highly Sensitive Photodetectors With Recessed Electrodes Fabricated on Low-Temperature-Grown GaAs," *IEEE Photonics Technol. Lett.* **18**, 820 (2006).
- A. V. Okishev, K. P. Dolgaleva, and J. D. Zuegel, "Experimental Optimization of Diode-Pumped Yb:GdCOB Laser Performance for Broadband Amplification at 1053 nm," in *International Conference on Lasers, Applications, and Technologies 2005: Advanced Lasers and Systems*, edited by G. Huber, V. Ya. Panchenko, and I. A. Scherbakov (SPIE, Bellingham, WA, 2006), Vol. 6054, pp. 124–127.
- A. V. Okishev, R. G. Roides, I. A. Begishev, and J. D. Zuegel, "All-Solid-State, Diode-Pumped, Multiharmonic Laser System for a Timing Fiducial," in *International Conference on Lasers, Applications, and Technologies 2005: High-Power Lasers and Applications*, edited by W. L. Bohn, V. S. Golubev, A. A. Ionin, and V. Ya. Panchenko (SPIE, Bellingham, WA, 2006), Vol. 6053, pp. 141–147.

L. A. Welsler, R. C. Mancini, J. A. Koch, N. Izumi, S. J. Louis, I. E. Golovkin, T. W. Barbee, Jr., S. W. Haan, J. A. Delettrez, F. J. Marshall, S. P. Regan, V. A. Smalyuk, D. A. Haynes, Jr., and R. W. Lee, "Multi-Objective Spectroscopic Analysis of Core Gradients: Extension from Two to Three Objectives," *J. Quant. Spectrosc. Radiat. Transf.* **99**, 649 (2006).

S. Wu, P. Geiser, J. Jun, J. Karpinski, J.-R. Park, and R. Sobolewski, "Long-Lived, Coherent Acoustic Phonon Oscillators in GaN Single Crystals," *Appl. Phys. Lett.* **88**, 041917 (2006).

Forthcoming Publications

R. Betti and C. Zhou, "Low-Adiabatic Implosions for Fast-Ignition Inertial Confinement Fusion," to be published in *Inertial Fusion Sciences and Applications 2005*.

T. R. Boehly, E. Vianello, J. E. Miller, R. S. Craxton, T. J. B. Collins, V. N. Goncharov, I. V. Igumenshchev, D. D. Meyerhofer, D. G. Hicks, P. M. Celliers, and G. W. Collins, "Shock-Timing Experiments Using Double-Pulse Laser Irradiation," to be published in *Physics of Plasmas* (invited).

J. Bromage, J. D. Zuegel, S.-W. Bahk, D. S. Vickery, L. J. Waxer, D. Irwin, V. Bagnoud, R. Boni, M. D. Moore, R. Jungquist, and C. Stoeckl, "High-Intensity Laser Diagnostics for OMEGA EP," to be published in *Inertial Fusion Sciences and Applications 2005*.

J. Bunkenburg, T. J. Kessler, W. Skulski, and H. Huang, "Phase-Locked Control of Tiled-Grating Assemblies for Chirped-Pulse-Amplified Lasers Using a Mach-Zehnder Interferometer," to be published in *Optics Letters*.

S. W. Culligan, A. C.-A. Chen, J. U. Wallace, K. P. Klubek, C. W. Tang, and S. H. Chen, "Effect of Hole Mobility Through Emissive Layer on Temporal Stability of Blue Organic Light-Emitting Diodes," to be published in *Advanced Functional Materials*.

J. L. DeCiantis, F. H. Séguin, J. A. Frenje, V. Berube, M. J. Canavan, C. D. Chen, S. Kurebayashi, C. K. Li, J. R. Rygg, B. E. Schwartz, R. D. Petrasso, J. A. Delettrez, S. P. Regan, V. A. Smalyuk, J. P. Knauer, F. J. Marshall, D. D. Meyerhofer, S. Roberts, T. C. Sangster, C. Stoeckl, K. Mikaelian, H. S. Park, and H. F. Robey, "Proton Core Imaging of the Nuclear Burn in Inertial Confinement Fusion Implosions," to be published in *Review of Scientific Instruments*.

D. H. Edgell, W. Seka, R. S. Craxton, L. M. Elasky, D. R. Harding, R. L. Keck, L. D. Lund, and M. D. Wittman, "Characterization of Cryogenic Direct-Drive ICF Targets During Layering Studies and Just Prior to Shot Time," to be published in *Inertial Fusion Sciences and Applications 2005*.

D. H. Edgell, W. Seka, R. S. Craxton, L. M. Elasky, D. R. Harding, R. L. Keck, and M. D. Wittman, "Analysis of Cryogenic Target Shadowgraphs at LLE," to be published in *Fusion Science and Technology*.

V. N. Goncharov, O. V. Gotchev, R. L. McCrory, P. W. McKenty, D. D. Meyerhofer, T. C. Sangster, S. Skupsky, and C. Cherfil-Cléroutin, "Ablative Richtmyer-Meshkov Instability: Theory and Experimental Results," to be published in *Inertial Fusion Science and Applications 2005*.

D. R. Harding, D. D. Meyerhofer, S. J. Loucks, L. D. Lund, R. Janezic, L. M. Elasky, T. H. Hinterman, D. H. Edgell, W. Seka, M. D. Wittman, R. Q. Gram, and M. J. Bonino, "Forming Smooth Cryogenic Target Layers for OMEGA Direct-Drive ICF Implosions and Prospects for Direct-Drive Targets for the NIF," to be published in *Physics of Plasmas* (invited).

M. Haurylau, S. P. Anderson, K. L. Marshall, and P. M. Fauchet, "Electrical Tuning of Photonic Bandgap Structures," to be published in *SPIE Newsroom*.

A. Jukna, I. Barboy, G. Jung, X. Li, D. Wang, R. Sobolewski, and A. Abrutis, "Electric Properties of $\text{YBa}_2\text{Cu}_3\text{O}_{7-\delta}$ Thin-Film Bridges with Laser-Written Channels of Easy Vortex Motion," to be published in the *Journal of Applied Physics*.

J. H. Kelly, L. J. Waxer, V. Bagnoud, I. A. Begishev, J. Bromage, B. E. Kruschwitz, T. J. Kessler, S. J. Loucks, D. N. Maywar, R. L. McCrory, D. D. Meyerhofer, S. F. B. Morse, J. B. Oliver, A. L. Rigatti, A. W. Schmid, C. Stoeckl, S. Dalton, L. Folsbee, M. J. Guardalben, R. Jungquist, J. Puth, M. J. Shoup III, D. Weiner, and J. D. Zuegel, "OMEGA EP: High-Energy Petawatt Capability for the OMEGA Laser Facility," to be published in *Inertial Fusion Sciences and Applications 2005*.

C. Kim, A. Trajkovska, J. U. Wallace, and S. H. Chen, "New Insight into Photoalignment of Liquid Crystals on Coumarin-Containing Polymer Films," to be published in *Macromolecules*.

- A. K. Knight and D. R. Harding, "Modeling the Sensitivity of a Polymer Vapor Deposition Process to Different Operating Conditions and Parameters," to be published in *Fusion Science and Technology*.
- B. E. Kruschwitz, R. Jungquist, J. Qiao, S. Abbey, S. E. Dean, D. N. Maywar, M. D. Moore, L. J. Waxer, and M. E. Wilson, "Large-Aperture Deformable Mirror Correction of Tiled-Grating Wavefront Error," to be published in *Inertial Fusion Sciences and Applications 2005*.
- C. K. Li and R. D. Petrasso, "Energy Deposition of MeV Electrons in Compressed Targets of Fast-Ignition Inertial Confinement Fusion," to be published in *Physics of Plasmas*.
- S. G. Lukishova, N. Lepeshkin, R. W. Boyd, and K. L. Marshall, "Far-Field Patterns from Dye-Doped Planar-Aligned Nematic Liquid Crystals Under High-Power, Nanosecond Laser Irradiation," to be published in *Molecular Crystals and Liquid Crystals*.
- S. G. Lukishova, N. Lepeshkin, R. W. Boyd, and K. L. Marshall, "Feedback-Free Hexagon Pattern Formation with Liquid Crystals and Isotropic Liquids," to be published in *Molecular Crystals and Liquid Crystals*.
- S. G. Lukishova and A. W. Schmid, "Near-Field Optical Microscopy of Cholesteric Oligomeric Liquid Crystal Layers," to be published in *Molecular Crystals and Liquid Crystals*.
- S. G. Lukishova, A. W. Schmid, R. Knox, P. Freivald, L. Bissell, R. W. Boyd, C. R. Stroud, Jr., and K. L. Marshall, "Deterministically Polarized, Room-Temperature Source of Single Photons," to be published in the *Journal of Modern Optics*.
- S. G. Lukishova, A. W. Schmid, R. P. Knox, P. Freivald, A. McNamara, R. W. Boyd, C. R. Stroud, Jr., and K. L. Marshall, "Single-Photon Source for Quantum Information Based on a Single Dye Molecule Fluorescence in Liquid Crystal Host," to be published in *Molecular Crystals and Liquid Crystals*.
- J. A. Marozas, F. J. Marshall, R. S. Craxton, I. V. Igumenshchev, S. Skupsky, P. B. Radha, T. J. B. Collins, R. Epstein, P. W. McKenty, M. J. Bonino, D. Jacobs-Perkins, D. D. Meyerhofer, T. C. Sangster, J. P. Knauer, V. A. Smalyuk, V. Yu. Glebov, S. G. Noyes, W. Seka, and R. L. McCrory, "Progress in Polar-Direct-Drive Simulations and Experiments," to be published in *Physics of Plasmas* (invited).
- F. J. Marshall, R. S. Craxton, M. J. Bonino, R. Epstein, V. Yu. Glebov, D. Jacobs-Perkins, J. P. Knauer, J. A. Marozas, P. W. McKenty, S. G. Noyes, P. B. Radha, W. Seka, S. Skupsky, V. A. Smalyuk, J. A. Frenje, C. K. Li, R. D. Petrasso, and F. H. Séguin, "Polar-Direct-Drive Experiments on OMEGA," to be published in *Inertial Fusion Science and Applications 2005*.
- R. L. McCrory, D. D. Meyerhofer, S. J. Loucks, S. Skupsky, R. Betti, T. R. Boehly, T. J. B. Collins, R. S. Craxton, J. A. Delettrez, D. H. Edgell, R. Epstein, K. A. Fletcher, C. Freeman, J. A. Frenje, V. Yu. Glebov, V. N. Goncharov, D. R. Harding, I. V. Igumenshchev, R. L. Keck, J. D. Kilkenny, J. P. Knauer, C. K. Li, J. R. Marciante, J. A. Marozas, F. J. Marshall, A. V. Maximov, P. W. McKenty, S. F. B. Morse, J. Myatt, S. Padalino, R. D. Petrasso, P. B. Radha, S. P. Regan, T. C. Sangster, F. H. Séguin, W. Seka, V. A. Smalyuk, J. M. Soures, C. Stoeckl, B. Yaakobi, and J. D. Zuegel, "Progress in Direct-Drive Inertial Confinement Fusion Research at the Laboratory for Laser Energetics," to be published in *Inertial Fusion Sciences and Applications 2005*.
- J. B. Oliver and D. Talbot, "Optimization of Deposition Uniformity for Large-Aperture Substrates in a Planetary Rotation System," to be published in *Applied Optics*.
- S. N. Shafrir, J. C. Lambropoulos, and S. D. Jacobs, "A Magnetorheological Polishing-Based Approach for Studying Precision Microground Surfaces of Tungsten Carbides," to be published in *Precision Engineering*.
- W. T. Shmayda, R. Janezic, T. W. Duffy, D. R. Harding, and L. D. Lund, "Tritium Operations at the Laboratory for Laser Energetics," to be published in *Fusion Science and Technology*.
- S. Skupsky, R. S. Craxton, F. J. Marshall, R. Betti, T. J. B. Collins, R. Epstein, V. N. Goncharov, I. V. Igumenshchev, J. A. Marozas, P. W. McKenty, P. B. Radha, J. D. Kilkenny, D. D. Meyerhofer, T. C. Sangster, and R. L. McCrory, "Polar Direct Drive—Ignition at 1-MJ," to be published in *Inertial Fusion Sciences and Applications 2005*.
- V. A. Smalyuk, O. Sadot, R. Betti, V. N. Goncharov, J. A. Delettrez, D. D. Meyerhofer, S. P. Regan, T. C. Sangster, and D. Shvarts, "Rayleigh–Taylor Growth Measurements of 3-D Modulations in Nonlinear Regime," to be published in *Physics of Plasmas* (invited).

C. Stoeckl, J. A. Delettrez, J. H. Kelly, T. J. Kessler, B. E. Kruschwitz, S. J. Loucks, R. L. McCrory, D. D. Meyerhofer, D. N. Maywar, S. F. B. Morse, J. Myatt, A. L. Rigatti, L. J. Waxer, J. D. Zuegel, and R. B. Stephens, "High-Energy Petawatt Project at the University of Rochester's Laboratory for Laser Energetics," to be published in *Fusion Science and Technology*.

W. Theobald, K. Akli, R. Clarke, J. A. Delettrez, R. R. Freeman, S. H. Glenzer, J. Green, G. Gregori, R. Heathcote, N. Izumi, J. A. King, J. A. Koch, K. Lancaster, A. J. MacKinnon, M. H. Key, C. Mileham, J. Myatt, D. Neely, P. A. Norreys, H.-S. Park, J. Pasley, P. Patel, S. P. Regan, H. Sawada, R. Shepherd, R. Snavely, R. B. Stephens, C. Stoeckl, M. Storm, B. Zhang, and T. C. Sangster, "Hot-Surface, Ionic-Line Emission and Cold

K-Inner-Shell Emission from Petawatt Laser Irradiated Cu Foil Targets," to be published in *Physics of Plasmas*.

J. D. Zuegel, V. Bagnoud, J. Bromage, I. A. Begishev, J. Puth, "High-Performance OPCPA Laser System," to be published in *Inertial Fusion Sciences and Applications 2005*.

J. D. Zuegel, S. Borneis, C. Barty, B. LeGarrec, C. Danson, N. Miyanaga, P. K. Rambo, T. J. Kessler, A. W. Schmid, L. J. Waxer, B. E. Kruschwitz, R. Jungquist, N. Blanchot, E. Moses, J. Britten, C. LeBlanc, F. Amiranoff, J. L. Porter, J. Schwarz, M. Geissel, I. C. Smith, I. Jovanovic, and J. Dawson, "Laser Challenges for Fast Ignition," to be published in *Fusion Science and Technology*.

Conference Presentations

The following presentations were made at Advanced Solid-State Photonics 2006, Incline Village, NV, 29 January–1 February 2006:

I. A. Begishev, V. Bagnoud, M. J. Guardalben, and J. D. Zuegel, "OPCPA Output Wavelength Tuning by Adjusting Time Delay Between Seed and Pump Pulses."

A. V. Okishev and J. D. Zuegel, "Athermal, Diode-Pumped Nd:YLF Regenerative Amplifier."

J. D. Zuegel, V. Bagoud, J. Bromage, and I. A. Begishev, "High-Performance OPCPA Laser System."

K. L. Marshall, A. Trajkovska-Petkoska, T. Z. Kosc, and S. D. Jacobs, "Polymer Cholesteric Liquid Crystal (PCLC) Flake/Fluid Host Electro-Optical Suspensions: Progress Toward Flexible Reflective Displays," USDC Fifth Annual Flexible Microelectronics and Displays Conference, Phoenix, AZ, 6–9 February 2006.

The following presentations were made at the 6th International Conference on High Energy Density Laboratory Astrophysics, Houston, TX, 11–14 March 2006:

S. Sublett, J. P. Knauer, I. V. Igumenshchev, A. Frank, and D. D. Meyerhofer, "Double-Pulse Laser-Driven Jets on OMEGA."

B. Yaakobi, "EXAFS Study of Shock Compression, Isentropic Compression, and Phase Transformation in Metals."

W. Seka, P. Rechmann, J. D. B. Featherstone, and D. Fried, "Lasers in Hard Tissue Dentistry," Academy of Laser Dentistry Annual Conference, Tucson, AZ, 15–18 March 2006.

J. Zhang and T. Y. Hsiang, "Dispersion Characteristics of Coplanar Waveguides at Subterahertz Frequencies," Progress in Electromagnetics Research Symposium, Cambridge, MA, 26–29 March 2006.

UNIVERSITY OF
ROCHESTER